ISSN 1028-8546

Volume XVIII, Number 1
Section: En
March, 2012

Azerbaijan Journal of Physics

Fizika

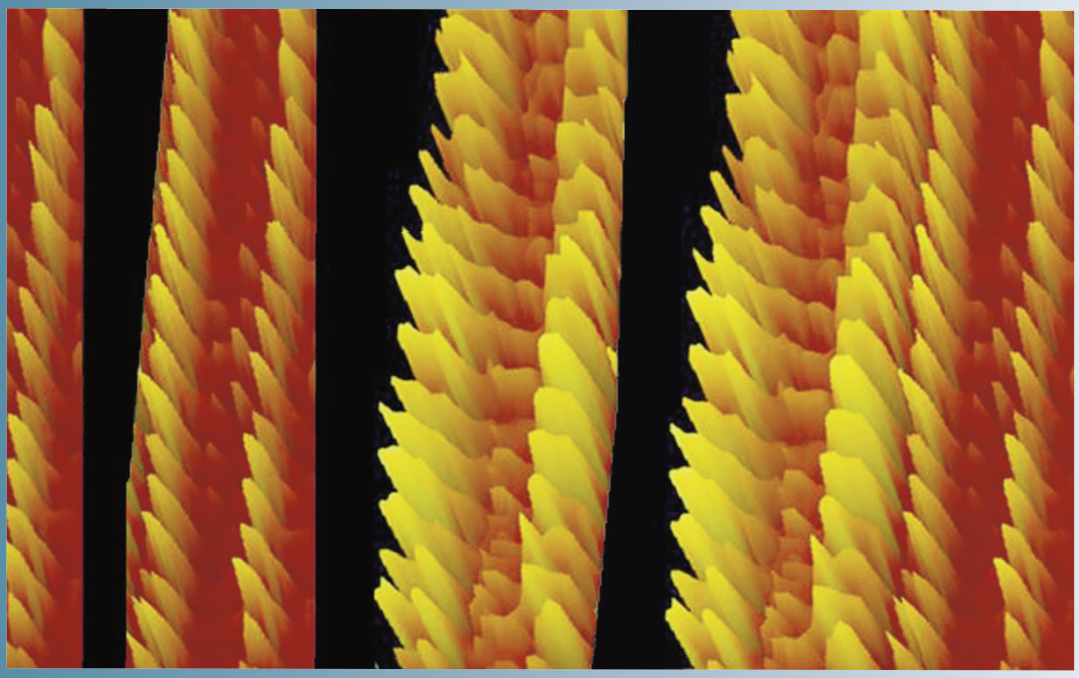

www.physics.gov.az

G.M. Abdullayev Institute of Physics
Azerbaijan National Academy of Sciences
Department of Physical, Mathematical and Technical Sciences

Published from 1995

ISSN 1028-8546
vol. XVIII, Number 1, 2012
Section: En

Azerbaijan Journal of Physics

Fizika

G.M.Abdullayev Institute of Physics
Azerbaijan National Academy of Sciences
Department of Physical, Mathematical and Technical Sciences

PUBLISHING OFFICE

33 H.Javid ave, AZ-1143, Baku
ANAS, G.M.Abdullayev Institute of Physics

Tel.: (99412) 439-51-63, 439-32-23
Fax: (99412) 447-04-56
E-mail: jophphysics@gmail.com
Internet: www.physics.gov.az/index1.html

It is authorized for printing: 30.03.2012

Published at: **"ŞƏRQ-QƏRB "**
17 Ashug Alesger str., Baku
Typographer :Aziz Gulaliyev

Sent for printing on: __ 04.2012
Printing approved on: __ 04.2012
Physical binding:_____
Number of copies:_____200
Order:_____

ANALYSIS OF MAIN ARTIFACTS IN SCANNING PROBE MICROSCOPY (I)

S.D. ALEKPEROV[1,2]
[1]*The branch of MSU named by M.V. Lomonosov in Baku,*
AZ-1141, F. Agayev str., 14, Baku
[2]*H.M. Abdullayev Institute of Physics of Azerbaijan National Academy of Sciences*
AZ-1143, G.Javid str., 33, Baku
e-mail: sdalekperov@mail.ru

The analysis of experiment carrying methodology in the scanning probe microscopy (SPM) region is carried out, the main parameters influencing on image quality are revealed. In order to reveal the artifact reason the main components of SPM signal which are divided on 5 groups: the useful signal; noises connected with external influences and temperature drift; distortions connected with piezoceramics and piezo-scanner non-ideality; probe geometry influence; apparatus noises are considered. The main methods of removal and minimization of the given artifacts are considered. The second and third groups of main components of SPM signal are considered in the article first part.

Keywords: scanning probe microscopy (SPM); scanning tunneling microscopy (STM); atomic force microscopy (AFM).
PACS :81.05.Je, 81.70.-q

INTRODUCTION

The advantages of probe microscopy methods [1,2] opposite to traditional investigation methods are difficultly overestimated. Let's enumerate the advantages of these methods: 1) high resolution up to atomic one ~0,1nm [3] in the combination with investigation locality allow us to compare SPM with transmission electron microscope; 2) the locality(the measurements are carried out directly in each surface point) gives to SPM the advantages in the comparison with investigation integral methods where the information is collected from any surface area or volume and further is averaged; 3) low interaction energies with the investigated object make the SPM methods indestructible ones, the average electron energy is milli-electron-volt order in scanning tunneling microscope STM, the interaction forces are usually nano-newton order in atomic force microscope AFM. This is very important at the investigation of "delicate" molecular objects, thin films, smooth polymer materials and bioobjects [5-7]; 4) the investigations by SPM methods can be carried out practically in any mediums *in situ* [8,9]: from super-high vacuum up to liquid solutions in the difference from all other surface investigation methods requiring the high vacuum. The limit condition is only one: the probe inertia to investigation medium; 5) the electroconductivity of investigated surface [10,11] isn't critic one for SPM methods. This fact allows us to investigate the objects of any conductance that also provides the advantage in the comparison with electron microscopy and other methods of surface electron analysis.

However, in spite of all these facts, the following and systematization of possible artifact appearance mechanisms are essentially important ones for adequate SPM application in wide-ranging scientific investigations. The last ones are the hardware effects leading to observation of false or distorted properties of investigated objects which can be caused by the influence of the research tool itself and etc. These artifacts as a rule, are easily taken into account on qualitative level at SPM result interpretation, however, the specifics of series of tasks can require the qualitative estimations and recombination of object real geometry methods. SPM images towards with useful information contain also much secondary information distorting the data about morphology and surface properties. In order to reveal the artifact reason, let's consider the main components of SPM signal. They can be divided on 5 groups: 1) the useful signal; 2) noises connected with external influences and temperature drift; 3) distortions connected with piezoceramics and piezo-scanner non-ideality; 4) the influence of the probe geometry; 5) hardware noises. The last 4 groups contribute the essential distortions into obtained surface relief. In first part of the article we will consider the second and third groups of main components of SPM signal.

1. THE NOISES CONNECTED WITH EXTERNAL INFLUENCES AND TEMPERATURE DRIFT

One should make compromise between value maximal sweep of scanning element and its resonance frequency [12] in the constructions of modern microscopes. The typical values of resonance frequencies for scanners are in the range 10-100 kHz. The different types of vibration isolation systems [13] are used for devise defense from external influences. The vibration isolation systems can be conditionally divided on active and passive ones. The main idea, consisting in passive vibration isolation systems, is the following one. The amplitude of forced oscillations of mechanical system strongly decreases at the difference increase between excitation force frequency and resonance eigenfrequency of system (the typical amplitude-frequency characteristics (AFC) of oscillation system is given on fig.1). That's why the external influences with $w_2 >> w_1$ frequencies don't practically essentially influence on oscillation system. As the proper frequencies of SPM heads are 10-100 kHz so choosing the resonance eigenfrequency of vibration isolation system enough low one (by 5-10 kHz order), one can effectively defense the device from external vibrations.

However, it is difficult to realize the low frequencies in practices. For spring platforms and elastic suspensions the frequency is equal to $\omega_0 = \sqrt{\frac{\kappa}{m}}$ where k is spring constant (or elastic suspension), m is mass of vibration isolation platform with SPM head. Let's estimate the vibration isolation system parameters providing the depression of high-frequency vibrations. From equilibrium condition it is followed that $mg = k\Delta l$, where Δl is elongation (or compression) of elastic element, g is free fall acceleration.

Then for the elongation value we obtain: $\Delta l = \frac{gm}{k} = \frac{g}{\omega_0^2} = \frac{g}{(2\pi\nu)^2} \cong 0{,}25 \times \frac{m(Hz)^2}{\nu^2}$. Thus, for obtaining of resonance frequency of vibration isolation system by 1 kHz order it is necessary that elongation (or compression) of elastic element is 25cm. One can easily realize such elongations with the help of spring or rubber suspensions. Taking into consideration that spring tension can achieve 100%, for realization of suspension resonance frequency in 1Hz the elastic element length should be 25cm and consequently, the out-to-out measure of vibration isolation system is 50 cm. If we decrease the requirements to resonance frequency, then we can achieve the essential decrease of vibration isolation system sizes. Thus, the elastic element compression should be 2,5mm for realization of frequency 10Hz. Such compression enough easily occurs in practices with help of stack of metallic plates with rubber layers that significantly decreases the vibration isolation system sizes. The active systems of external vibration depression are also successfully used for defense of SPM heads. Such devices present themselves the negative feedback electro-mechanical systems which causes the stable position of vibration isolation platform in space. The principle of operation of active systems can be considered on the following simple example. The vibration gauge (accelerometer), which is the device reacting on acceleration endured by platform, is posited on platform. The signal from the gauge receives to feedback system (FS) where it increases and in antiphase is given to piezoelectric blocks which displaces to opposite side, damp the acceleration endured by platform. This is so-called proportional regulation. Indeed, let's under external force influence, the platform oscillates on *w* frequency so that its displacement is $u = u_0 \sin(wt)$.

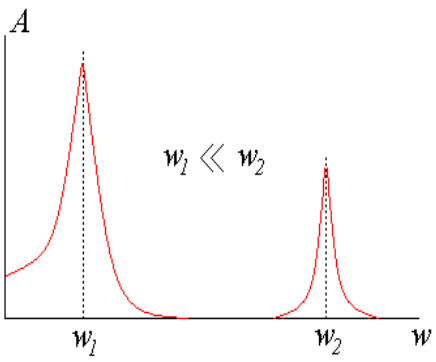

Fig.1. The schematic image of amplitude-frequency characteristics of oscillation system (w_1 is proper system resonance frequency; w_2 is external vibration frequency).

Then the acceleration of platform is equal to $\frac{d^2u}{dt^2} = -w^2 u_0 \sin(wt)$. The feedback system in this case gives the antiphase signal on blocks as a result of which the platform displacement will present itself the superposition of two displacements :

$$u = u_0 \sin(wt) - A\sin(wt) = (u_0 - A)\sin(wt).$$

Moreover, the feedback system will increase signal amplitude *A* till that platform acceleration will be equal to zero: $\frac{d^2u}{dt^2} = -w^2(u_0 - A)\sin(wt)$. The operation frequency band of active systems is defined by frequency band of stable work of feedback electromechanical system. In the case of nonharmonic vibrations *u=u(t)* signal from accelerometer is integrated two times by hardware and in antiphase is given on piezoelectric blocks so that platform oscillation amplitude tends to zero:

$$\frac{d^2u}{dt^2} = u(t) - A\iint \frac{d^2u}{dt^2}(t)dt \Rightarrow 0.$$

The one of SPM important problem is the task of probe stabilization position over investigated sample surface. The temperature change of environment or microscope construction element heat during the microscope work [14] is the main source of probe instability position. The solid body temperature change leads to appearance of thermoelastic deformations: $u_{ik} = \alpha_{ik}\Delta T$, where u_{ik} is deformation tensor, α_{ik} is tensor of material thermal expansion coefficients; ΔT is temperature increment.

For isotropic materials the thermal expansion coefficient is scalar value so $\alpha_{ik} = \alpha \cdot \delta_{ik}$, where δ_{ik} is Kronecker unit tensor, α is absolute value of thermal expansion coefficient. The absolute elongation of microscope construction elements can be estimated from the following relations:

$$u = \frac{\Delta l}{l_0} = \alpha \cdot \Delta T\ ;\ \Delta l = l_0 \alpha \cdot \Delta T\ .$$

The typical values of material thermal expansions are 10^{-5}-10^{-6} degree $^{-1}$. So at body heating by length 10 cm on $1°C$ its length increases on the value by 1μm order. Such deformations essentially influence on the work of probe microscopes. The thermostating of PSM measuring heads is applied for decrease of thermo-drift or thermo-compensating elements are introduced into head construction. Any SPM construction can be presented in the form of element series with different thermal expansion coefficients. The thermocompensating elements having the different expansion coefficients are introduced into construction of SPM measuring heads for thermo-drift compensation so that the following condition $\Delta L = \sum_i \Delta l_i = \Delta T \sum_i \alpha_i l_i \Rightarrow 0$ for temperature expansion sum in construction different arms is satisfied. The introduction of SPM compensating elements from the same material and with the same character sizes that the main elements have, is simplest method of thermo-drift decrease of probe position along Z axis. The probe displacement along Z direction will be minimal one at temperature change of such construction.

2. THE DISTORTIONS CONNECTED WITH PIEZOCERAMICS AND SCANNER NONIDEALITY

The piezoelectric engines [15] are used for controlled needle displacement on super-small distances in SPM. Their task is to provide the precision mechanical scanning by probe of the investigated sample by the way of probe displacement relatively immovable sample or sample displacement relatively immovable probe. The operation of many

piezoelectric engines applied in modern SPM is based on the use of reversal piezoeffect which is in change of piezomaterial sizes at electric field influence. The basis of many piezoceramics used in SPM is $PbZr_{1-x}Ti_xO_3$ composition (lead zirconate-titanate) with different additions [16]. The piezoplate elongation fixed from one edge is defined by the expression: $\Delta l = l\frac{U}{h}d_{31}$, where l is plate length, h is plate thickness, U is electric voltage applied to electrodes posited on piezoplate faces, d_{31} is material piezomodule. Piezomodule d_{31} defining the voltage transformation in displacement in longitudinal direction is usually equal to $(30\text{-}350)\cdot 10^{-12}$ m/V. The piezomodule big coefficients are important for less scanner sizes and less controlling voltages. The maximal value of piezomaterial deformation defining the maximal scanning field is limited by electric field strength value at which the material electrical breakdown appears. The minimal step or displacement delicacy are mainly defined by noises of controlling electric voltage, mechanical vibration level and thermo-drift value. One can select main piezoceramic characteristics applied in SPM: small requisite power and absence of heat generation; d_{31} piezomodule stability at low temperatures (up to helium ~4,2K) that is important for low-temperature SPM; Curie temperature 170÷350 °C; small sizes, high regidity and as a result, the high resonance frequencies (> 10 kHz) necessary for defense from vibrations. The high resonance frequency allows us also to increase the scanning velocity, i.e. to decrease of SPM data obtaining time; applicability in different mediums and super-high vacuum as they are chemically aren't active ones and don't form the electromagnetic fields.

In spite of mentioned advantages, the piezoceramics also have some disadvantages which can introduce the specified distortions in SPM images:

1) Non-linearity

The piezoceramic deformation is the complex function of external field: $\Delta l = f(U)$. The typical values of E^*fields at which the non-linear effects are seen, are 100 V/mm order. That's why for correct work of scanning elements the controlling fields in the ceramic linearity region ($E<E^*$) are usually used.

2) Hysteresis

SPM scanner hysteresis leads to displacement of scanning region (and correspondingly, SPM-images) obtained at direct and reversal displacements. That's why for exclusion of distortions of sample surface SPM-images connected with hysteresis, it is necessary to carry out the measurements only at direct or only reversal scanner motion.

3) Creep

If the applied voltage is in the form of step then the displacement continuance in the form of the given on the fig.2 (piezoceramic bounce) is observed. The creep is revealed in the distortion of scan initial region at big squares and scanning velocities, i.e. when the voltage applied to piezomaterial, changes enough rapidly. The creep influence decreases at scanning velocity decrease and also after scanner "training". It is clear that creep reveals at strongly scanner displacement into required initial scanning point, that's why the strong jumps of controlling voltage are excluded in algorithms of scanner control and time delays taking into consideration the creep are introduced.

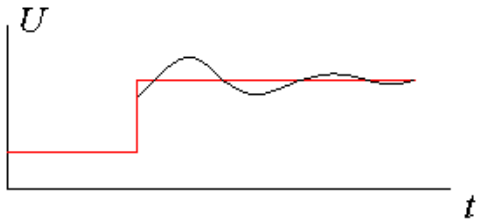

Fig. 2. The piezoceramic creep and bounce.

4) Temperature drift

The occasional temperature changes always existing in the laboratory lead to change of construction element length and relative displacement of probe and sample. For example, at temperature change on ΔT=1°C, the piezotube by l=20 mm length with thermal linear expansion coefficient $\beta=2\cdot 10^{-6}\ K^{-1}$ changes its length on $\Delta l=\beta\cdot l\cdot\Delta T$=40 Å. The slow temperature drift along Z coordinate in scanning process leads to inclination of sample plane on SPM-image. The change of linear sizes along X and Y coordinates leading to mutual displacement of probe and sample in sample plane leads to the image scale change. As a whole, these distortions of piezoceramic properties are similar to ones caused by ceramic creep.

The nonideality of piezoceramic properties leads to the fact that SPM image obtained with the help of piezoceramic scanner contains the series of specific distortions. For tripod scanner the probe at scanning will move in Z-direction on arc of a circle and for tube scanner the probe trajectory at scanning will be describe the complex hyperbolic function. In both cases the image which is seen curved even when real sample surface is totally plane, is obtained. Partially these images can be excluded on hardwire level using the linearization methods of scanner characteristics. There are the several methods of scanner nonlinearity corrections in scanning probe microscopes. The most reliable and the most expensive method to solve of this problem is in the direct measurement of scanner momentary position and nonlinearity correction in real time by means of the feedback circuit. The capacity gauges [17] and tensogauges [18], photodetectors [19] or optical interferometers can be used in the capacity of displacement gauges.

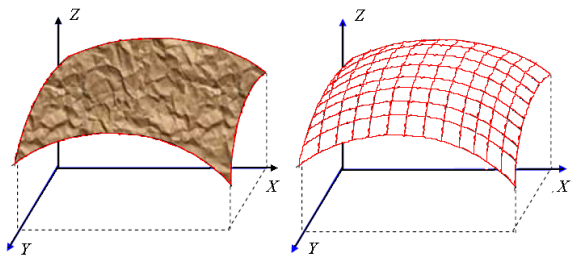

Fig. 3. The surface deduction of 2-d order from SPM surface image.

The second more simple method is in the use of such nonlinear voltages for piezoceramics that scanner resultant displacement should be approximately linear one. For this the scanner should be previously standardized, i.e. the function of displacement dependence on applied voltage is found. The

scanner calibration is usually carried out with use of samples with periodic structures of before known sizes (so-called test-objects). However, in spite of this, not all distortions can be excluded on hardwire level. In particular, as it is above mentioned, the scanner movement in sample plane influences on probe position over surface (on Z axis), SPM images present themselves the superposition of real relief and some surface of *2d* (and higher) order.

For exclusion of such type distortions by the lest square method the approximating surface of *2d* order $P^{(2)}(x,y)$ having the minimal inclinations from inital functions $Z=f(x,y)$ is found and further, the given surface is deducted from initial SPM-image: $Z'_{ij}=Z_{ij} - P_{ij}^{(2)}$. The deduction result of surface of *2d* order from real surface AFM-image [20] is presented on fig.3. The one more type of distortions is connected with nonlinearity and nonorthogonality of scanner displacement in X,Y plane. This leads to distortion of geometric proportions in different parts of SPM surface image. For exclusion of such distortions the correction procedure of SPM images with the help of correction factor fail which is formed at scanning by concrete scanner of test structures with well known relief is carried out. Concerning scanner resonance frequency then it is necessary to increase it as possible. For example, the resonance eigenfrequency ω of tube piezoscanner is defined as follows: $\omega = \frac{1}{2\pi}\frac{(1{,}875)^2}{l^2}\sqrt{\frac{EI_z}{m}}$,

where I_z is inertia moment relative to Z axis, l is length, m is mass, $E=c^2\rho$ is Young's modulus, c is sound velocity in piezoceramics, ρ is piezoceramic density. As it is seen from the formula, the increase of scanner displacement range because of the increase of its length leads to quadratic decrease of its resonance frequency. The scanners with high value of resonance frequency, firstly, are better defended from external vibration influence and secondary, allows us to follow signals in enough wide frequency band with delicacy. This gives the possibility to establish the scanning high velocity decreasing the time necessary for obtaining of information. The scanning time decrease of the given region is comfortable for one side, and is of the fundamental importance as at the harmful influence of temperature drift decreases from another one.

[1] *G. Binnig and H. Rohrer*. Scanning tunneling microscopy // *Helv. Phys. Acta.*, -1982, - v. 55, - pp. 726-735.

[2] *G. Binnig, H. Rohrer, C. Gerber, and E. Weibel.* Tunneling through a controllable vacuum gap // *Appl. Phys. Lett.*, 1982, v. 40, pp. 178-180.

[3] *Q. Binniq, Q. Porer*. Skaniruyushaya tunnelnaya mikroskopiya – ot rojdeniya k yunosti // UFN, -1988, t. 154, No 2, ss. 261-277. (in Russian).

[4] *N. S. Maslova, A. I. Oreshkin, V. I. Panov, S. V. Savinov, A. A. Kalachev, and J. P. Rabe.* STM evidence of dimensional quantization on the nanometer size surface defects // *Solid State Communications*, 1995, v. 95, No 8, pp. 507-510.

[5] *C. Bustamante, J. Vesenka, C. L. Tang, W. Rees, M. Guthod, and R. Keller.* Circular DNA molecules imaged in air by scanning force microscopy //*Biochemistry*, 1992, v. 31, pp. 22-26.

[6] *G. U. Lee, L. A. Chrisey, and R. J. Colton.* Direct measurements of the forces between complementary strands of DNA // *Science*, 1994, v. 266, pp. 771–773.

[7] *M. Guthold, M. Bezanilla, D. A. Erie, B. Jenkins, H. G. Hansma, and C. Bustamante.* Following the assembly of RNA polymerase-DNA complexes in aqueous solutions with the scanning force microscope // *Proc. Natl. Acad. Sci. USA*, 1994, - v. 91, No 26, pp. 12927-12931.

[8] *V.I. Panov.* Skaniruyushaya tunnelnaya mikroskopiya I spektroskopiya povernosti, UFN, t. 155, №1, s. 155-158, 1988. (in Russian).

[9] *V.S. Edelman.* Razvitie skaniruyushey tunnelnoy I silovoy mikroskopii, Pribori I texnika eksperimenta, №1, s. 24-42, 1991. (in Russian).

[10] *G. Binning, C. F. Quate, and C. Gerber.* Atomic force microscopy // *Phys. Rev. Lett.*, 1986, v. 56, No 9, pp. 930-933.

[11] *H.K. Wickramasinghe.* Progress in scanning probe microscopy, Acta materialia, v.48, p.347, 2000.

[12] *A.A. Buxarev, N.B. Berdunov, D.V. Ovchinnikov, K.M. Salixov.* SSM metroloqiya mikro – i nanostruktur, Mikroelektronika, t. 26, №3, s. 163-175, 1997. (in Russian).

[13] *V. Y. Yurov, A. N. Klimov*. (1994). Scanning tunneling microscope calibration and reconstruction of real image: Drift and slope elimination, *Review of Scientific Instruments* **65** (5): 1551-1557.

[14] *Meyer E. et al.* Scanning Probe Microscopy: The Lab on a Tip. — Berlin–Heidelberg: Springer-Verlag, 2003. — 210 p.

[15] *A.A. Erofeev, S.B Boychov, T.A. Poplevkin*. Pezokeramicheskie mikromanipulyatori dlya skaniruyusheqo tunnelnoqo mikroskopa. Elektronnaya promishlennost, 1991, №3, s. 54.(in Russian).

[16] *A.P. Volodin, A.E. Panich.* Primenenie pezokeramicheskix pezokeramicheskix materialov PKP v nizkotemperaturnix skaniruyushix tunnelnix mikroskopax. Pribori I texnika eksperimenta, 1989, №5, s. 188. (in Russian).

[17] *J.E. Griffith, G.L. Miller, C.A. Green.* A Scanning Tunneling Microscope with a Capacitance- Based Position Monitor. J. Vac. Sci. Technot. B 8(6), 2023 (1990).

[18] *Mizutani et.* al. A Piezoelectric-Drive Table and its Applications to Microgrinding of Ceramic Materials. Precision Engineering. 12(4), 219 (1990).

[19] *R.C. Barrett, C.F. Quate.* Optical Scan-Correction System Applied to Atomic Force Microscopy. Rev. Sci. Instrum. 62(6), 1393 (1991).

[20] *V.L. Mironov.* Osnovi skaniruyushiy zondovoy mikoskopii. Rossiyskaya akademiya nauk, Institut fiziki mikrostruktur q. Nijniy Novqorod, 2004 q.110 s. (in Russian).

Receved:14.02.2012

THE STRUCTURE FUNCTIONS FOR LARGE-P_T HADRON PRODUCTION IN SEMI-INCLUSIVE DIS

S.K. ABDULLAYEV, A.I. MUKHTAROV, M.Sh. GOJAYEV
Baku State University,
AZ-1148, Z.Halilov str., 23, m_qocayev@mail.ru

We calculate, within perturbative QCD the expressions for unpolarized and polarized structure functions for large- p_T baryon production in semi-inclusive DIS. After deriving the complete set of the polarized cross-section which is differential with respect to the transverse momentum, we discuss characteristic features of the azimuthal spin asymmetries, using existing parton densities and fragmentation functions at COMPASS and EIC energies.

Keywords: semi-inclusive deep inelastic scattering, double spin asymmetry, distribution and fragmentation functions
PACS:10-29

1. INTRODUCTION

The standard model of the electroweak interactions of the elementary particles has achieved a great success in the description of series of the experiments, which have been carried out in the various laboratories of the world. In particular, one of its exact checking has been alone on the e^-e^+-colliders LEP and SLC, as the result of which the agreement with the experimental data has been obtained. Alongside with e^-e^+-annihilation the deep-inelastic scattering (DIS) processes of the polarized leptons on the polarized nucleons play the important role in the check of standard theory and they are intensive investigated at the present time [1-15].

In this paper we study the structure functions for the polarized baryon production in polarized semi-inclusive DIS off nucleon

$$e^-(\lambda_e)+N(\lambda_N)\Rightarrow e^-+B(\lambda_B)+X, \quad (B=\Lambda,\Sigma^{\pm}) \tag{1}$$

where λ_e is the electron spirality, λ_N and λ_B are the longitudinal polarizations of nucleon-target and baryon B. In order that a final hadron carries large transverse momentum, another parton has to be emitted in the opposite directions. This is on $O(\alpha_s)$ effect in perturbative QCD and was investigated in [15] for the unpolarized semi-inclusive DIS with electron and neutrino beams. Here we extend the analysis to the polarized cases and study the polarization of baryons in semi-inclusive DIS processes. We stress that the polarization of baryons is an important source of new information.

2. THE HADRON FRAME

The momenta of particles are defined in Fig. 1. We define five Lorentz invariants for specifying the kinematics. The center of mass energy s for the initial lepton and the nucleon is

$$s=(k+P)^2\approx 2(kP), \tag{2}$$

where we ignored masses. Conventional DIS variables

$$x_B=\frac{Q^2}{2(qP)}, \tag{3}$$

$$Q^2=-q^2=-(k-k')^2. \tag{4}$$

are determined by observing the final lepton. For the description of kinematics of the final hadron B, we introduce

$$z_B=\frac{(PP_B)}{(qP)} \tag{5}$$

and the transverse component of q which is orthogonal to P и P_B:

$$q_t^{\mu}=q^{\mu}-\frac{(qP_B)}{(PP_B)}P^{\mu}-\frac{(qP)}{(PP_B)}P_B^{\mu}. \tag{6}$$

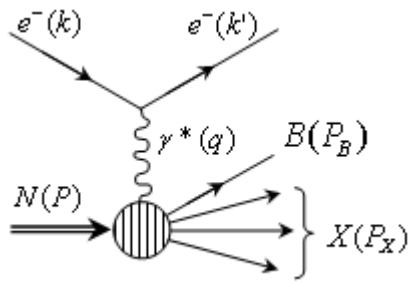

Fig. 1. Feynman diagram for $e^-N\Rightarrow e^-BX$

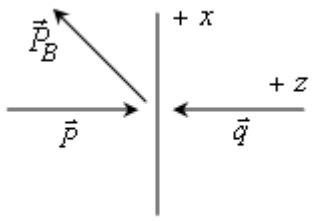

Fig. 2. The hadron frame

q_t^μ is a space-like vector and we define its magnitude as

$$q_T = \sqrt{-q_t^2}\ . \tag{7}$$

In the parton model, there are no bremsstrahlung partons and all parton momenta are exactly collinear with the corresponding hadron momenta, so one has $q_t^\mu = 0.$ At the order α_S, parton emission makes q_t^μ nonzero, in general. We will give formulas for the distribution of events as a function of q_T^2.

Define the hadron frame as follows, as pictured in Fig. 2. In the hadron frame, the time-component of the virtual photon momentum is zero and its space-components lie along the negative z-axis:

$$q^\mu = (0,0,0,-Q), \tag{8}$$

where

$$Q = \sqrt{-q^2}\ . \tag{9}$$

The space-components of momenta of the incoming nucleon are exactly along the positive z-axis in the hadron frame. Then the components of P in the hadron frame are:

$$P^\mu = \frac{Q}{2x_B}(1,0,0,1). \tag{10}$$

We align the x-axis of the hadron frame so that the space-components of P_B^μ lie in the $x-z$ plane, with $P_B^x > 0$. The direction of P_B^μ as seen from the hadron frame is fixed once q_T/Q is given. One finds easily that P_B^μ can be written as

$$P_B^\mu = \frac{1}{2} z_B Q\left(1+\frac{q_T^2}{Q^2}, 2\frac{q_T}{Q}, 0, \frac{q_T^2}{Q^2}-1\right). \tag{11}$$

In order to write the lepton momentum in the hadron frame, we need to in introduce the azimuthal angle Φ between the hadron plane and the lepton plane. Then the lepton momentum can be parameterized as

$$k^\mu = \frac{1}{2}Q(\cosh\psi, \sinh\psi\cos\Phi, \sinh\psi\sin\Phi, -1) \tag{12}$$

and

$$k'^\mu = k^\mu - q^\mu = \frac{1}{2}Q(\cosh\psi, \sinh\psi\cos\Phi, \sinh\psi\sin\Phi, +1), \tag{13}$$

with

$$\cosh\psi = \frac{2x_B s}{Q^2} - 1. \tag{14}$$

With this definitions, the cross section for (1) can be expressed in terms of s, x_B, Q^2, z_h, q_T^2 and Φ in the hadron frame.

3. THE DIFFERENTIAL CROSS SECTION

The differential cross section for the semi-inclusive hadron production (1) can be written as

$$d\sigma = \frac{1}{2s}\cdot\frac{d^3P_B}{(2\pi)^3 2E_B}\cdot\frac{d^3k'}{(2\pi)^3 2E'}\cdot\frac{e^4}{q^4}L_{\mu\nu}(k,k')W^{\mu\nu}(P,P_B,q), \tag{15}$$

where $L_{\mu\nu}$ is the lepton tensor defined as

$$L_{\mu\nu}(k,k') = 2[k_\mu k'_\nu + k'_\mu k_\nu - g_{\mu\nu}(kk') - i\lambda_e\varepsilon_{\mu\nu\rho\sigma}k^\rho k'^\sigma], \tag{16}$$

$W^{\mu\nu}(P,P_B,q)$ is the hadronic tensor.

Using Lorentz invariance, current conservation and the hermiticity of the current operator, we express hadronic tensor $W^{\mu\nu}$ in a basis of nine independent structure functions F_k, G_k, H_k, I_k:

$$W^{\mu\nu} = \sum_{k=1}^{9} W_k^{\mu\nu}[F_k + \lambda_N G_k + \lambda_B H_K + \lambda_N\lambda_B I_K], \tag{17}$$

here $W_k^{\mu\nu}(k=1\div 9)$ are nine tensors constructed from P^μ, P_B^μ and q^μ. The structure functions F_k and G_k, H_k and I_k contain the information about hadrons. They depend only on the invariants x_B, Q^2, z_B and q_T.

To construct the tensors $W_k^{\mu\nu}$, we make use of the vectors T^μ, X^μ, Y^μ and Z^μ, defined as:

$$T^\mu = \frac{1}{Q}(q^\mu + 2x_B P^\mu),$$

$$X^\mu = \frac{1}{q_T}\left[\frac{1}{z_B}P_B^\mu - q^\mu - \left(1+\frac{q_T^2}{Q^2}\right)x_B P^\mu\right], \quad (18)$$

$$Y^\mu = \varepsilon^{\mu\nu\rho\sigma} Z_\nu X_\rho T_\sigma, Z^\mu = -\frac{q^\mu}{Q}.$$

These vectors are orthogonal to one another and normalized to $T_\mu T^\mu = 1,\ \ X_\mu X^\mu = -1,\ \ Y_\mu Y^\mu = -1,$ $Z_\mu Z^\mu = -1$. Note that T^μ, X^μ and Z^μ are vectors, while Y^μ is an axial vector. Since $W_k^{\mu\nu}$ satisfies the current conservation, $q_\mu W^{\mu\nu} = \ = q_\nu W^{\mu\nu} = 0$, it is easy to see that $W^{\mu\nu}$ can be expanded in terms of nine independent tensors, for which we employ the following:

$$\begin{aligned}
W_1^{\mu\nu} &= X^\mu X^\nu + Y^\mu Y^\nu,\\
W_2^{\mu\nu} &= g^{\mu\nu} + Z^\mu Z^\nu,\\
W_3^{\mu\nu} &= T^\mu X^\nu + X^\mu T^\nu,\\
W_4^{\mu\nu} &= X^\mu X^\nu - Y^\mu Y^\nu,\\
W_5^{\mu\nu} &= i(T^\mu X^\nu - X^\mu T^\nu),\\
W_6^{\mu\nu} &= i(X^\mu Y^\nu - Y^\mu X^\nu),\\
W_7^{\mu\nu} &= i(T^\mu Y^\nu - Y^\mu T^\nu),\\
W_8^{\mu\nu} &= T^\mu Y^\nu + Y^\mu T^\nu,\\
W_9^{\mu\nu} &= X^\mu Y^\nu + Y^\mu X^\nu.
\end{aligned} \quad (19)$$

The first five of these tensors are even under a parity transformation while tensors 6 through 9 are odd under parity. Tensors $W_{1,2,3,4,8,9}^{\mu\nu}$ are symmetric under interchange of μ and ν while tensors $W_{5,6,7}^{\mu\nu}$ are antisymmetric.

One can sort the tensors according to their properties under rotations about the z-axis. The tensors $W_1^{\mu\nu}$, $W_2^{\mu\nu}$ and $W_6^{\mu\nu}$ are invariant under such rotations and this carry angular momentum zero. The tensors $W_3^{\mu\nu}$, $W_5^{\mu\nu}$, $W_7^{\mu\nu}$ and $W_8^{\mu\nu}$ carry angular momentum ± 1, while $W_4^{\mu\nu}$ and $W_9^{\mu\nu}$ carry angular momentum ± 2.

In order express $L_{\mu\nu}W^{\mu\nu}$ in term of the structure functions F_k, G_k, H_k and I_k, we write the products $L_{\mu\nu}W_k^{\mu\nu}$ in the form

$$A_k = \frac{1}{Q^2} L_{\mu\nu} W_k^{\mu\nu}. \quad (20)$$

The A_k are then functions of the angles Φ and ψ [14]:

$$\begin{aligned}
A_1 &= (+1)\cdot(1+\cosh^2\psi),\\
A_2 &= -2,\\
A_3 &= (-1)\cdot\cos\Phi\cdot\sinh 2\psi,\\
A_4 &= (+1)\cdot\cos 2\Phi\cdot\sinh^2\psi,\\
A_5 &= (-2)\cdot\sin\Phi\cdot\sinh\psi\cdot\lambda_e,\\
A_6 &= (-2)\cosh\psi\cdot\lambda_e,\\
A_7 &= (+2)\cdot\cos\Phi\cdot\sinh\psi\cdot\lambda_e,\\
A_8 &= (+1)\cdot\sin\Phi\cdot\sinh 2\psi,\\
A_9 &= (-1)\cdot\sin 2\Phi\cdot\sinh^2\psi.
\end{aligned} \quad (21)$$

There of the structure functions, namely $F_k, G_k, H_k, I_k\ (k=5,8,9)$ are zero at order α_s of perturbation theory. All these structure functions are odd functions of Φ: either $\sin\Phi$, or $\sin 2\Phi$.

By applying the method described above, we finally obtain the cross section for the large- p_T hadron production in DIS in the following form:

$$\begin{aligned}
\frac{d\sigma}{dx_B dQ^2 dz_B dq_T^2 d\Phi} = \frac{\alpha_e^2}{16\pi x_B^2 s^2 Q^2}\{&[(1+\cosh^2\psi)(F_1+\lambda_N\lambda_B I_1) - 2(F_2+\lambda_N\lambda_B I_2) -\\
&-\cos\Phi\cdot\sinh 2\psi(F_3+\lambda_N\lambda_B I_3) + \cos 2\Phi\sinh^2\psi(F_4+\lambda_N\lambda_B I_4) -\\
&-2\cosh\psi\cdot\lambda_e(\lambda_N G_6+\lambda_B H_6) + 2\cosh\psi\cdot\sinh\psi\cdot\lambda_e(\lambda_N G_7+\lambda_B H_7)\},
\end{aligned} \quad (22)$$

The effective section (22) contains 4 unpolarized (F_1, F_2, F_3 and F_4) and 8 polarized ($I_1, I_2, I_3, I_4, G_6, G_7, H_6, H_7$)SF. Let's discuss the possibilities of information obtaining about those and other functions. SF depend on Q^2, x_B, q_T^2 and z_B variables, that's why the experimental study of baryon azimuthal distribution over Φ allows us to define SF F_1, F_2, F_3 and F_4. For example, azimuthal angle symmetries

$$< cos\Phi >= -\frac{(2-y)\sqrt{1-y}F_3}{[1+(1-y)^2]F_1 - y^2F_2}, \tag{23}$$

$$< cos2\Phi >= \frac{(1-y)F_4}{[1+(1-y)^2]F_1 - y^2F_2} \tag{24}$$

are information sources about SF F_3 and F_4, here $y = \frac{Q^2}{x_B s}$ variable is introduced.

The degree of baryon longitudinal polarization at deep-inelastic scattering of longitudinal polarized electron on unpolarized nucleon is obtained as follows:

$$P(\lambda_e,\Phi) = \frac{d\sigma(\lambda_e,\lambda_B=1) - d\sigma(\lambda_e,\lambda_B=-1)}{d\sigma(\lambda_e,\lambda_B=1) + d\sigma(\lambda_e,\lambda_B=-1)} =$$
$$= \lambda_e \cdot \frac{-y(2-y)H_6 + 2y\sqrt{1-y}H_7 \cdot cos\Phi}{[1+(1-y)^2]F_1 - y^2F_2 - 2(2-y)\sqrt{1-y}F_3 cos\Phi + 2(1-y)F_4 \cdot cos2\Phi} \tag{25}$$

It can give the information about polarized SF H_6 and H_7.

At scattering of longitudinal polarized electron on polarized nucleon, the two-spin symmetry

$$A(\Phi) = \frac{d\sigma(\lambda_e,\lambda_N=1) - d\sigma(\lambda_e,\lambda_N=-1)}{d\sigma(\lambda_e,\lambda_N=1) + d\sigma(\lambda_e,\lambda_N=-1)} =$$
$$= \frac{-y(2-y)G_6 + 2y\sqrt{1-y}H_7 cos\Phi}{[1+(1-y)^2]F_1 - y^2F_2 - 2(2-y)\sqrt{1-y}F_3 \cdot cos\Phi + 2(1-y)F_4 cos2\Phi} \tag{26}$$

contains the information about polarized SF G_6 and G_7.

The degree of baryon longitudinal polarization at deep-inelastic scattering of longitudinal polarized electron on unpolarized nucleon is the information source about polarized SF I_1, I_2, I_3 and I_4:

:

$$P(\lambda_N,\Phi) = \frac{d\sigma(\lambda_N,\lambda_B=1) - d\sigma(\lambda_N,\lambda_B=-1)}{d\sigma(\lambda_N,\lambda_B=1) + d\sigma(\lambda_N,\lambda_B=-1)} =$$
$$= \lambda_N \frac{[1+(1-y)^2]I_1 - y^2I_2 - 2(2-y)\sqrt{1-y}I_3 \cdot cos\Phi + 2(1-y)I_4 cos2\Phi}{[1+(1-y)^2]F_1 - y^2F_2 - 2(2-y)\sqrt{1-y}F_3 \cdot cos\Phi + 2(1-y)F_4 cos2\Phi} \tag{27}$$

It is necessary to note that SF of hadrons don't depend on azimuthal angle of baryon takeoff, therefore they are easily defined by integration over the angle of Φ of baryon longitudinal polarizations degrees $P(\lambda_e)$, $P(\lambda_N)$ and two-spin symmetry A:

$$P(\lambda_e) = -\lambda_e \frac{y(2-y)H_6}{[1+(1-y)^2]F_1 - y^2F_2}, \tag{28}$$

$$P(\lambda_N) = \lambda_N \frac{[1+(1-y)^2]I_1 - y^2I_2}{[1+(1-y)^2]F_1 - y^2F_2}, \tag{29}$$

$$A = -\frac{y(2-y)G_6}{[1+(1-y)^2]F_1 - y^2F_2}, \tag{30}$$

Within frameworks of perturbation QCD we define SF of hadrons and carry out the evaluations of longitudinal polarization degrees $P(\lambda_e)$ and $P(\lambda_N)$.

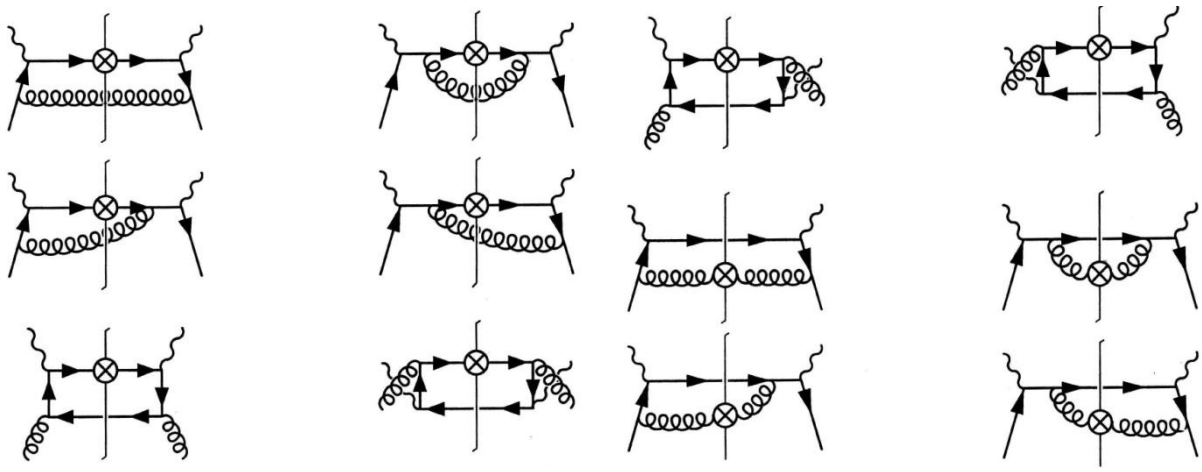

Fig. 3.

Lowest order diagram in the QCD coupling relevant for the processes (1) is shown in Fig. 3. The leading twist-2 contribution to the hadronic tensor $W^{\mu\nu}$ can be written as

$$W^{\mu\nu}(P,P_B,q)=\int_0^1\frac{dx}{x}\int_0^1\frac{dz}{z}\boldsymbol{Tr}[M_A(x,P,\lambda_N)\hat{M}_B(z,P_B,\lambda_B)H^{\mu\nu}(xP,P_B/z,q)]\times$$
$$\times 2\pi\delta((xP+q-P_B/z)^2) \tag{31}$$

where $M_A(x,P,\lambda_N)$ and $M_B(z,P_B,\lambda_B)$ are the distribution and fragmentation functions for nucleon N and baryon B, respectively, and $H^{\mu\nu}(xP_N,P_B/z,q)$ is the corresponding hard part. ***Tr*** indicates the trace over relevant spinor. Since we are interested in the twist-2 cross sections, P and P_B can be regarded as light-like to define the complete set of distribution and fragmentation functions, we introduce another set of vectors $n(n^2=0)$ and $\omega(\omega^2=0)$ for P and P_B, respectively, by the relation $(Pn)=1$ and $(P_B\omega)=1$. The complete set of the twist-2 quark distribution for the proton is defined as [14].

$$M_{ij}^q(x,P,\lambda_N)=\int\frac{d\lambda}{2\pi}e^{i\lambda x}<P\lambda_N|\overline{\psi}_j(0)\psi_i(\lambda n)|P\lambda_N>==\frac{1}{2}\hat{P}q(x)+\frac{1}{2}\lambda_N\gamma_5\hat{P}\Delta q(x)+\ldots, \tag{32}$$

where $q(x)$ and $\Delta q(x)$ are, respectively, spin-average and longitudinally polarized quark distribution.

The gluon distribution is also defined as [14]

$$M_g^{\alpha\beta}(x,P,\lambda_N)=\frac{2}{x^2}\int\frac{d\lambda}{2\pi}e^{i\lambda x}<P\lambda_N|\boldsymbol{tr}[n_\rho G^{\rho\alpha}(0)n_\sigma G^{\sigma\beta}(\lambda n)]|P\lambda_N>=$$
$$=-\frac{1}{2x}G(x)g_{A\perp}^{\alpha\beta}-\frac{1}{2x}\Delta G(x)i\varepsilon^{\alpha\beta\rho\sigma}P_\rho n_\sigma, \tag{33}$$

where $G^{\rho\alpha}$ is the gluon's field strength, ***tr*** means the trace over the color index for $G^{\rho\alpha}$, $g_{A\perp}^{\alpha\beta}=g^{\alpha\beta}-P^\alpha n^\beta-n^\alpha P^\beta$, $G(x)$ and $\Delta G(x)$ are, respectively, spin-average and longitudinally polarized gluon distributions.

Similarly we define twist-2 quark and gluon fragmentation functions for the spin $-1/2$ baryon B [14]:

$$M_{Bij}^q(z,P_B,\lambda_B)=\frac{1}{N_C}\sum_X\int\frac{d\lambda}{2\pi}e^{-i\lambda/z}<0|\psi_i(0)|BX><BX|\overline{\psi}_j(\lambda\omega)|0>=$$
$$=\frac{1}{z}\hat{P}_B q(z)+\frac{1}{z}\lambda_B\gamma_5\hat{P}_B\Delta q(z), \tag{34}$$

$$M_B^{g\alpha\beta}(z,P_B,\lambda_B)=\frac{2z^2}{N_C^2-1}\sum_X\int\frac{d\lambda}{2\pi}e^{-i\lambda/z}<0\left|\mathbf{tr}[\omega_\rho G^{\rho\alpha}(0)\right|BX><BX\left|\omega_\sigma G^{\sigma\beta}(\lambda\omega)]\right|0>= \\ =-G(z)g_{B\perp}^{\alpha\beta}-\Delta G(z)i\varepsilon^{\alpha\beta\rho\sigma}P_{B\rho}\omega_\sigma, \tag{35}$$

where $g_{B\perp}^{\alpha\beta}=g^{\alpha\beta}-P_B^\alpha\omega^\beta-\omega^\alpha P_B^\beta$.

By applying the method described above, we finally obtain the SF for the large- p_T baryon production in DIS in the following form:

$$F_k(G_k,H_k,I_k)=\alpha_S\int_{x_{min}}^1\frac{dx}{x}\int_{z_h}^1\frac{dz}{z}f_k(g_k,h_k,i_k)\delta\left(\frac{q_T^2}{Q^2}-\left(\frac{1}{\hat{x}}-1\right)\left(\frac{1}{\hat{z}}-1\right)\right), \tag{36}$$

In (35) $f_k(g_k,h_k,i_k)$ should read the following form $(C_F=4/3)$:

$$f_k=\sum_q e_q^2\{q(x)q(z)f_k^{qq}+G(x)q(z)f_k^{gq}+q(x)G(z)f_k^{qg}\}, \tag{37}$$

$$g_k=\sum_q e_q^2\{\Delta q(x)q(z)g_k^{qq}+\Delta G(x)q(z)g_k^{gq}+\Delta q(x)G(z)g_k^{qg}\}, \tag{38}$$

$$h_k=\sum_q e_q^2\{q(x)\Delta q(z)h_k^{qq}+G(x)\Delta q(z)h_k^{gq}+q(x)\Delta G(z)h_k^{qg}\}, \tag{39}$$

$$i_k=\sum_q e_q^2\{\Delta q(x)\Delta q(z)i_k^{qq}+\Delta G(x)\Delta q(z)i_k^{gq}+\Delta q(x)\Delta G(z)i_k^{qg}\}, \tag{40}$$

$$f_1^{qq}=2C_F\hat{x}\hat{z}\left[\frac{1}{Q^2q_T^2}\left(\frac{Q^4}{\hat{x}^2\hat{z}^2}+(Q^2-q_T^2)^2\right)+6\right],$$

$$f_2^{qq}=2f_4^{qq}=8C_F\hat{x}\hat{z},$$

$$f_3^{qq}=4C_F\hat{x}\hat{z}\frac{1}{Qq_T}(Q^2+q_T^2),$$

$$f_1^{gq}=\hat{x}(1-\hat{x})\left[\frac{Q^2}{q_T^2}\left(\frac{1}{\hat{x}^2\hat{z}^2}-\frac{2}{\hat{x}\hat{z}}+2\right)+10-\frac{2}{\hat{x}}-\frac{2}{\hat{z}}\right],$$

$$f_2^{gq}=2f_4^{gq}=8\hat{x}(1-\hat{x}),$$

$$f_3^{gq}=\hat{x}(1-\hat{x})\frac{2}{Qq_T}\left[2(Q^2+q_T^2)-\frac{Q^2}{\hat{x}\hat{z}}\right],$$

$$f_1^{qg}=2G_F\hat{x}(1-\hat{z})\left[\frac{1}{Q^2q_T^2}\left(\frac{Q^2}{\hat{x}^2\hat{z}^2}+\frac{(1-\hat{z})^2}{\hat{z}^2}\left(Q^2-\frac{z^2q_T^2}{(1-\hat{z})^2}\right)\right)+6\right],$$

$$f_2^{qg}=2f_4^{qg}=8C_F\hat{x}(1-\hat{z}),$$

$$f_3^{qg}=4C_F\hat{x}(1-\hat{z})^2\frac{1}{\hat{z}Qq_T}\left[Q^2+\frac{\hat{z}^2q_T^2}{(1-\hat{z})^2}\right]; \tag{41}$$

$$g_6^{qq}=-2C_F\left[\left(\frac{1}{\hat{x}\hat{z}}+\hat{x}\hat{z}\right)\frac{Q^2}{q_T^2}-\frac{\hat{x}\hat{z}q_T^2}{Q^2}\right],$$

$$g_7^{qq}=-4C_F\hat{x}\hat{z}\frac{Q^2-q_T^2}{Qq_T},$$

$$g_6^{gq}=-\frac{2\hat{x}-1}{\hat{x}}\left(2\hat{x}+\frac{\hat{x}-1}{\hat{z}^2}\cdot\frac{Q^2}{q_T^2}\right),$$

$$
\begin{aligned}
g_7^{qq} &= -2\frac{Q}{q_T}\cdot\frac{(\hat{x}-1)(2\hat{z}-1)}{\hat{z}},\\
g_6^{qg} &= 2C_F\frac{\hat{z}}{\hat{x}-1}\left[\frac{1}{\hat{z}^2}-(\hat{x}-1)^2+\frac{\hat{x}^4}{(\hat{x}-1)^2}\cdot\frac{q_T^4}{Q^4}\right],\\
g_7^{qg} &= 4C_F\frac{\hat{x}\hat{z}}{\hat{x}-1}\left(1-\frac{\hat{x}}{\hat{z}}\right)\cdot\frac{q_T}{Q}.
\end{aligned}
\tag{42}
$$

$$
\begin{aligned}
h_{6,7}^{qq} &= g_{6,7}^{qq},\\
h_6^{qq} &= \frac{2\hat{x}^2-2\hat{x}+1}{\hat{x}\hat{z}}\left(\hat{x}+(\hat{x}-1)\frac{Q^2}{q_T^2}\right),\\
h_7^{qq} &= 2\frac{Q}{q_T}\frac{(\hat{x}-1)(2\hat{x}-1)}{\hat{z}},\\
h_6^{qg} &= 2C_F\frac{\hat{z}}{\hat{x}-1}\left[\frac{1}{\hat{z}^2}+(\hat{x}-1)^2-\frac{\hat{x}^4}{(\hat{x}-1)^2}\cdot\frac{q_T^4}{Q^4}\right],\\
h_7^{qg} &= -4C_F\frac{\hat{x}\hat{z}}{\hat{x}-1}\left(1-\frac{\hat{x}}{\hat{z}}\right)\cdot\frac{q_T}{Q},
\end{aligned}
\tag{43}
$$

$$
\begin{aligned}
i_k^{qq} &= f_k^{qq}\ (k=1,2,3,4),\\
i_1^{qq} &= \frac{2\hat{x}-1}{\hat{x}(\hat{x}-1)}\frac{Q^4(\hat{x}-1)^2-q_T^4\hat{x}^2}{Q^2q_T^2},\\
i_3^{qq} &= \frac{2}{Qq_T}[Q^2(\hat{x}-1)-q_T^2\hat{x}],\\
i_1^{qg} &= 2C_F\hat{x}\hat{z}\left[\frac{\hat{x}-2}{\hat{x}-1}+\frac{\hat{x}(\hat{x}+1)}{(\hat{x}-1)^2}\frac{q_T^4}{Q^4}+\frac{2(2\hat{x}^2-2\hat{x}+1)}{(\hat{x}-1)^2}\frac{q_T^2}{Q^2}\right],\\
i_2^{qg} &= 2i_4^{qg} = 8C_F\frac{\hat{x}^2\hat{z}}{\hat{x}-1}\cdot\frac{q_T^2}{Q^2},\\
i_3^{qg} &= 4C_F\frac{\hat{x}\hat{z}}{(\hat{x}-1)^2}\cdot\frac{q_T}{Q}\left[(\hat{x}-1)^2+\hat{x}^2\frac{q_T^2}{Q^2}\right]
\end{aligned}
\tag{44}
$$

We introduced the variables:

$$\hat{x}=\frac{x_B}{x},\quad \hat{z}=\frac{z_B}{z}, \tag{45}$$

and

$$x_{min}=x_B\left(1+\frac{z_B}{1-z_B}\cdot\frac{q_T^2}{Q^2}\right). \tag{46}$$

For a given s, Q^2 and q_T, the kinematic constraint for x_B and z_B is

$$\frac{Q^2}{s}<x_B<1, \tag{47}$$

$$0<z_B<\frac{1-x_B}{1-x_B(1+q_T^2/Q^2)}. \tag{48}$$

For a given Q^2, x_B and z_B, q_T can take

$$0<q_T<Q\sqrt{\left(\frac{1}{x_B}-1\right)\left(\frac{1}{z_B}-1\right)}. \tag{49}$$

The structure functions F_1, I_1, G_6 and H_6 have a $1/q_T^2$ behavior, these terms arise from the emission of partons that are collinear to the incoming parton, collinear to the outgoing parton, or soft. The functions F_3, G_7, H_7 and I_3 gives contributions are of order $1/q_T$.

In the semi-inclusive DIS, contribution from the gluon distribution and fragmentation functions is of the same $O(\alpha_s)$ effect as the quark contribution, so that q_T-differential cross section is expected to be a more sentitive tool to determine detailed form of the polarized gluon contribution than the q_T-integrated case.

4. NUMERICAL ESTIMATE

The polarizations $P(\lambda_e), P(\lambda_B)$ and asymmetry A

are still functions of five variables: s, Q^2, x_B, z_B and q_T. We estimate them at COMPASS $(s = 300\,GeV^2)$ and EIC $(s = 10^4\ GeV^2)$ energies. We have chosen $(Q^2, x_B) = (100\,GeV^2, 0.45)$ for the COMPASS energy and $(Q^2, x_B) = (100\,GeV^2, 0.015)$ for the EIC energy. We use GRV parton density for the unpolarized nucleon [16], GRSV polarized parton density [17] and FSV Λ-fragmentation functions [18] for polarized and unpolarized Λ.

Figure 4 shows the q_T-dependence and z_B-dependence of the longitudinal polarization $P(\lambda_e)$ for $e + p \Rightarrow e + \Lambda + X$ ((*a*) and (*b*)) at the COMPASS kinematics.

Figure 5 shows the same polarizations as Fig. 4 but for the EIC kinematics. In [18], three sets of polarized fragmentation function for Λ baryon have been constructed. Scenario 1 corresponds to the nonrelativistic quark model picture, where only polarized s-quark is assumed to fragment into the polarized Λ, i. e., $\Delta u(z) = \Delta d(z) = 0$. Scenario 2 and 3 assumes that $-\Delta u(z) = -\Delta d(z) = 0{,}2\Delta s(z)$ and $\Delta u(z) = \Delta d(z) = \Delta s(z)$. In scenario 1 in which only s-quark fragments into Λ-hyperon gives negligible polarization, while scenarios 2 and 3 gives, respectively, negative and positive polarizations, the former being smaller in magnitude.

Figures 6 and 7 show the polarization $P(\lambda_B)$ at the COMPASS and EIC kinematics, respectively

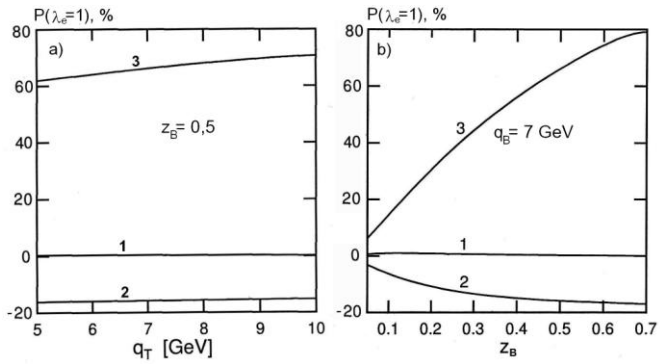

Fig. 4. The longitudinal polarization $P(\lambda_e = 1)$ for $e + p \to e + \Lambda + X$ at the COMPASS energy. (a) and (b) show the $q_T -$ dependence and the z_B-dependence for scenarios 1, 2, 3

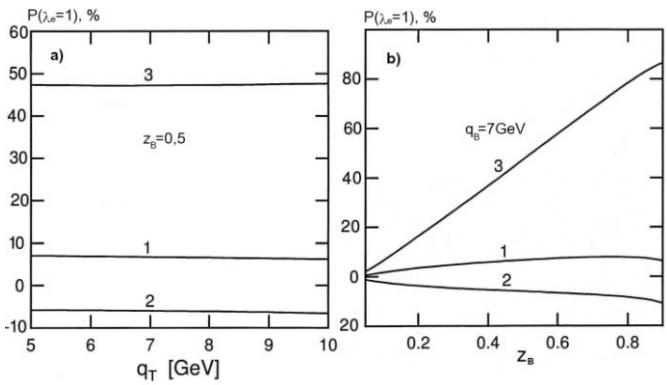

Fig. 5. The same as Fig. 4 but for EIC energy

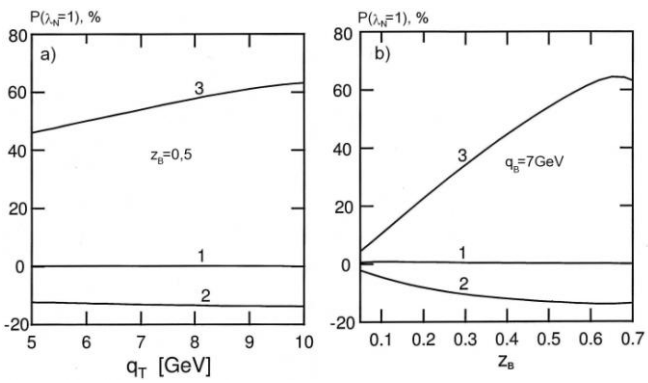

Fig. 6. The longitudinal polarization $P(\lambda_N = 1)$ for $e + p \to e + \Lambda + X$ at the COMPASS energy. (a) and (b) show the $q_T -$ dependence and the z_B-dependence for scenarios 1, 2, 3

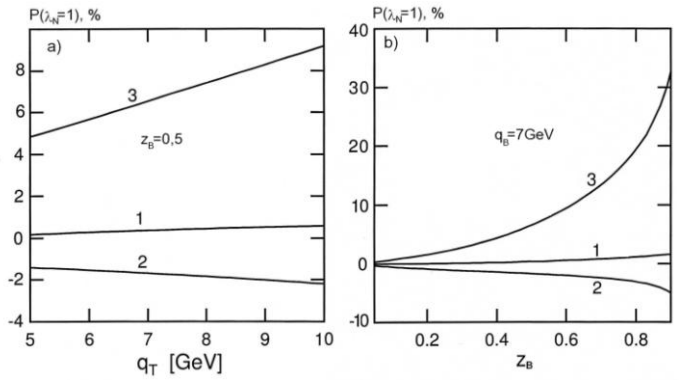

Fig. 7. The same as Fig. 6 but for EIC energy

[1] *V. Barone, S. Melis, A. Prokudin.* Boer-Mulders effect in unpolarized SIDIS: An analysis of the COMPASS and HERMES data on the cos2ϕ asymmetry // Phys. Rev. D, 2010, N81, p.114026-1-9.

[2] *D.De Florian, G.A. Navarro, R. Sassot.* Sea quarks and gluon polarization in the nucleon at NLO accuracy // Phys. Rev. D71, 2005, 094018-1-12.

[3] *P.J. Mulders.* Polarized structure functions // Progress in Particle and Nuclear Physics, 2005, N55, p.243-269.

[4] *V. Barone, A. Prokudin, Ma B.-Q.* Systematic phenomenological study of the cos2ϕ asymmetry in unpolarized semi-inclusive DIS // Phys. Rev. D, 2008, N78, p.045022-1-10.

[5] *M. Arneodo* et al. Measurement of Hadron Azimuthal Distributions in Deep Inelastic Muon Proton Scattering. (European Muon Collaboration) // Z. Phys. C34: 277, 1987.

[6] *J. Breitweg* et al. Measurement of azimuthal asymmetries in deep inelastic scattering // Phys. Lett. B 481, 199-212, 2000, e-Print Archive: hep-ex/0003017.

[7] *W. Käfer.* Measurements of Unpolarized Azimuthal Asymmetries at COMPASS // In proceedings for Transversity, 2008, pp.169-176.

[8] *A. Bressan.* Azimuthal asymmetries in SIDIS off unpolarized targets at COMPASS. arXiv:0907.5511v1.

[9] *A. Giordano, R. Lamb.* Measurement of azimuthal asymmetries of the unpolarized cross section at HERMES // AIP Conf. Proc. 1149: 423-426, 2009.

[10] *S.K. Abdullayev, A.I. Mukhtarov, M.Sh. Gojayev.* The longitudinal polarization of B-barion in semi-inclusive reactions // Azerbaijan Journal of Phys., Fizika. Bakı, 2010, №3-4, p.70-78.

[11] *S.K. Abdullayev, A.I. Mukhtarov , M.Sh. Gojayev.* Double spin asymmetries for hadron production in semiinclusiv DIS // Fizika, 2009, N.1, p.61-67.

[12] *S.K. Abdullaev, A.I. Muxtarov, M.Sh. Gojayev.* Bakı Universitetinin Xəbərləri. Fizika-riyaziyyat elmləri seriyası. 2002, №4, s.5-11. (in Russian).

[13] *S.K. Abdullaev, M.Sh. Gojayev.*Bakı Universitetinin Xəbərləri. Fizika-riyaziyyat elmləri seriyası. 2011, №3, s.167-176. (in Russian).

[14] *Y. Koike, J. Nagashima.* Double spin asymmetries for large-p_T hadron production in semi-inclusive DIS // arxiv: hep-ph/0302061 V2, 2003, p.1-25.

[15] *A. Mendez.* QCD predictions for semi-inclusive and inclusive leptoproduction // Nucl. Phys. B145, 1978, p.199-220

[16] *R. Meng, F.I. Olness, D. Soper.* Semi-Inclusive Deeply Inelastic Scattering at electron-proton colliders // Nucl. Phys. B371, 1992, p.79-110

[17] *M. Glück , E. Reya , A. Vogt.* Dynamical Parton Distributions Revisited // Eur. Phys. J. C5, 1998, p.461-470.

[18] *D.De Florian, M. Stratman, W. Vogelsang.* QCD analysis of unpolarized and polarized Λ-baryon production in leading and next-to leading order // Phys. Rev. D63, 1998, p.5811-5824.

[19] *M. Glück, E. Reya, M. Stratmann and W. Vogelsang.* Models for the Polarized Parton Distributions of the Nucleon // Phys. Rev. D63, 2001, 094005.

Received: 31.01.2011

DIELECTRIC PROPERTIES OF DUAL-FREQUENCY LIQUID CRYSTAL 5CB- C2-H22

T.D. IBRAGIMOV, A.K. MAMEDOV
H.M.Abdullayev Institute of Physics of Azerbaijan National Academy of Sciences
AZ1143 H.Javid Avenue, 33, Baku, Azerbaijan

G.M. BAYRAMOV
Baku State University
AZ1148 Z.Khalilov str, 23, Baku, Azerbaijan

The novel dual-frequency liquid crystal (LC) consisting of LC 4-n-pentyl-4'-cyanobiphenyl (5CB) with positive dielectric anisotropy and two LCs 4-hexyloxyphenyl ester 4'-hexyloxy-3-nitrobenzoic acid (C2) and 4-n-pentanoyloxy-benzoic acid-4'-hexyloxyphenyl ester (H 22) with negative dielectric anisotropies was developed. Meanwhile, the interval of the LC phase of the mixture was extended within 11 - 65 °C. Temperature dependences of dielectric permeability components of the 5CB- C2-H22 mixture and also the crossover frequency were defined. It was shown that an increase in temperature of the sample leads to reduction of perpendicular component of dielectric permeability and an increase in crossover frequency. The last is characterized by the activation energy connected with rotations of the long molecular axes.

Keywords: dual-frequency liquid crystal, crossover frequency, activation energy, permeability
PACS: 77.84.Nh, 78.28.Jq, 61.30.Gd, 61.30.Eb

INTRODUCTION

Optical properties of a well-aligned layer of a liquid crystal (LC) are characterized by extraordinary n_e and ordinary $\mathbf{n}_o$ refractive indices. Meanwhile, the difference $\Delta\varepsilon$ between dielectric permeabilities $\varepsilon_{\|}$ and $\varepsilon_{\perp}$, corresponding to extraordinary and ordinary refractive indices, defines dielectric anisotropy of the LC. It is necessary to note that $\varepsilon_{\|}$ and $\varepsilon_{\perp}$ are components of the dielectric permeability measured along and perpendicular to the direction of LC long molecular axes called by the director.

Dual-frequency liquid crystal (DFLC) represents a mixture consisting of molecules of liquid crystals with positive and negative dielectric anisotropies. The sign of dielectric anisotropy of such mixture can change from positive to negative magnitudes at a change of electric field frequency. Possibility of sign inversion of dielectric anisotropy on some crossover frequency f_t allows operating the switching processes in LC. Meanwhile, dielectric anisotropy on low frequencies $(f < f_t)$ has a positive sign and it has negative one at high frequencies $(f > f_t)$. With an increase of the applied electric field frequency, $\varepsilon_{\|}$ decreases while $\varepsilon_{\perp}$ remains invariable. Thus, there is a reorientation of molecular dipoles of LC with the positive dielectric anisotropy in parallel to an electric field vector at application of low frequency field to the DFLC layer with the parallel-directed orientation of molecules. The application of voltage with the high frequency causes reorientation of molecular dipoles of LC molecules with negative dielectric anisotropy in orthogonal direction to the vector of electric field. As a result, there is a process of a relaxation of molecules and returning of LC director to the starting position.

Use of DFLC expands a span of electrooptical effects and possibility of application of LC in various electrooptical devices. In particular, the DFLC system in combination with the polymer, having refractive index equal to ordinary refractive index of LC, allows operating the transmission of an electrooptical cell [1]. The small particles – DFLC system is used for a filtration and modulation of infra-red radiation [2-4].

In work [5] it is informed about obtaining of plasmon modulators of high-contrast signals based on DFLC in work [5]. Authors of paper [6] have developed DFLC with high two-refraction and ultralow crossover frequency which can be used at the elevated temperatures. The method of phase modulation with the high speed using dual-frequency liquid crystals is described in work [7]. This system uses an electronic feedback connection in order to simplify the control. For large phase shifts, phase modulation speeds are an order of magnitude faster than for existing techniques. Thus, synthesis of the two-frequency liquid crystal mixture possessing a wide temperature interval of the mesogene phase, great magnitudes of dielectric anisotropy, low value of crossover frequency and small switching times will create possibilities not only for improvement of operated characteristics of existing electrooptical devices but also designing of novel type of similar devices.

In the given work, the results of study of dielectric parameters of the novel synthesized dual-frequency liquid crystal are reported.

EXPERIMENTAL

Three-component mixture of following liquid crystals was used for obtaining of dual-frequency LC:
4-n-pentyl-4'-cyanobiphenyl (5CB) with $\Delta\varepsilon = +11.5$, sequence of phase transitions Cr 18°C N 35,2°C I, and structural formula

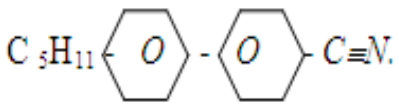

4-hexyloxyphenyl ester 4'-hexyloxy-3-nitrobenzoic acid (C2) with $\Delta\varepsilon = -8.5$, sequence of phase transitions Cr 36°C S_A 71°C I, and structural formula

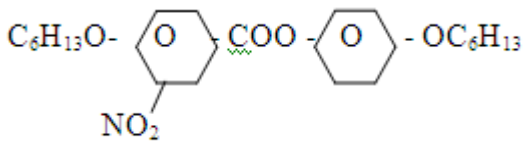

4-n-pentanoyloxy-benzoic acid-4'-hexyloxyphenyl ester (H 22) with Δε= -2.6, sequence of phase transitions Cr 44°C N 75°C I, and structural formula

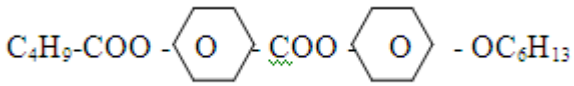

and molar ratio of 1: 1: 1.5, correspondingly. Observation under polarization microscope showed that the mixture has nematic phase in the temperature range of 11-65º C.

A study of frequency dependence of dielectric permeability of a mixture 5CB - C2 - H22 was carried out in cells with substrates from conductive glasses. Meanwhile, dependences $\varepsilon_\perp$ and $\varepsilon_{||}$ on frequency were measured with working voltage nearby 1 V at planar and homeotropic orientations of LC molecules, accordingly. Planar orientation of molecules was reached by following manners. The polyamide lacquer was dissolved in dimethyl formamide (5 % solution) and passed through the glass filter. The drop of the obtained solution was put on a plate surface and the system rotated in a centrifuge with frequency of 3000 rpm for a uniform covering. After solvent drying in the drying cupboard, plates were maintained at the temperature 300°C within 0,5 hours . After this stage of heat-treatment (-polymerization), uniform film of a polyamide lacquer was formed on a substrate surface. Then the film is rubbed by means of a fabric. For obtaining of the homeotropic orientation of LC molecules, a drop of the soap solution of 1% in hot (60ºC) water fells on a hot substrate from an electrode (SnO_2) which rotated in a centrifuge with frequency 20 s^{-1}. After that the substrate was dried up in siccative cupboard.

The cell was filled by LC in the isotropic phase and was located in special oven. A temperature of the cell with LC was measured by the copper-constantan thermocouple with accuracy of 0.5°*C*. Dielectric permeability was defined from the relation of capacities of the filled and empty cells which in their turn, were measured on the device BM 560 Tesla.

RESULTS AND DISCUSSION

Frequency dependence of dielectric permeabilities $\varepsilon_\perp$ and $\varepsilon_{||}$ of the mixture 5CB - C2 - H22 at temperature 23ºC is shown on Fig. 1. The dispersion of $\varepsilon_\perp$ occurs at very high frequencies (~ 1 MHz), which is connected with a relaxation of dipole groups –COO. Two dispersions are observed for $\varepsilon_{||}$. The first of them corresponds to longitudinal component of group - NO_2 which begins directly at low frequencies (~1 kHz). The second relaxation, which occurs at frequencies of 100 kHz, corresponds to relaxation of dipole groups-C≡N. The point of crossing of dispersive curves (crossover frequency) corresponds to transition of the mixture from the state of positive dielectric anisotropy to negative one and makes up 104 кHz at temperature 23ºC.

Temperature dependence of $\varepsilon_\perp$ is shown in Fig.2.

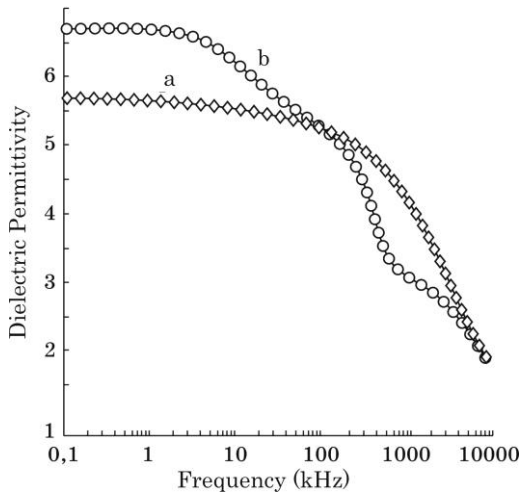

Fig.1. Frequency dependence of dielectric permeabilities $\varepsilon_{||}$ (a) and $\varepsilon_\perp$ (b) of the mixture 5CB – C2 – H22 at temperature 23ºC.

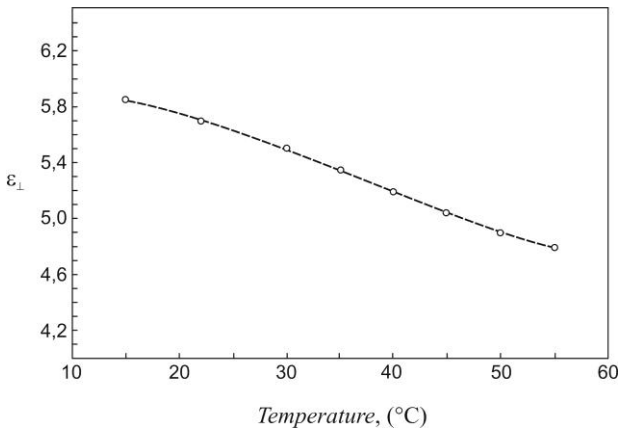

*Fig.2.*Temperature dependence of dielectric permittivity component $\varepsilon_\perp$ of the mixture 5CB – C2 – H22 on the frequency of 40 kHz.

As seen from this figure, an increase in temperature of the sample 5CB - C2 - H22 results in reduction of perpendicular component of dielectric permeability. Temperature dependence of crossover frequency is shown on Fig.3. Apparently, it increases from 90 kHz to 300 kHz at change of temperature from 15°C to 50°C.

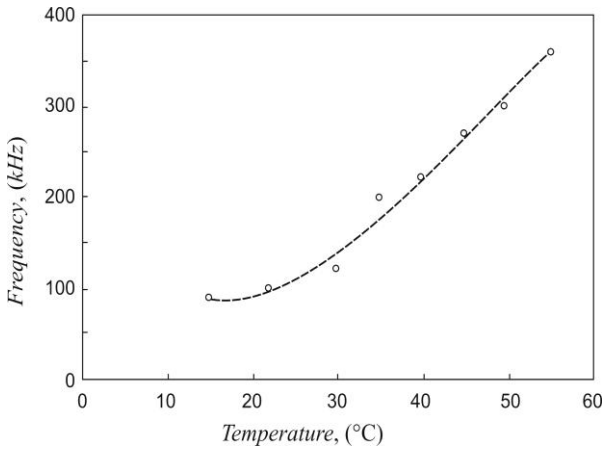

Fig.3. Temperature dependence of crossover frequency of a mixture 5CB - C2 - H22.

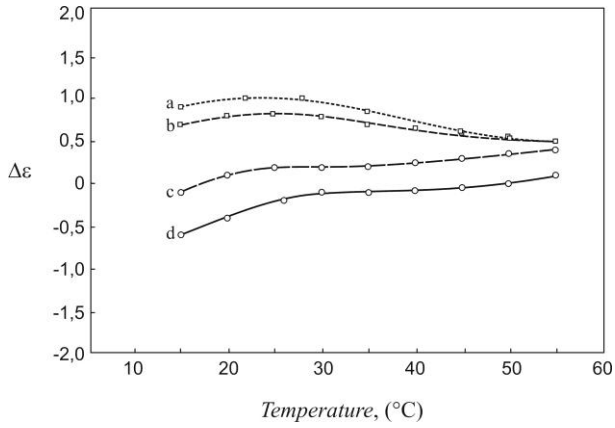

Fig. 4. Dielectric anisotropy as function of temperature of the cell at various frequencies of the applied electric field: a is 50 kHz; b is 100 kHz; c is 200 kHz; d is 300 kHz.

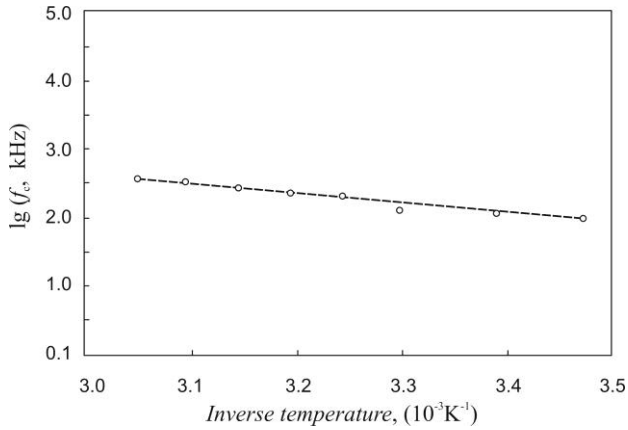

Fig. 5. Crossover frequency f_c versus the inverse temperature 1/T.

Δε is always positive in a wide frequency range of the applied electric voltage (Fig.4) at high temperatures.

Temperature behavior of crossover frequency can be fitted by a straight line in the inverse-logarithmic coordinates (Fig. 5), that specifies on activation nature of the given change:

$$fc \sim \exp(-E_f/k_B T),$$

where k_B is the Boltzmann constant and E_f is the activation energy representing the energy barrier connected with rotations of the long molecular axes.

Extrapolation of the given straight line on the inverse temperature axis and linear fit field the magnitude of activation energy $E_f = 0.29$ *eV*.

CONCLUSION

The interval of LC phase of the developed novel dual-frequency LC, consisting of LC 5CB with positive dielectric anisotropy and two LCs with negative dielectric anisotropies C2 and H22, has been extended within 11 - 65 °C. Increasing temperature of the sample results in reduction of perpendicular component of dielectric permeability and an increase of crossover frequency. The last is characterized by the activation energy connected with rotations of the long molecular axes.

ACKNOWLEDGMENT

This work has been supported by Scientific and Technology Center in Ukraine (grants 4172 and 5352) and also in the framework of the Belarus-Azerbaijan project F10AZ-004.

[1] *Coates, David. Nolan, Patrick*. Electrooptical liquid crystal system containing dual frequency liquid crystal mixture. US Patent 5621552 (1997)

[2] *T.D. Ibragimov*. Cristiansen effect in the particles Al_2O_3 – liquid crystal system. Journal of Applied Spectroscopy. 76, 5 (2009)793-796.

[3] *T.D. Ibragimov, E.A. Allahverdiyev, G.M. Bayramov and A.R. Imamaliyev*, Selective modulation of infrared radiation by an Al_2O_3 particles - liquid crystal system, Journal of Applied Spectroscopy, 78 (2011) 445-449.

[4] *T.D. Ibragimov, G.M. Bayramov*. Novel type of tunable infrared filters based on the Al_2O_3 particles - liquid crystal system. Infrared Physics and Technology. V.54, No 6, (2011) 512-515.

[5] *Joseph S. T. Smalley, Yanhui Zhao, Ahmad Ahsan Nawaz, Qingzhen Hao, Yi Ma, Iam-Choon Khoo, and Tony Jun Huang*. High contrast modulation of plasmonic signals using nanoscale dual-frequency liquid crystals. Optics Express. Vol. 19, No. 16 (2011) 15265-15274

[6] *Haiqing Xianyu[a]; Xiao Liang[b]; Jie Sun[a]; Shin-Tson Wu.* 'High performance dual frequency liquid crystal compounds and mixture for operation at elevated temperature. Liquid Crystals, 37, 12 (2010) 1493 — 1499.

[7] *Andrew K. Kirby and Gordon D. Love*. Fast, large and controllable phase modulation using dual frequency liquid crystals. Optics Express, 12, 7 (2004) 1470-1475.

Received: 29.12.2011

Δ^0 – RESONANCE PRODUCTION IN MULTI-NUCLEON π^{-12}C - INTERACTIONS AT THE MOMENTUM OF 40GeV/*c*

Y. H. HUSEYNALIYEV
Azerbaijan State Pedagogical University, Bakı/Azerbaijan
E-mail: yashartur@yahoo.com

The experimental results on properties of multi-nucleon $\pi^{-12}C-$ interactions at the momentum of p_π–=40GeV/c obtained from the 2m propane bubble chamber of the laboratory of High Energies of Joint Institute for Nuclear Research (Dubna, Russia) are discussed. To select the multi-nucleon $\pi^{-12}C-$ interactions the criterion is used that the number of identified protons with momentum p_p<1GeV/c is great or equal two in each event ($n_p \geq 2$). To analyze the properties of multi-nucleon $\pi^{-12}C-$ interactions the variable R is used. The values of the R as a ratio of the inclusive spectra of charged π -mesons and protons emitted in multi-nucleon events and in all ones are determined, i.e.

$$R = \frac{[1/N_{ev}(dN/dy)]_{n_p \geq 2}}{[1/N_{ev}(dN/dy)]_{\pi-12C}}.$$

As the characteristics of secondary particles the transverse momentum (p_t), cumulative number (β^0, the values of which are determined as $\beta^0 = (E - p_l)/M_N$, where E is a total energy, p_l is a longitudinal momentum and M_N is a nucleon mass), kinetic energy (T) and emission angle (θ) dependences (in laboratory frame) of the R are studied. The indications on occurrence of a Δ^0 – baryon resonance and relatively high contribution of deep-inelastic processes in multi-nucleon events are received.

Keywords: $\pi^{-12}C$, Δ^0 –baryon resonance, π –meson, proton, transverse momentum, cumulative number, kinetic energy, emission angle, effective mass distribution
PACS: 25.75.Gz, 25.75. q, 11.25.Hf, 123.1K, 13.85. –t, 25.80. e, 14.20. Gk

INTRODUCTION

Study of behavior of the characteristics in hadron-nucleus and nucleus-nucleus interactions as a function of collision centrality, Q, is an important experimental method for obtaining information on the phases of nuclear matter, because the increase in Q could lead to an increase in baryon density of nuclear matter. In other words, changes in the behavior of some centrality in dependence of characteristics of events will be a signal on the phase transition. This is considered the best method to achieve a phase of quark-gluon plasma of strongly-interacting nuclear matter. Some experimental results have demonstrated the existence of changes in behavioral characteristics of events as a function of the collision centrality [1-8].

The easiest option to set centrality is the use the number of protons emitted in the reactions to consider multi-nucleon processes. By studying the multi-nucleon events in hadron-nucleus and nucleus-nucleus interactions one can get useful information about collective phenomena, for example formation of bound states of the resonances in the nucleus. It should be noted that production of some baryon resonances has been studied in [9] in detail. Physics of these processes serves as a bridge that joins the study of mechanisms for the production of high-energy particles, and new phases of strongly - interacting nuclear matter. But there is one very important question: what are the criteria to separate the multi-nucleon processes in experiment? There another question is arising: can we extract resonance in an event using only particle characteristics and without using any method, which was done in [9]?

1. THE EXPERIMENTAL METHOD ON Π^{-12}C – INTERACTION

The experimental data were obtained using the 2m propane bubble chamber of the Laboratory of High Energies of Joint Institute for Nuclear Research (JINR) (Dubna, Russia) exposed to a beam of relativistic π^--mesons at 40GeV/*c* at Serpukhov Accelerator. The number of $\pi^{-12}C-$ interactions equals to 8791, where the corresponding inelastic cross section is $\sigma_{in} = (87.5 \pm 1.0)mb$ [10]. The methodological issues connected with the processing of the stereo photos, selection and identification of types of interactions in propane (C_3H_8), reconstruction of the kinematical characteristics of the secondary particles, their identification, and inclusion of corrections due to the loss of particles emitted under large angle to the object plane of a camera are described in details in [11-13]. Practically all secondaries, emitted at a 4π total solid angle, were detected in the chamber. A minimum momentum for pion registration was about 70MeV/c. Separation of protons and π^+ -mesons was done visually based on their ionization in region p<700MeV/c and protons were identified, since a momentum 140MeV/c at which the track starts to be precisely visible (length>3cm). The analysis on δ –electrons showed that the admixture of protons among the fast positive singly charged particles identified as π^+-mesons was 12±5% of the measured mean multiplicity of protons. It should be mentioned that π^- -

mesons make up the main fraction (>95%) among the negatively charged particles [14].

2. PROPERTY OF MULTI-NUCLEON π^{-12}C INTERACTIONS AT P_{π^-} = 40GEV/C

In this paper the inclusive properties of $\pi^{\pm}$ -mesons and protons production (with momentum P_p<1GeV/c) are studied by comparing data, when the number of protons is great or equal two (multi-nucleon event) with inclusive properties of all π^{-12}C events, i.e. from process

$$\pi^- + {}^{12}C \to np + n_1\pi^{\pm} + X \qquad (1)$$

(n is a number of protons with P_p<1GeV/c, n_1 is number $\pi^{\pm}$ -mesons, and X is all rest) is allocated process

$$\pi^- + {}^{12}C \to n'p + n_1'\pi^{\pm} + X' \qquad (2)$$

($n' \geq 2$ is a number of protons with P_p<1GeV/c, n_1' is a number of $\pi^{\pm}$ -mesons and X' is all rest in event) and inclusive properties of process (2) by means of variable $R^k(y)$ are compared with inclusive properties of process (1).

The variable $R^k(y)$ is defined as a ratio of inclusive spectra of particles of type k (k denotes $\pi^{\pm}$ -meson or proton) depending on a variable y received in process (2) to similar spectra, received in (1), i.e.

$$R^k(y) = \frac{(dN/dy)_2}{(dN/dy)_1}.$$

As the characteristics of secondary particles (y) the transverse momentum (p_t), cumulative number (β^0, the values of which is determined as $\beta^0 = (E - p_l)/M_N$, where E is a total energy, p_l is a longitudinal momentum and M_N is the nucleon mass), kinetic energy (T) and emission angle (θ) dependences (in laboratory frame) of the R are studied. The number of multi-nucleon $\pi^{-12}C$ – interactions equals to 3571. The interactions of the projectiles with "quasi-free" nucleons of the target were not taken into account.

The characteristics p_t, β^0 and T allow describing such parameters of nuclear substance, as the geometrical sizes of area of radiation, a mass and "temperature" of nuclear matter, accordingly. In addition, β^0 describes minimum target mass, by which an interaction takes place. Therefore, the values of $R^k(y)$, distinct from $\overline{n_1'}/\overline{n_1}$ in case of $\pi^{\pm}$ - mesons and from $\overline{n'}/\overline{n}$ in case of protons ($\overline{n_1}, \overline{n_1'}$, $\overline{n}$ and $\overline{n'}$ are the average values of n_1, n_1', n and n', accordingly), will be interpreted as manifestation of dynamic effects, related with multi-nucleon processes.

3. EXPERIMENTAL RESULTS

In fig.1a, b values of $R^k(p_t)$ (● -π^+-meson, ○ -π^- -meson and □ -proton) are presented. For the ratios $\overline{n_1'}/\overline{n_1}$ and $\overline{n'}/\overline{n}$ following values are found accordingly: 0.96±0.01 (for π^+ -meson, in figures it is shown by dashed lines); 1.05 ± 0.01 (for π^- -meson, in figures it is shown by dot lines); 1.81±0.02 (for proton, in figures it is shown by dashed-dot lines).

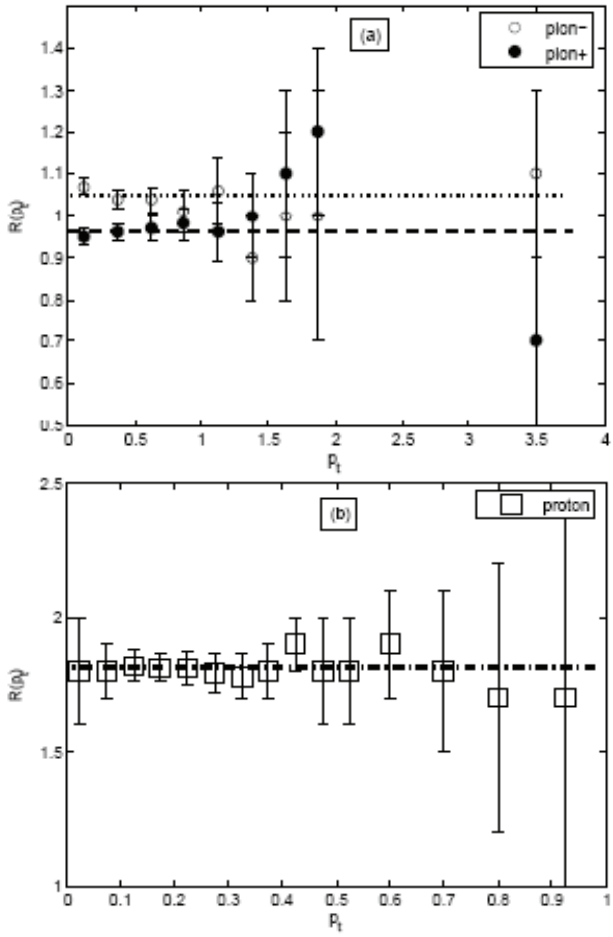

*Fig.1.*The $R(p_t)$ dependence for $\pi^{\pm}$ - mesons (a) and protons (b), emitted in $\pi^{-12}C$– interactions at p_{π^-}=40GeV/c.

Errors of ratios for different type of particles are shown by the empty or filled boxes near to lines whose values are given in the text at appropriate places. From fig.1a, b it is seen, that:

1.1) *for $\pi^{\pm}$ -mesons, the values of $R(p_t)$ does not differ from $\overline{n_1'}/\overline{n_1}$ at all values of p_t;*

1.2) *for protons, $R(p_t) \approx \overline{n'}/\overline{n}$ at all p_t.*

1.3) *in p_t > 0.75GeV/c, the $R(p_t)$ for π^+ - and π^- - mesons coincide (fig.1a).*

It means that emission of π -mesons practically independent of their sign of charge. The distribution of protons is also the same, but with different numerical

factor, 1.81 (fig.1b). The latter is due to the fact that, in the number of protons in multi-nucleon events selection is made ($n' \geq 2$).

According to data presented in fig.2a, b one can conclude, that

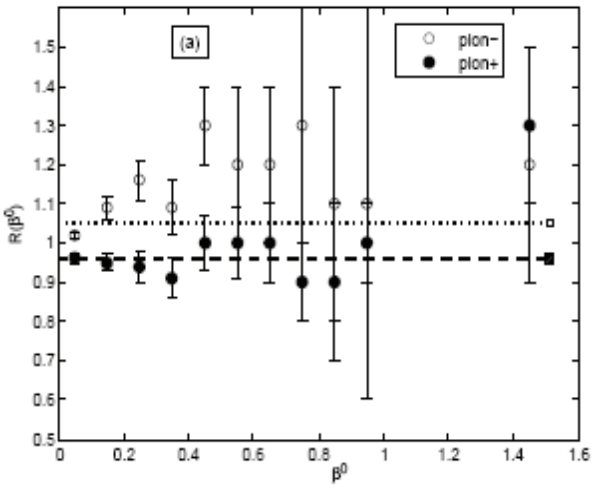

*Fig.2a.*The $R(\beta^0)$ dependence on β^0 for $\pi^{\pm}$ - mesons, emitted in $\pi^{-12}C$ -interactions at p_{π^-}=40GeV/c.

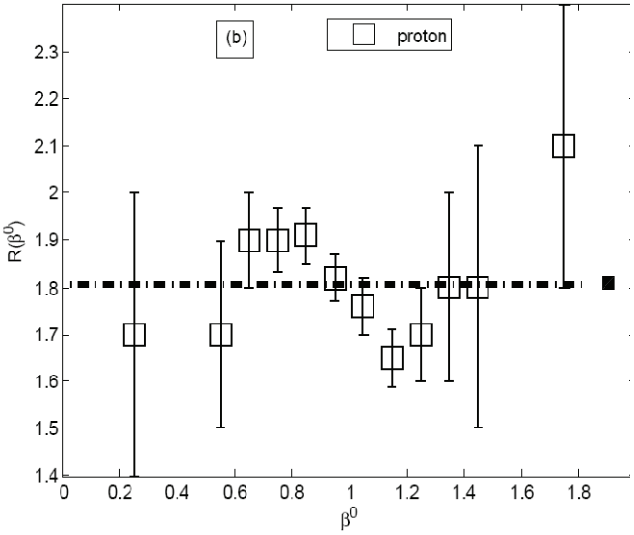

*Fig.2b.*The $R(\beta^0)$ dependence on β^0 for protons, emitted in $\pi^{-12}C$ - interactions at p_{π^-}=40GeV/c.

2.1) *for* π^+ *-mesons,* $R(\beta^0) \approx \overline{n_1'} / \overline{n_1}$ *at* $\beta^0<1$ *and* $R(\beta^0) \geq \overline{n_1'} / \overline{n_1}$ *at* $\beta^0>1$;

2.2) *for* π^- *-mesons,* $R(\beta^0) < \overline{n_1'} / \overline{n_1}$ *at* $\beta^0 <0.1$ *and* $R(\beta^0) \geq \overline{n_1'} / \overline{n_1}$ *at* $\beta^0> 0.1$;

2.3) *for protons,* $R(\beta^0) \geq \overline{n'} / \overline{n}$ *at* $\beta^0<1$ *and* $R(\beta^0) \leq \overline{n'} / \overline{n}$ *at* $\beta^0>1$.

The values of $R(T)$ are presented in fig.3, and it is seen that:

3.1) *for* π^+ *-mesons,* $R(T) \approx \overline{n_1'} / \overline{n_1}$;

3.2) *for* π^- *-mesons,* $R(T) > \overline{n_1'} / \overline{n_1}$ *at* $T <1GeV$ *and* $R(T) \leq \overline{n_1'} / \overline{n_1}$ *at* $T >1GeV$;

3.3) *for protons,* $R(T) \approx \overline{n'} / \overline{n}$.

4. DISCUSSION OF EXPERIMENTAL RESULTS

According to data given in the previous section, one can see that, the increase in the number of the nucleons participating in interaction, does not lead to any noticeable change in the distributions of secondary $\pi^{\pm}$ - mesons and protons on the p_t (results 1).

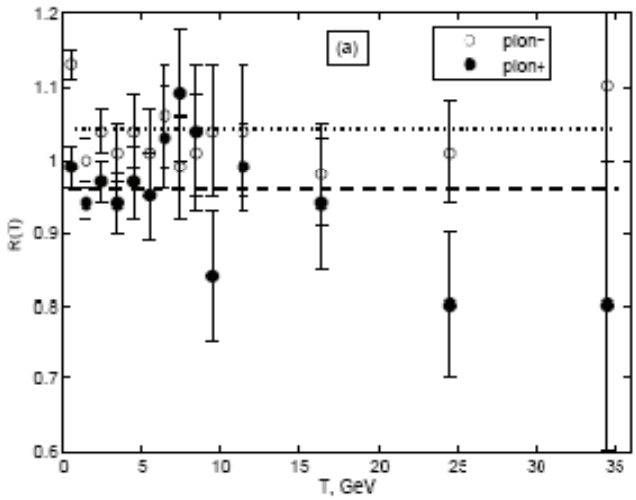

*Fig.3a.*The $R(T)$ dependence for $\pi^{\pm}$ - mesons (a), emitted in $\pi^{-12}C$ -interactions at p_{π^-}=40GeV/c.

This result may indicate that:

- the role of multiple collisions in multi-nucleon processes is negligible;
- in multi-nucleon processes in a significant part of cases nucleons inside the nucleus occupy less volume than the volume occupied by them in case of all processes.

In this case it is necessary to assume, that the interaction of the primary hadron occurs to a group of rigidly-correlated nucleons. This assumption in due time has been used by academician Baldin to explain the basic properties of a cumulative effect [15] and in searching the effect of nuclear shock waves in [16]. The author has also used assumption. However, the results 3.1 and 3.2 of the independence $R^{\pi^+,p}(p_t)$ from p_t are somewhat puzzled by the fact that in an area of radiation in case of rigid correlations of nucleons the "temperature" of the system should increase. First of all it should be reflected in a spectrum of protons by occurrence of high-temperature components. For elimination of the arising contradiction it is necessary to introduce a mechanism by which the system of rigidly-correlated nucleons "cools". For this purpose we turn the result 3.2, which indicates that in processes (2) the yield of π^- -mesons with momentum close to momentum of protons, more than in the processes (1).

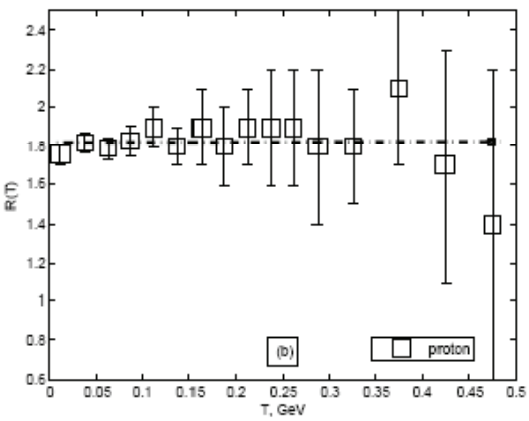

*Fig. 3b.*The $R(T)$ dependence for protons (b), emitted in $\pi^{-12}C$ - interactions at $p_{\pi^-} = 40GeV/c$.

Probably, this result is the reason of "cooling" of rigidly-correlated nucleons system through the mechanism of formation and decay of baryon resonances into proton and π^- -mesons. Confirming to this statement we should note that in paper [17] an attempt was made to determine the inclusive cross sections of a Δ baryon and N* nucleon resonances production in process (1) with allocation of process (2). Invariant mass spectra of pairs proton-π^- meson were analyzed. The author of that paper managed to obtain a relatively high yield of Δ in process (2). These data do not exclude an opportunity of occurrence in processes (2) in some cases a phase of resonances.

In multi-nucleon processes in the cumulative area (β^0>1) the yield of protons with momentum, greater than 1GeV/c (relativistic protons) is more, than in all events. Anoshin, etc. [18] has found, that the probability of a pion production with values β^0>0.6 is (2.0±0.2)% and of course the probability of proton emission with values β^0>0.6 in interactions in P_{π^-}= 40GeV/c is more, than this value, i.e. (37±1)% [19]. It explains why a point of regime change could not be observed on the behavior of R as function β^0 for pions. The results obtained in [10, 20] confirm the assumption which found that multi-nucleon events can be correctly identified using the following criterion: the number of protons greater than 3÷4 and the values β^0>0,6 for the pions produced in $\pi^{-12}C$ – interactions at P_{π^-} = 40GeV/c. It means that the area of new physics – multi-nucleon physics begins after values β^0>0.6.

For π^+-mesons $R^{\pi^+}(\beta^0) > \overline{n_1'}/\overline{n_1}$ at β^0>1 and that $R^{\pi^+}(\beta^0) < \overline{n_1'}/\overline{n_1}$ at β^0<1, i.e. excess π^+ - mesons in β^0>1 is related to the admixture of unidentified protons among π^+ -mesons. This fact, together with result 2.2 (at β^0<0,1) which indicates a weakening leading effect in multi-nucleon processes can be seen as an indication of the large contribution of inelastic processes in multi-nucleon events, i.e. manifestation of quark freedom degrees in nuclei in multi-nucleon processes. These results can have a great value for understanding of inter-nuclei processes at small distances when separate nucleons lose the individuality and the processes connected with quark degrees of nuclei are dominating, i.e. we can consider, that in some cases the group of rigidly - correlated nucleons with the big internal energy as a result of the further increase in temperature turns to a quark-gluon plasma which is cooled by emission of particles of greater spins, than at nucleons, including Δ and N*. Therefore, the properties of $\pi^\pm$ -mesons with T <1GeV should be investigated more carefully.

According to data, resulted on fig.4 it is seen, that in all range of definition of T, $R^{\pi^+}(T) \approx 1$ and $R^{\pi^-}(T) > 1$ at T<0,25GeV and $R^{\pi^-}(T) \approx 1$ at T ≥0,25GeV. Thus, we see, that the yield of π^- -mesons with T <0,25GeV in multi-nucleon processes is more, than in all $\pi^{-12}C$ – interactions at p_{π^-}=*40GeV/c*. This result probably serves as one more fact in favor of existence of a phase of baryon resonances in multi-nucleon systems. Let's explain told. It is known, that the probability of absorption of π^- - mesons with T<0,25GeV by group rigidly–correlated nucleons is greater and consequently, to explain the received result, it is necessary to assume, that these π^- - mesons emit out of area of absorption. One possible way of such emission could be the disintegration of slow baryon resonances.

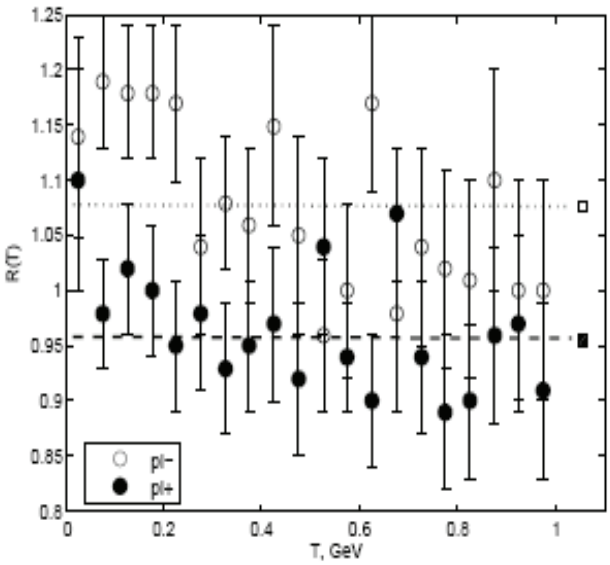

Fig.4. The $R(T)$ dependence for $\pi^\pm$ -mesons with kinetic energy T <1GeV (● -π^+ -meson, ○ -π^- -meson) emitted in $\pi^{-12}C$ - interactions at p_{π^-}= *40GeV/c.*

5. ANALYSIS OF ANGULAR DISTRIBUTIONS OF $\Pi^\pm$ -MESONS AND PROTONS

The results obtained in the previous sections show that multi-nucleon processes differ from all events in π^--mesons with kinetic energies T <0.25GeV. Large yield of soft π^-- mesons was explained due to the mechanism of neutral baryon resonances production with their subsequent decay into protons and π^- -mesons. Therefore, the angular distributions of $\pi^\pm$ - mesons and protons with T <0.25GeV in lab frame were analyzed in order to verify this assumption. For comparison, similar data for $\pi^\pm$ -mesons and protons with T >0.25GeV were obtained.

Fig.5 presents experimental data for $\pi^\pm$ -mesons and protons with T <0.25GeV.

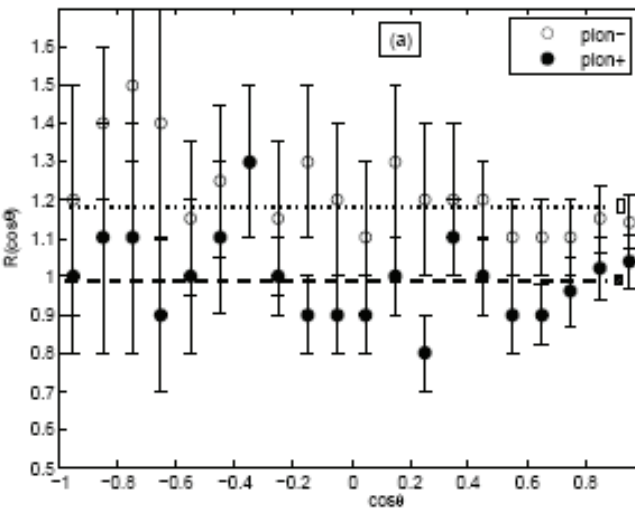

Fig.5a. $R(\cos\theta)$ dependence for $\pi^{\pm}$ -mesons (● -π^+, ○ -π^-) with T <0.25GeV, emitted in the $\pi^{-12}C$ - interactions at 40GeV/c.

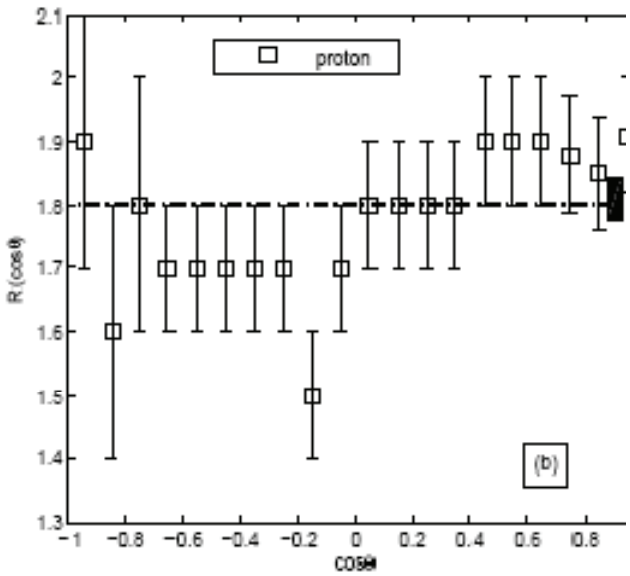

Fig.5b. $R(\cos\theta)$ dependence for protons(□) with T <0.25GeV, emitted in the $\pi^{-12}C$ - interactions at 40GeV/c.

One can see that:

1) *for π^+ -mesons, within the error bars $R^{\pi^+}(\cos\theta) \approx \overline{n_1'}/\overline{n_1}$ (0.99±0.02) in the whole studied range of θ, here θ, is the emission angle of π^+ -mesons ($\overline{n_1'}$ and $\overline{n_1}$ are the average multiplicities of secondary π^+ -mesons with kinetic energies T <0.25GeV in multi-nucleon and in all events, respectively);*

2) *for π^- -mesons, $R^{\pi^-}(\cos\theta)$ =1.4±0.1 in $\cos\theta$ <-0.6 (θ is an emission angle of π^- -meson), i.e. more than $\overline{n_2'}/\overline{n_2}$ =1.18±0.03;*

3) *for protons, within the error bars, $R(\cos\theta)$ coincides with the value $\overline{n'}/\overline{n}$ (1.81±0.03) in the whole studied range θ.*

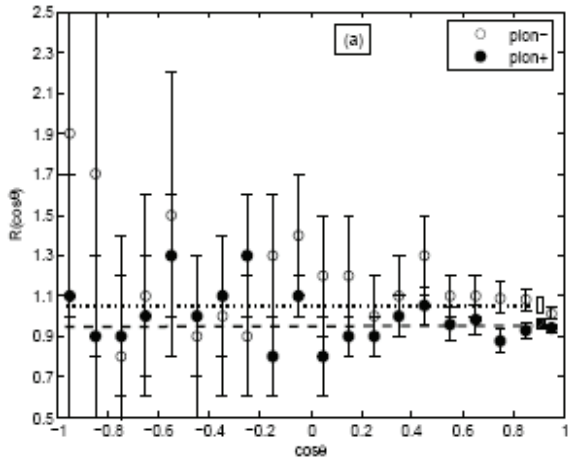

Fig.6a. $R(\cos\theta)$ dependence for mesons (● -π^+ -, ○ -π^- -) with kinetic energies 0,25<T<1GeV, emitted in $\pi^{-12}C$ - interactions at 40GeV/c.

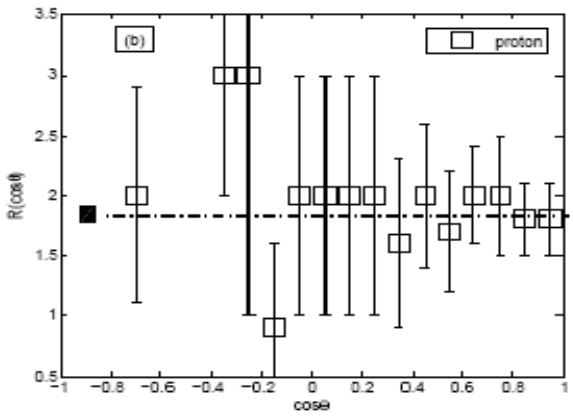

Fig.6b. $R(\cos\theta)$ dependence for protons (□) with kinetic energies 0,25<T<1GeV, emitted in the $\pi^{-12}C$ -interactions at P_π-=40GeV/c.

The data, presented in fig.6 and fig.7, shows that for charged pions and protons with 0.25< T <1GeV and for $\pi^{\pm}$-mesons with T >1GeV in the whole domain of definition of θ.

6. EFFECTIVE MASS DISTRIBUTION OF Π^- P PAIRS

Effective mass distribution of π^-p pairs emitted in multi-nucleon $\pi^{-12}C$ – interactions at the momentum of incident negative pions, which equal to 40GeV/c, is shown in Fig.8. Here, the restrictions mentioned above (T_π-<0,25GeV, $\beta^0(\pi^-)$>0.6, $\cos\theta(\pi^-)$ <-0.6) are taken into account. The experimental data was fitted by relativistic Breit-Wigner function type y=A*w*x*M/((x^2-M^2)^2 + w^2 * M^2). The fitted parameters are the following: Reduced Chi-Sqr=0.13877; Adj. R-Square=0.97423; width of the neutral baryon resonance with error, w=161.4818±9.71773; the mass of the neutral baryon resonance with error, M=1234.70704±2.53113 and

amplitude of the distribution with error, A=13050.58843±563.82774. The fitted parameters are in good consistence with other paper [9].

Thus, one could argue that the main difference between the selected multi-nucleon and all processes is the behavior of π^- -mesons with T <0.25GeV and $\cos\theta$ <-.6.

CONCLUSION

It is found that, multi-nucleon events can be correctly identified using the following criteria: the number of protons greater than 3÷4 and the values β^0>0,6 for pions produced in $\pi^{-12}C-$interactions with the P_π-=40GeV/c.

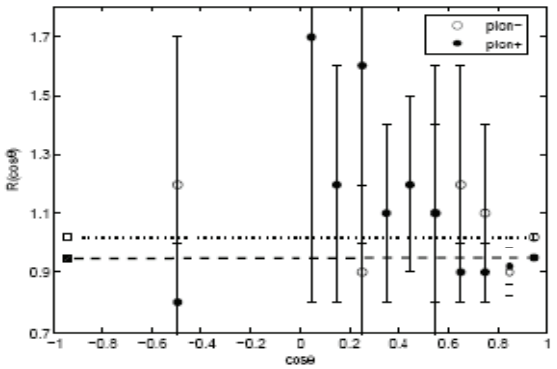

Fig.7. $R(\cos\theta)$ dependence for $\pi^\pm$ - mesons (● - π^+ -meson, ○ – π^- -meson) with kinetic energies T >0.25GeV, emitted in the $\pi^{-12}C-$interactions at P_π-=40GeV/c.

It turned out that multi-nucleon $\pi^{-12}C-$interaction (with the number of identified protons is greater or equal two), basically differ from all $\pi^{-12}C-$events by large yield of "soft" π^- -mesons with kinetic energies T<0.25GeV and emission angle $\cos\theta$ <-0.6 in the laboratory frame. This fact can be explained by the dominant role of the mechanism of neutral baryon resonance production in multi-nucleon processes with a relatively large cumulative number. It is found that the neutral Δ –baryon resonance can be extracted by using the particle characteristics, such as transverse momentum, cumulative number, kinetic energy and emission angle.

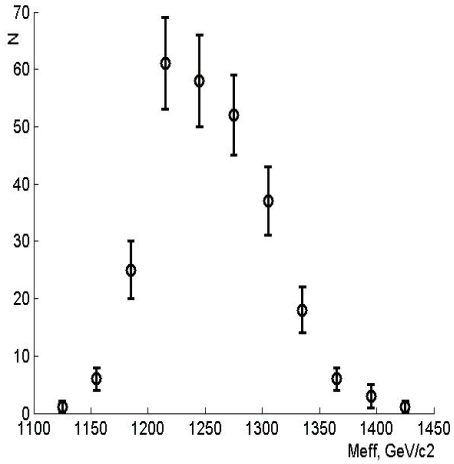

Fig.8. Effective mass distribution of π^-p pairs emitted in multi-nucleon $\pi^{-12}C-$interactions at P_π-=40GeV/c

[1] *E. Shuryak, I. Zahed,* hep-ph/0307267, 2003; *G.Brown, C. H. Lee, M. Rho, E. Shuryak*, hep-ph/0312175, 2003; hep- ph/0402068, 2004

[2] *F.Karsch et al.*,Nucl. Phys.Proc.Suppl., 2002,106,p. 513

[3] *M. Asakawa, T. Hatsuda*, hep-lat/0308034, 2003; *F. Karsch,* Nucl. Phys. B, 2003, 715, p.701.

[4] *J. Manjavidze, A. Sissakian,* Phys. Rep., 2001, 346, p. 1; *A.I.Sisakyan* Uspekhi Phisicheskih Nauk, 2003, 173, c. 328-332

[5] *R. Hagedorn*, Suppl. Nuovo Cimento 3 1965, 3, p. 147.

[6] *J. D. Bjorken*, Phys.Rev.1983,D27, p. 140.

[7] *P.K. Panda et al.,*nucl-th/0310075, 2003.

[8] *K. Saito, K. Tsushima, and A.W. Thomas,*Nucl. Phys. A, 1996, 609, p.339; Phys.Rev. C, 1997, 55, p. 2637; Phys. Lett. B, 1997, 406, p. 287.

[9] *Kh.K. Olimov,* Phys. Rev. C **76**, 055202 (2007).

[10] *A.I.Anoshin* et al.Yad.Fiz.36:409-416, 1982.

[11] *N. Angelov et al.*, Yad. Fiz. **33**, 1046 (1981).

[12] *U. Abdurakhimov* et al., Yad. Fiz. **18**, 545(1973),

[13] *U. Abdurakhimov et al.*, Some results on correlations in particle production in pion-proton interactions at 40GeV/c. Yad. Fiz. 18, 1251 (1973),

[14] *S.A. Azimov et al,* Multiplicity of secondary particles in inelastic proton-neon interactions at 300 GeV/c, Nucl.Phys. **B107**, 45 (1976).

[15] *A.M. Baldin* ECHAYA, v.8, issue 3, 1977, pp. 429-477.

[16] *A.I. Anoshin* et al. Yad.Fiz.33:164-168,1981.

[17] *A.I. Anoshin.* Preprint JINR, PI-83697, Dubna, 1980.

[18] *A.I. Anoshin* et al. Sov.J.Nucl.Phys. 31: 347,1980, Yad.Fiz.31:668-673,1980

[19] *N. Angelov* et al. Preprint JINR, P1-11951, Dubna, 1978.

[20] *O.B. Abdinov* et al. Journal of PEPAN Letters, JINR 1996,N1[75-96],p.51

Received: 01.02.2012

ANOMALIES OF THE INDUCED IMPURITY PHOTOCONDUCTIVITY IN GALLIUM MONOSELENIDE CRYSTALS

A.SH. ABDINOV, R.F. BABAYEVA*, YA.G. GASANOV **, S.I. AMIROVA, N.A. RAGIMOVA, R.M. RZAYEV

Baku State University,
Az 1145, Baku, Z.Khalilov str., 23

**Azerbaijan State Economic University,*
*** Azerbaijan Medical University*

Under various external conditions the basic characteristics and parameters of induced impurity photoconductivity (IIPC) in $p-GaSe$ crystals with various initial specific dark resistances have been investigated experimentally. It has appeared that in high-resistance crystals this photo-electric phenomenon is accompanied by a number of anomalies. It is ascertained that IIPC found out in high-resistance $p-GaSe$ crystals are caused with partial disorder of these crystals.

Keywords: impurity photoconductivity, trapping level, specific resistance, background illumination, drift barriers, recombination barriers, probing light.
PACS: 61.46

1. INTRODUCTION

Among $A^{III}B^{VI}$ semiconductor compounds with layered structure gallium monoselenide (GaSe) crystals gain special attention as a perspective material for optoelectronics, having high enough photosensitivity (at temperatures up to *~350 K*) and an optical transparency in *0.30÷0.63 μm* region and *0.65÷18 μm*, accordingly. Strong ionic-covalent binding in layers and considerably weak (Van-der-Vaals binding with the small ionic-covalent contribution) binding between layers (along the "C" axis of the crystal) besides strong anisotropy of electric, optical, thermal, mechanical properties of these crystals, causes also various anomalies of the non-equilibrium electronic phenomena in them. The layered structure does GaSe single crystals perspective also for creation various contact structures, photodetectors and light sources, as well as for bistable and threshold switches. The combination of switching property with high photosensitivity and highly effective injection electroluminescence in a visible region allows to create on the basis of these crystals various generators and relaxation oscillators for optoelectronics, including devices which are called vitrids and are competitors for multilayered (with one or several $p-n$ junctions) semiconductor devices, such as dinistors, thyristors, phototriggers, light sources with "S"-shaped current-voltage characteristic. Advantage of the last (vitrids) as compared to devices with $p-n$ junctions consist in possibilities to operate at any polarity of controlling external electric voltage and independence of switching voltage value on the steepness of operating impulse front .

In the scientific literature appeared information also about possibilities of creation on the basis of gallium monoselenide crystals sources of terahertz laser radiation applied in manufacture of photodetectors and photoconverters for infra-red (IR) radiation, control of photosensitivity range under the effect of various external influences and by means of change of intra-crystal conditions.

In our opinion, it is interesting also the fact that though in this material usual positive impurity photoconductivity is not observed almost, however take place other impurity photoeffects - negative photoconductivity, IR-quenching of intrinsic photoconductivity, induced impurity photoconductivity, induced by electric field negative photoconductivity [1, 2]. The specified properties, firstly considerably expand photosensitivity spectrum gallium monoselenide crystals towards near IR spectrum region (up to *~2.60 μm*); secondly allow to control their photoelectric properties purposefully; thirdly make these semiconductors a suitable material also for creation of various photodetectors and the converters representing a great interest for optoelectronics.

Though in some early works [3, 4] it was reported about detection in $p-GaSe$ crystals induced impurity photoconductivity (IIPC) of various type (IBIPC - induced by background illumination and IIIPC - induced by injection impurity photoconductivity), however herein the reasons of their anomalies remained not found out.

In particular it is established that unlike experimentally established in the majority of other semiconductor materials, as well as the contradiction of existing scientific notations on this phenomenon [5] in semiconductors, in general in $p-GaSe$ crystals experimentally measured value of IIPC itself (Δi_{ipc}) and the value of duration of the relaxation time (τ_{ipc}) after switching off the effect of probing light appear considerably high. In so doing specific dependences Δi_{ipc} values, as well their shapes, key parameters of its spectral distribution, light (lux-current) and current-voltage characteristics, kinetics on the value of exciting factors, injecting ability of current-carrying contacts, initial dark specific resistance (value of ρ_{do} at 77), alloying level for studied sample and temperature.

All above mentioned problems possess certain scientific-practical value and will demand detailed

experimental research of IIPC in $p-GaSe$ single crystals.

Naturally these researches besides enrichment of knowledge of electronic properties of gallium monoselenide crystals can be useful also for development of physics of the induced impurity photoconductivity in semiconductors in general.

In the given work set a goal on the basis of detailed experimental research of IIPC in $p-GaSe$ single crystals to find out the reasons of its anomalies in the specified material.

2. RESEARCH TECHNIQUE AND SAMPLES

Studied samples were cut off from various sections of the same pure (specially not alloyed) and alloyed by gadolinium atoms with various percentage ($N_{Gd}\approx 10^{-5}$; 10^{-4}; 10^{-3}; 10^{-2} and 10^{-1} at.%) of the single crystalline ingot (p-$GaSe$ and $p-GaSe<Gd>$) on cleavage planes. Both types' ingots were grown up by a method of slow cooling at a constant temperature gradient [6] and alloying with Gd of various composition was carried out by technology similar to applied elsewhere [7] for reception alloyed with rare-earth elements (REE) *n-InSe* crystals.

Samples represented plane-parallel plates of $d\approx 0.20\div 0.50\,mm$ thickness (along the "C" axis of the crystal) and $3\div 4.3\div 5\,mm^2$ area (on "C" plane of the crystal). Their specific dark resistance (ρ_d) was defined by standard two-probe method at *300 K* for various samples along and across the layers. At *300 K* ρ_d value were $\sim 10^1\div 10^6\ \Omega\cdot cm$ and $10^2\div 10^8\ \Omega\cdot cm$ for various samples, along and across the layers accordingly. With decreasing of temperature to *77 K* it sharply increased (almost by 3-4 order of magnitude) and for various samples were $\rho_d\approx 10^2\div 10^8\ \Omega\cdot cm$ and $\approx 10^3\div 10^{10}\ \Omega\cdot cm$ along and across the layers accordingly. As a material for current carrying contacts $In,\ Sn$, as well as silver paste or aquadag were used. Contacts were created by soldering In (or Sn) without a flux and application silver paste (or aquadag) in open air.

Depending on alloying level (N_{Gd} value) a value of ρ_{do} of $p-GaSe<Gd>$ crystals at *77K* varied within $10^2\div 10^{11}\ \Omega\cdot cm$.

Measurements were carried out on the experimental installation assembled on the basis of two monochromators (MDR-12 and MDR-12U type) with quartz lenses. As illumination sources incandescent lamps were applied intended specially for used monochromators.

Under all conditions considered by us illumination of investigated samples (both background illumination and a probing light beam) was carried out on "C" plane of the crystal. Measurements at research IBIPC were carried out both along and in perpendicular direction to layers, and at research IIIPC – in a direction parallel to "C" axis of the crystal.

At BCGA measurements the method of two light sources were used, in which one high-intensity beam of light with the fixed wavelength (with fixed energy of radiation quantum $h\nu_c$ as a rule corresponding to a maximum of a spectrum of intrinsic photoconductivity of the studied sample) and second – probing one with a wide radiation spectrum. Both radiation beams are received (selected) by means of used by us in experiment monochromators from incandescent lamps. From a probing radiation beam by means of MDR-12 narrow monochromatic beam with variable energy ($h\nu_V$) was selected.

Measurements were carried out in $77\le T\le 300\ K$, $U\le 3\cdot 10^3\ V/cm$, $\Phi\le 5\cdot 10^2\ Lux$ and $\mathbf{0.30}\le\lambda\le\mathbf{3.00}$ μm intervals of temperature (T), external electric voltage applied to the sample (U), intensity (Φ) and light wavelength (λ) accordingly.

At IIIPC measurements the first beam of light (the light beam with the fixed wavelength or quantum energy) was not used and unlike IBIPC case, instead of weak voltage, on the sample higher external voltage (corresponding to area of full filling of traps [8]) was applied. By change of value of this voltage injection level (level of IIIPC excitation in the studied sample) varied.

3. EXPERIMENTAL RESULTS

All basic IIPC characteristics (spectral distribution, light characteristics, kinetics, temperature dependence and dependence on the external electric voltage applied to the sample) were measured in studied samples (fig. 1-6).

Comparison of the received experimental results on spectral distribution, kinetics, light characteristics of IBIPC and IIIPC, as well as on influence ρ_{do} and T on these phenomena has shown that thereby qualitative differences are not observed. Only some quantitative differences take place. At that at IBIPC observable features under other identical conditions are shown more brightly. Therefore in given article we give only experimentally measured graphs on IBIPC, with the exception of the graph in which dependence of Δi_{ipc} on the value of the inducing external electric voltage (U_i) is represented.

As a result of the carried out measurements it is established that gallium monoselenide single crystals in IIPC properties at low temperatures ($T<300\,K$) also are divided on two groups: low-resistance and high-resistance ones.

In both groups of crystals at $T\le 170\div 190\,K$ (for various samples depending on value ρ_{do}) is observed pronounced IIPC which value and basic characteristics considerably depend also on ρ_{dO}. Under other identical conditions influence of specific dark resistance (ρ_{do}) on the above mentioned parameters and characteristics of IIPC with growth of ρ_{dO} manifests itself more strongly, and with rise in temperature is strongly weakened. With rise in temperature value of IIPC (Δi_{ipc} value) also decreases.

In low-resistance crystals parameters of IIPC spectrum (fig. 1, curve 1) appear independent of excitation level (intensity of background illumination and

voltage of injecting electric field at IBIPC and IIIPC accordingly).

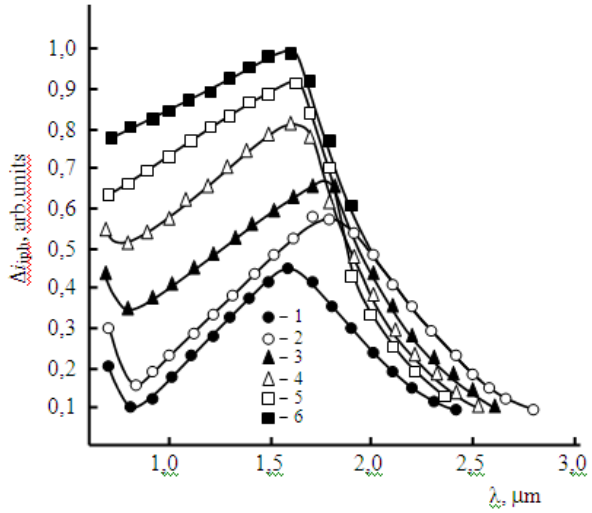

*Fig. 1.*IIPC spectrum in $p-GaSe$ crystals under various excitation levels. T=77 K; λ_c=0.58 μm; λ_I =1.60 μm; U = 5 V; ρ_{do}, Ω·cm: 1- 10^3; 2-6- 10^8; Φ_{int}, rel. units: 1, 2 - 0.1; 3 - 0.15; 4 - 0.25; 5 - 0.5; 6 - 0.8.

Thus both IBIPC and IIIPC spectrum covers $0.80 \le \lambda \le 2.80$ μm wavelength range and has a maximum at λ_{im}=1.60 μm. Besides in these (low-resistance) crystals IIPC has fast character. In particular, at switching on probing light stationary value Δi_{ipc} is established quickly and without inertia (almost instantly) falls down to zero after switching-off effect of probing light (fig. 2, curve 1).

Unlike low-resistance crystals, in high-resistance ones (fig. 1, curves 2-6) position of maximum (λ_{im}) and long-wavelength cut-off (λ_{ic}) on the spectral distribution of IIPC appear dependent on ρ_{do} and with growth of the last at weak Φ_I (as well as also at not so high U_i) are slightly displaced to longer waves (fig. 1, curves 2-4). With growth of excitation level (Φ or U_i values) and with rise of the temperature (at $T \le 100 \div 120 K$ for various samples depending on ρ_{do} value) dependences λ_{im} and λ_{ic} on ρ_{do} are gradually weakened and at last absolutely disappear.

In high-resistance crystals, unlike low-resistance ones, decay of IIPC after switching off effect of probing light has long-term relaxing character (fig. 2, curves 2-4) - residual IIPC is observed. Thus value of the residual IIPC ($\Delta i_{rc}=\Delta i_{ipc}-\Delta i'_{ipc}$, where $\Delta i_{ic}'$ - IIPC value through 30 sec after switching-off probing light) besides Φ_{imp} (fig. 2, curves 2-4) Φ_{int} (or U_i) appears dependent also on temperature and ρ_{do}. At low temperatures (fig. 3, curve 1) Δi_{rc} value decreases with increase of T (fig. 3, curve 1), and increases with growth of ρ_{do} (fig. 3, curve 2).

Both in low-resistance and high-resistance crystals light characteristic of IIPC (dependence $\Delta i_{пф}$ on Φ_i) has power-low character ($\Delta i_{ipc} \sim \Phi_i^{\alpha}$). And value of α, besides Φ_i appears dependent also on ρ_{do} (fig. 4, curve 1-5).

Dependence of value (Δi_{ipc}) induced by electric field impurity photoconductivity (IIIPC) on the external electric voltage applied to the sample (U_i) has non-monotonic character: at small U_i it increases and at higher values of U_i decreases with increasing voltage (fig. 5). However a steepness of $\Delta i_{пф}$ (U_i) curves and their inflection point appreciably depend on ρ_{do}.

For comparison on the same sample also spectral distribution of the negative photoconductivity, induced impurity photoconductivity and IR-quenching of intrinsic photoconductivity (fig. 6) were measured.

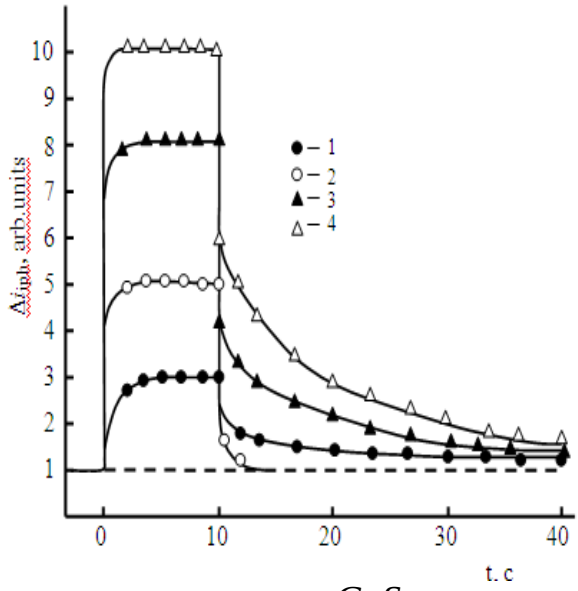

Fig. 2. IIPC kinetics in $p-GaSe$ crystals under various excitation levels (1, 2) and probing light intensity (1, 3, 4). T=77 K; λ_c=0.58 μm; λ_I = 1.60μm; $\rho_{do}=10^8$ Ω·cm; U=5 V; Φ_{int}, rel. units: 1, 3, 4 – 0.1; 2 - 0.8; Φ_{imp}, rel. units: 1, 2 – 0.2; 3 – 0.4; 4 – 0.8

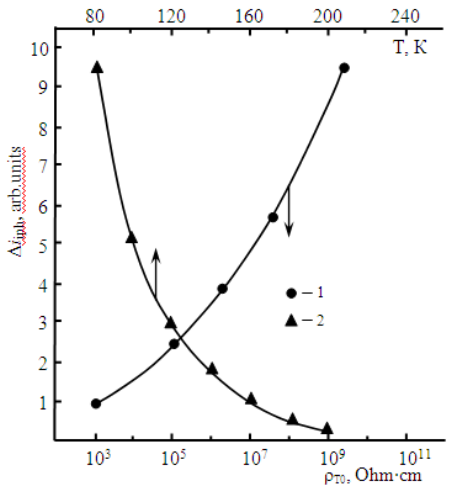

Fig. 3. Dependence of Δi_{ipc} value on initial specific dark resistance of the sample (curve 1) and temperature (curve 2) in $p-GaSe$ crystals. *T, K: 1 – 77;* Φ_{int} = 0.8 rel. units; Φ_{imp}=0.8 rel. units; λ_c=0.58 μm; λ_{imp}=1.60 μm; ρ_{do}, Ω·cm: 2 - 2·10^9

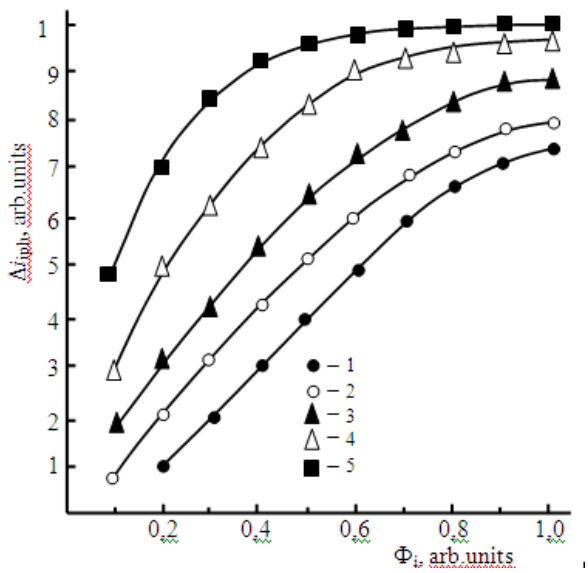

Fig. 4. Light dependence of IIPC in $p-GaSe$ crystals with various initial specific dark resistance (ρ_{do}). *T= 77 K; Φ_{int} = 0.8 rel. units; λ_c=0.58 μm; λ_{imp}=1.60 μm; U =5 V; ρ_{do}, Ω·cm*: 1-10^3; 2-10^8; 3 - $2\cdot10^6$; 4 - $5\cdot10^7$; 5 - $2\cdot10^9$

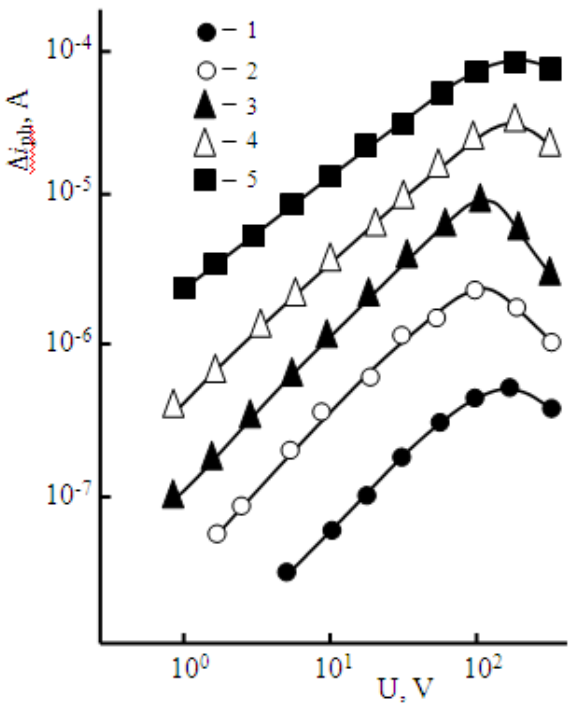

*Fig. 5.*Dependence of ИIIPC ($\Delta i_{пф}$) on external electric voltage (U_i) in $p-GaSe$ crystals. *T = 77 K: λ_{imp}=1.60 μm; Φ_{int}=0.8 rel.units; ρ_{do}, Ω·cm:* 1-10^3; 2-10^6; 3 - $5\cdot10^7$; 4 – 10^8; 5 - $2\cdot10^9$

4. DISCUSSION

The experimental measurements carried out by us show that from the point of view of existing scientific conceptions on IIPC in semiconductors [5], in high-resistance $p-GaSe$ crystals this photoelectric phenomenon exhibits a number of anomalies. In particular, unlike specified in [5] with which are well correlated received by us results for low-resistance - $p-GaSe$ crystals, in high-resistance crystals at low temperatures and low excitation levels a position of the maximum and long-wave limit of IIPC spectrum depend on excitation level and ρ_{do} value; kinetics of IIPC has slow relaxing character - it is observed residual IIPC, its value (Δi_{rc}) and relaxation time (τ_{rc}) which depend on excitation level of and ρ_{do}; in an initial part of light characteristic of IIPC the superlinear branch of dependence Δi_{ϕ} (Φ_n), which exponent depending on excitation level and ρ_{TO} changes within $2\div5$; dependence Δi_{ipc} (U_i) has non-monotonic character (Δi_{ipc} - at small U_i increases, and at higher U_i decreases with external voltage applied to the sample).

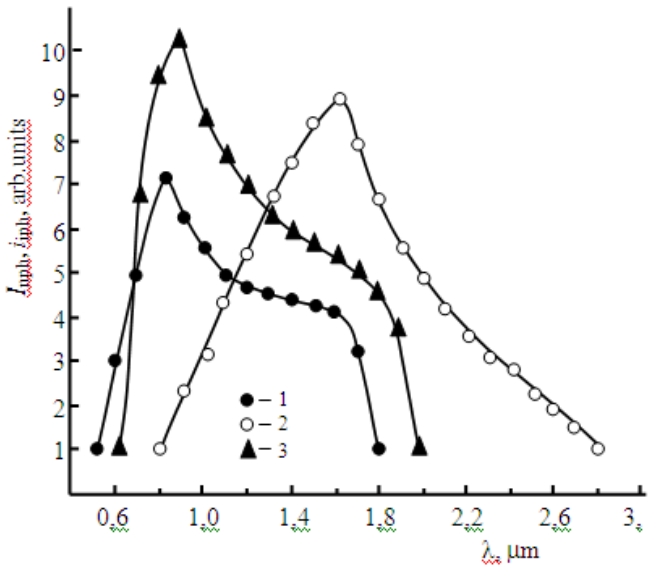

*Fig. 6.*Spectral distribution of negative photoconductivity (curve 1), induced impurity photoconductivity (curve 2) and IR-quenching of intrinsic photoconductivity (curve 3) in $p-GaSe$ crystals. *T=77 K; Φ_{int}=0.8* rel. units; *λ_{int}=0.58 μm; λ_{imp}=0.8 μm; ρ_{do} = $5\cdot10^7$ Ω·cm.*

The value of parameters characterizing all these anomalies with growth of alloying level of $p-GaSe$ crystal with Gd atoms also changes non-monotonically. In particular, with growth of alloying level (N_{Gd}) they at first (to $N_{Gd}\approx10^{-4}$ ат. %) increase and further decreasing at last, at $N_{Gd}\geq10^{-2}$ ат. %, almost absolutely disappear.

The comparative analysis of the received experimental results taking into account information existing in the scientific literature on electronic properties of $p-GaSe$ crystals and scientific concepts on IPF mechanism in semiconductors at all, allows to tell following about IPF mechanism in semiconductors.

As it is established elsewhere [1-4] in the forbidden band of $p-GaSe$ single crystals exist various recombination centers (slow and fast [9]), there are also trapping levels (capture levels with various depth energy - ε_t). At effect on these crystals external factors generating non-equilibrium charge carriers (light from fundamental absorption region or injecting external electric voltage) a part of the created non-equilibrium charge carriers at low temperatures (at $kT < \varepsilon_t$) are captured by these trapping levels. As a result of the last, non-equilibrium filled trapping levels become as though "active" impurity centers which can be emptying under the influence of stronger external energy field (for example, at switching effect [9]), and under action of impurity (probing) light with quantum energy $\varepsilon_t \le h\nu_{\mathrm{i}} < \varepsilon_{\mathrm{g}}$, where ε_g width of the forbidden band of the considered semiconductor material. In the latter case it is observed IIPC which value is defined by density *(N_t)* and degree of filling of trapping levels, and a spectrum – by their energy depth (ε_t). According to put forward elsewhere [5] fundamental conceptions on IIPC, herein its light characteristic (dependence $\Delta i_{n\phi}$ on Φ_i) should consist of an initial linear, subsequent sub-linear and finishing saturation part. According to these considerations herein duration of decay process of IIPC after switching off probing light should be defined by lifetime of the charge carriers released under the effect of probing light from trapping levels. In quasi-homogeneous semiconductors it usually equals to $\tau \le 10^{-6} s$, i.e. thus the long-term (or residual) relaxation of IIPC should not take place. As to dependence Δi_{ipc} (U_i), it should consist of an initial linear, subsequent sub-linear and final saturation branch. Actually, in low-resistance $p-GaSe$ crystals under all external conditions considered by us, excitation levels and temperatures these criteria are almost fulfilled. However in the low temperatures range at weak excitations, as has already been mentioned in the beginning of the present section, experimentally absolutely other situations are observed. The resume of the works done to date on electronic properties of high-resistance $p-GaSe$ crystals allows to tell that high-resistance $p-GaSe$ single crystals may be described satisfactorily on the basis of two-barrier energy model of partially-disorder semiconductor [10], according to which they as a whole consist of low-resistance matrixes (LRR), but with chaotic high-resistance inclusions (HRR). Besides, in the forbidden band of these crystals exist shallow *(α)* and deep *(β)* trapping levels, as well as fast *(S)* and slow *(r)* recombination centers [1-4]. And all these local levels are distributed on volume of the studied sample non-uniformly: α-levels and *S*-centers predominantly are localized in LRR, while β-levels and r-centers possess higher density in HRR. In LRR-HRR boundaries recombination barriers exist and in the allowed energy bands between adjacent HRR drift barriers exist. Under conditions considered by us IIPC is created mainly owing to excitation of quasi-equilibrium charge carriers captured by β-levels. Therefore it is not excluded also creation of IIPC owing to facilitated tunneling of charge carriers through recombination barriers. With growth of excitation level and with rise of the temperature light (or electric) and temperature smoothing of the potential relief occurs [11]. Therefore IIPC component facilitated by tunneling is weakened. Last in turn leads to displacement of the maximum and long-wave limit of spectrum for IIPC to shorter wavelengths with growth of excitation level and increasing of the temperature. Residual IIPC also is caused with presence of recombination barriers. Presence of drift barriers, in our opinion, connects sharper than linear dependence Δi_{ipc} *(Φ_n)* in an initial branch of light characteristic of IIPC, and also rather high value of Δi_{ipc}, than taking place in low-resistance crystals. Thus besides excess concentration of the photocarriers generated under the influence of probing light, in creation of IIPC the appreciable role plays also growth of the charge carriers mobility owing to deleting of drift barriers.

Within the limits of the offered model a falling part of Δi_{ipc} versus (U_i) curves can will be explained by a partial emptying β-levels owing to their tunnel breakdown at the voltage close to switching voltage [9] in this material.

Effect of the alloying with gadolinium atoms on characteristics of IIPC in $p-GaS$ crystals, most likely is caused by corresponding dependence of disorder degree of investigated samples on level of alloying with rare-earth element [12].

5. CONCLUSION

Thus, it is possible to conclude that the found out anomalies of induced impurity photoconductivity in high-resistance $p-GaSe$ crystals, first of all are caused by partial disorder of these crystals and predominantly localization bearing direct responsibility for creation in IIPC trapping levels in chaotic high-resistance inclusions existing in them.

[1] *A.Sh. Abdinov, A.G. Kyazym-zadeh.* The negative photoconductivity induced by electric field in gallium selenide single crystals. FTP, 1978, V.12, No. 6, P.1074-1078.

[2] *A.Sh. Abdinov, A.M. Guseynov.* Residual IR-quenching of intrinsic photoconductivity in indium and gallium selenide single crystals. Doklady AN Az. SSR., 1989, V.45, No. 4, P.11-16.

[3] *A.Sh. Abdinov, A.A. Ahmedov, V.K. Mamedov, El.Yu. Salayev.* Impurity photoconductivity in GaSe, induced by intrinsic illumination. FTP, 1980, V.14, No. 1, P.164-169.

[4] *I.M. Aliyev, N.A. Aliyeva, A.R. Gadzhiyev,* B.G. *Tagiyev.* Impurity photoconductivity induced by unipolar injection in $p-GaSe$. Izv. AN Az. SSR,

ser. fiz.-tekhn. i mat. nauk, 1980, No. 3, P.78-80.

[5] *S.M. Rivkin.* Photoelectric phenomena in semiconductors, M "Science", 1963, 494 p.

[6] *R.F. Mehtiyev, G.B. Abdullayev, G.A. Akhundov.* A method of growth of GaSe single crystals and research their some properties. Doklady AN Az. SSR, 1962, V.18, No. 6, P.11-17

[7] *A.M. Guseynov, T.I. Sadykhov.* Reception of indium selenide single crystals alloyed by rare-earth elements. In: Electrophysical properties of semiconductors and gas discharge plasma. Baku, ASU, 1989, P.42-44.

[8] *M. Lampert, P. Mark.* Injection currents in solids. M "Mir", 1973, 416 p.

[9] *A.Sh. Abdinov, R.F. Babayeva.* Effect of switching in layered $A^{III}B^{VI}$ monoselenides and heterostructures on their basis. The Bulletin of the Baku University, ser. fiz.-mat. nauk, 2009, №3, s.139-147.

[10] *M.K. Sheynkman, A.Ya. Shik.* Long-term relaxation and residual conductivity in semiconductors. FTP, 1976, V.10, No. 2, P.209-232.

[11] *V.I. Tagirov, A.G. Kyazym-zadeh, M.M. Panakhov.* Surface photo-e.m.f. in InSe and GaSe single crystals at high levels of excitation. Izv. Vuzov, Fizika, 1981, V. 24, No. 6, p. 28-31

[12] *R.F. Babayeva.* Features of the electronic phenomena in partially disorder $A^{III}B^{VI}$ type semiconductor crystals with layered structure alloyed by rare-earth elements and heterostructures on their basis. Abstract of Doctoral Thesis, Baku, 2009, 38 p.

Received: 25.01.2012

THE CALCULATION OF SPECTRAL CONSTANTS OF ISOBUTANOL MOLECULE ROTATIONAL ABSORPTION SPECTRUM

G.I. ISMAILZADEH, I.Z. MOVSUMOV, M.R. MENZELEYEV
H.M.Abdullayev Institute of Physics of Azerbaijan National Academy of Sciences
Az-1143, 33 H.Javid av., Baku

The semiempirical calculations of rotational constants of isobutyl alcohol $(CH_3)_2CHCH_2OH$ expected isomeric forms have been provided on the base of model with rigid molecular skeleton structure. The conformations structures have been analyzed equations and calculation results are presented.

Keywords: isobutanol, rotational absorption spectrum,
PACS: 31.10.+z

Methods of microwave (MW) gas spectroscopy allow us to have trustworthy information about structure of investigated substance at the molecular level. This information could be used as the basis for further macroscopic structures construction, study of the substance chemical and physical properties nature. Therefore, the investigations of molecular structure of such compounds class as alcohols and especially their monoatomic variety (alcanoles) by means of MW gas spectroscopy methods are possible to refer to the number of rather actual scientific problems. Particular interest here is attracted by the specificity of intramolecular motion dynamic, basically closed with presence of hydroxyl atomic groups, which are mainly responsible not only for the features of electrical properties of initial molecules, but also for the realization of intermolecular hydrogen bonds.

Isobutanol $(CH_3)_2CHCH_2OH$ molecule is certainly one of the most perspective objects from the point of potential information value. At the same time its molecular system structure features (sufficient length of molecular chain, presence of two methyl groups etc) are the cause of quite complex MW absorption spectra liable to fine structure effects of different nature and corresponding difficulties of identification of different isomeric forms spectra. Thereupon the provision of direct experiments has been anticipated by adequate design-theoretical researches - the initial and basic part of total investigation complex.

It has to be apparent that for the purpose of preliminary estimation of total number and relative stability of expected isomeric forms the first required step is to provide the calculations of the potential function of the asymmetric atomic groups' internal rotation. At this stage there isn't necessity to implement precision but same time complex (even for the comparison of simple molecules) ab-initio calculations, considering that the use of the MW gas spectroscopy methods in the further experimental researches will provide appropriate information about molecular structure. In other words the most reasonable way for preliminary evaluation of isobutyl alcohol potential function of internal rotation is the provision of the less laborious semi empiric calculations based on consideration of two types of intramolecular interactions [1]:

- Exchange interactions of electron clouds of the bonds adjacent to the internal rotation valence bond;
- Interactions of non-valence bonded atoms, which are realized in the process of asymmetric atomic groups of internal rotation (free interactions).

Besides that in the calculations for such class of molecular systems it is reasonable to take into consideration the ability of realization of electrostatic interactions experimentally founded and described in article [2] in the form of OH···C type hydrogen bonds.

Results of such semiempirical calculations model have showed availability of isobutanol in seven stable, energy-nonequivalent conformational conditions related to the mechanisms of simplex or duplex rotations of asymmetric atomic groups OH and CH_2OH around axes of internal rotation coincided with valence bond C_4-O (ψ) and C_3-C_4 (φ) directions respectively. It has been noted that realization of inversion T-g isomer with internal rotation angles $\varphi=0°$ and $\psi=\pm120°$ is not confirmed by such type of calculations. This possibly related with effect of steric repulsion of hydroxyl hydrogen atom by hydrogen atoms of two nearby located methyl groups. Together with this, results of more precision ab-initio calculations, given in article [3] suppose availability of that isomeric form, so it has been taken into account in further theoretical investigation process (fig.1, table 1).

The rotational constant values (A,B,C) of all mentioned above isobutanol molecule isomeric forms together with some other parameters of their structure have been obtained as the result of conventional calculations, based on postulation of investigated molecular system skeleton rigidity in the process of intramolecular rotation of its asymmetric segments (OH and CH_2OH). Taking into consideration this condition the universal equations for the determination of all atoms coordinates in adequate coordinate frames have been developed (table 2).

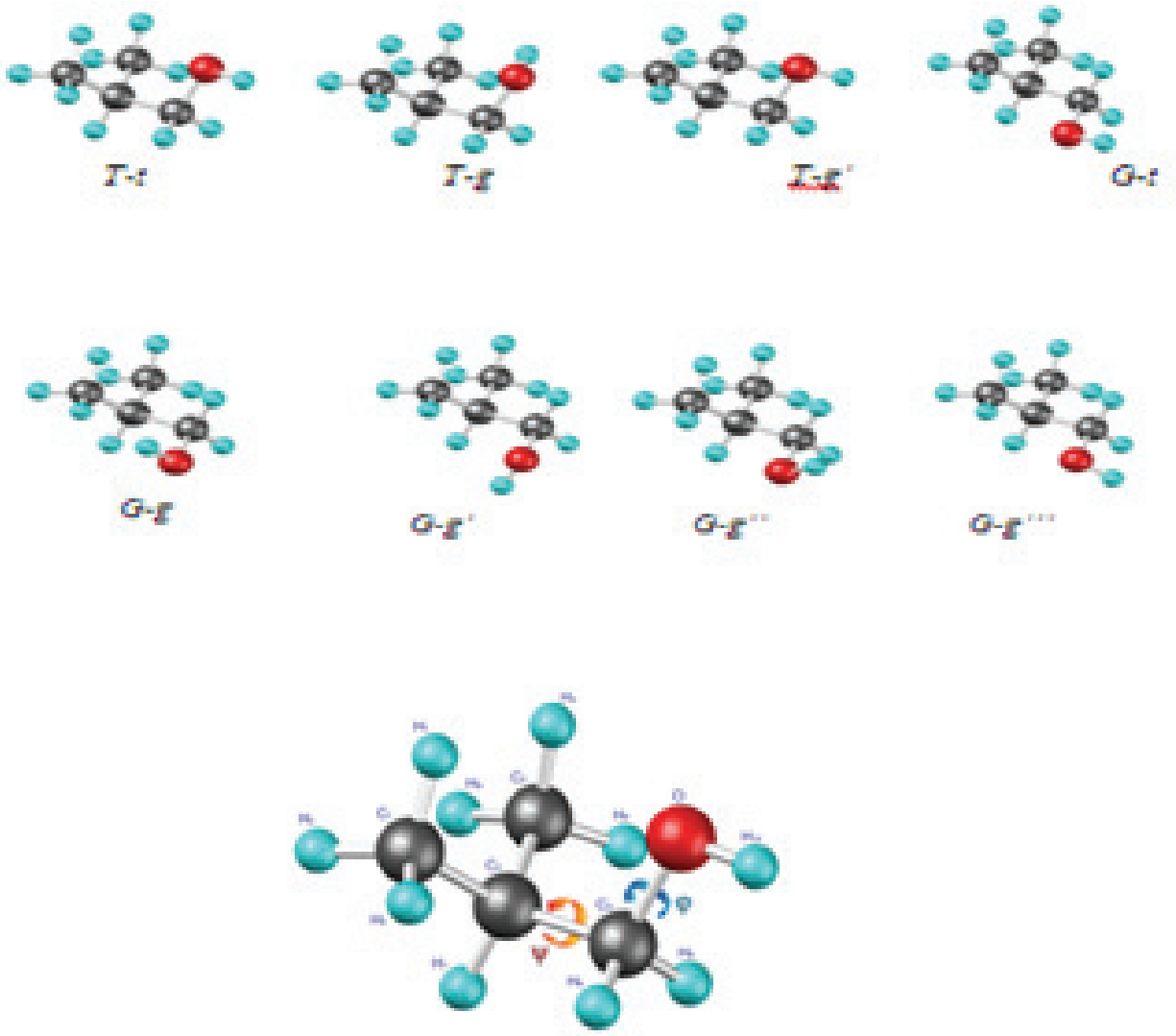

Fiq.1. Isobutanol molecule & its isomeric forms

Table 1.

Isobutyl alcohol $(CH_3)_2CHCH_2OH$ isomeric forms

№	Conformer	φ	ψ
1	T-t	0	0
2	T-g	0	±120°
3	T-g’	0	±30°
4	G-t	120°	0°
5	G-g	120°	120°
6	G-g’	120°	-120°
7	G-g’’	120°	30°
8	G-g’’’	120°	-30°

Table 2.

Universal equations for isobutyl alcohol molecule $(CH_3)_2CHCH_2OH$ atoms coordinates determination

C_1	X	$r_{(C-C)}\cdot\sin(\angle CCC)\cdot\cos\left(\psi+\arcsin\left(\frac{\sin(\angle CCC/2)}{\sin(\angle CCC)}\right)\right)$
	Y	$-r_{(C-C)}\cdot\cos(\angle CCC)$
	Z	$r_{(C-C)}\cdot\sin(\angle CCC)\cdot\sin\left(\psi+\arcsin\left(\frac{\sin(\angle CCC/2)}{\sin(\angle CCC)}\right)\right)$
C_2	X	$r_{(C-C)}\cdot\sin(\angle CCC)\cdot\cos\left(\psi-\arcsin\left(\frac{\sin(\angle CCC/2)}{\sin(\angle CCC)}\right)\right)$
	Y	$-r_{(C-C)}\cdot\cos(\angle CCC)$
	Z	$r_{(C-C)}\cdot\sin(\angle CCC)\cdot\sin\left(\psi-\arcsin\left(\frac{\sin(\angle CCC/2)}{\sin(\angle CCC)}\right)\right)$
C_3	X	0
	Y	0
	Z	0
C_4	X	0
	Y	$-r_{(C-C)}$
	Z	0
O	X	$r_{(C-O)}\cdot\sin(\angle CCO)$
	Y	$-r_{(C-C)}+r_{(C-O)}\cdot\cos(\angle CCO)$
	Z	0
H_1	X	$\sqrt{(X_{11})^2+(X_{12})^2}\times\cos\left(\psi+\arctan\left(\frac{X_{12}}{X_{11}}\right)\right)$, where $X_{11}=\sqrt{\left(r_{(C-C)}-r_{(C-H)}\cdot\cos(\angle CCH)\right)^2+\left(r_{(C-H)}\cdot\sin(\angle CCH)\right)^2}\times\cos\left(\arccos\left(\sqrt{\cos^2(\angle CCC/2)-\left(\sin^2(\angle CCC/2)-\cos^2(\angle CCC/2)\right)^2}\right)+\arctan\left(\frac{-r_{(C-H)}\cdot\sin(\angle CCH)}{r_{(C-C)}-r_{(C-H)}\cdot\cos(\angle CCH)}\right)\right)$ $X_{12}=\left(\sqrt{\left(r_{(C-C)}-r_{(C-H)}\cdot\cos(\angle CCH)\right)^2+\left(r_{(C-H)}\cdot\sin(\angle CCH)\right)^2}\times\sin\left(\arccos\left(\sqrt{\cos^2(\angle CCC/2)-\left(\sin^2(\angle CCC/2)-\cos^2(\angle CCC/2)\right)^2}\right)+\arctan\left(\frac{-r_{(C-H)}\cdot\sin(\angle CCH)}{r_{(C-C)}-r_{(C-H)}\cdot\cos(\angle CCH)}\right)\right)\right)\times\frac{\sin(\angle CCC/2)}{\sin\left(\arccos\left(\sqrt{\cos^2(\angle CCC/2)-\left(\sin^2(\angle CCC/2)-\cos^2(\angle CCC/2)\right)^2}\right)\right)}$
	Y	$\left(\sqrt{\left(r_{(C-C)}-r_{(C-H)}\cdot\cos(\angle CCH)\right)^2+\left(r_{(C-H)}\cdot\sin(\angle CCH)\right)^2}\times\sin\left(\arccos\left(\sqrt{\cos^2(\angle CCC/2)-\left(\sin^2(\angle CCC/2)-\cos^2(\angle CCC/2)\right)^2}\right)+\arctan\left(\frac{-r_{(C-H)}\cdot\sin(\angle CCH)}{r_{(C-C)}-r_{(C-H)}\cdot\cos(\angle CCH)}\right)\right)\right)\times\cos\left(\arcsin\left(\frac{\sin(\angle CCC/2)}{\sin\left(\arccos\left(\sqrt{\cos^2(\angle CCC/2)-\left(\sin^2(\angle CCC/2)-\cos^2(\angle CCC/2)\right)^2}\right)\right)}\right)\right)$
	Z	$\sqrt{(Z_{11})^2+(Z_{12})^2}\times\sin\left(\psi+\arctan\left(\frac{Z_{12}}{Z_{11}}\right)\right)$ where $Z_{11}=\sqrt{\left(r_{(C-C)}-r_{(C-H)}\cdot\cos(\angle CCH)\right)^2+\left(r_{(C-H)}\cdot\sin(\angle CCH)\right)^2}\times\sin\left(\arccos\left(\sqrt{\cos^2(\angle CCC/2)-\left(\sin^2(\angle CCC/2)-\cos^2(\angle CCC/2)\right)^2}\right)+\arctan\left(\frac{-r_{(C-H)}\cdot\sin(\angle CCH)}{r_{(C-C)}-r_{(C-H)}\cdot\cos(\angle CCH)}\right)\right)$ $Z_{12}=\left(\sqrt{\left(r_{(C-C)}-r_{(C-H)}\cdot\cos(\angle CCH)\right)^2+\left(r_{(C-H)}\cdot\sin(\angle CCH)\right)^2}\times\sin\left(\arccos\left(\sqrt{\cos^2(\angle CCC/2)-\left(\sin^2(\angle CCC/2)-\cos^2(\angle CCC/2)\right)^2}\right)+\arctan\left(\frac{-r_{(C-H)}\cdot\sin(\angle CCH)}{r_{(C-C)}-r_{(C-H)}\cdot\cos(\angle CCH)}\right)\right)\right)\times\frac{\sin(\angle CCC/2)}{\sin\left(\arccos\left(\sqrt{\cos^2(\angle CCC/2)-\left(\sin^2(\angle CCC/2)-\cos^2(\angle CCC/2)\right)^2}\right)\right)}$
H_2	X	$\sqrt{(X_{21})^2+(X_{22})^2}\cdot\cos\left(\psi+\arctan\left(\frac{X_{22}}{X_{21}}\right)\right)$ where

		$X_{21} = K \cdot \cos(\alpha + \beta)$ $X_{22} = \sqrt{(K \cdot \sin(\alpha+\beta))^2 + (r_{(C-H)} \cdot \sin(\angle HCH/2))^2} \cdot \sin\left(\arcsin\left(\frac{\sin(\angle CCC/2)}{\sin\alpha}\right) + \arctan\left(\frac{r_{(C-H)} \cdot \sin(\angle HCH/2)}{K \cdot \sin(\alpha+\beta)}\right)\right)$ $K = \sqrt{(r_{(C-C)} - r_{(C-H)} \cdot \cos(\angle CCH))^2 + (r_{(C-H)} \cdot \sqrt{\sin^2(\angle CCH) - \sin^2(\angle HCH/2)})^2}$ $\alpha = \arccos\left(\sqrt{\cos^2(\angle CCC/2) - (\sin^2(\angle CCC/2) - \cos^2(\angle CCC/2))^2}\right)$ $\beta = \arctan\left(\frac{r_{(C-H)} \cdot \sqrt{\sin^2(\angle CCH) - \sin^2(\angle HCH/2)}}{r_{(C-C)} - r_{(C-H)} \cdot \cos(\angle CCH)}\right)$
	Y	$\sqrt{(K \cdot \sin(\alpha+\beta))^2 + (r_{(C-H)} \cdot \sin(\angle HCH/2))^2} \cdot \cos\left(\arcsin\left(\frac{\sin(\angle CCC/2)}{\sin\alpha}\right) + \arctan\left(\frac{r_{(C-H)} \cdot \sin(\angle HCH/2)}{K \cdot \sin(\alpha+\beta)}\right)\right)$
	Z	$\sqrt{(Z_{21})^2 + (Z_{22})^2} \cdot \sin\left(\psi + \arctan\left(\frac{X_{22}}{X_{21}}\right)\right)$ where $Z_{21} = K \cdot \cos(\alpha + \beta)$ $Z_{22} = \sqrt{(K \cdot \sin(\alpha+\beta))^2 + (r_{(C-H)} \cdot \sin(\angle HCH/2))^2} \cdot \sin\left(\arcsin\left(\frac{\sin(\angle CCC/2)}{\sin\alpha}\right) + \arctan\left(\frac{r_{(C-H)} \cdot \sin(\angle HCH/2)}{K \cdot \sin(\alpha+\beta)}\right)\right)$
H_3	X	$\sqrt{(X_{31})^2 + (X_{32})^2} \cdot \cos\left(\psi + \arctan\left(\frac{X_{32}}{X_{31}}\right)\right)$ where $X_{31} = K \cdot \cos(\alpha + \beta)$ $X_{32} = \sqrt{(K \cdot \sin(\alpha+\beta))^2 + (-r_{(C-H)} \cdot \sin(\angle HCH/2))^2} \cdot \sin\left(\arcsin\left(\frac{\sin(\angle CCC/2)}{\sin\alpha}\right) + \arctan\left(\frac{-r_{(C-H)} \cdot \sin(\angle HCH/2)}{K \cdot \sin(\alpha+\beta)}\right)\right)$
	Y	$\sqrt{(K \cdot \sin(\alpha+\beta))^2 + (-r_{(C-H)} \cdot \sin(\angle HCH/2))^2} \cdot \cos\left(\arcsin\left(\frac{\sin(\angle CCC/2)}{\sin\alpha}\right) + \arctan\left(\frac{-r_{(C-H)} \cdot \sin(\angle HCH/2)}{K \cdot \sin(\alpha+\beta)}\right)\right)$
	Z	$\sqrt{(Z_{31})^2 + (Z_{32})^2} \cdot \sin\left(\psi + \arctan\left(\frac{Z_{32}}{Z_{31}}\right)\right)$ where $Z_{31} = K \cdot \cos(\alpha + \beta)$ $Z_{32} = \sqrt{(K \cdot \sin(\alpha+\beta))^2 + (-r_{(C-H)} \cdot \sin(\angle HCH/2))^2} \cdot \sin\left(\arcsin\left(\frac{\sin(\angle CCC/2)}{\sin\alpha}\right) + \arctan\left(\frac{-r_{(C-H)} \cdot \sin(\angle HCH/2)}{K \cdot \sin(\alpha+\beta)}\right)\right)$
H_4	X	$\sqrt{(X_{41})^2 + (X_{42})^2} \cdot \cos\left(\psi + \arctan\left(\frac{X_{42}}{X_{41}}\right)\right)$ where $X_{41} = \sqrt{(r_{(C-C)} - r_{(C-H)} \cdot \cos(\angle CCH))^2 + (r_{(C-H)} \cdot \sin(\angle CCH))^2} \times$ $\cos\left(\arccos\left(\sqrt{\cos^2(\angle CCC/2) - (\sin^2(\angle CCC/2) - \cos^2(\angle CCC/2))^2}\right) + \arctan\left(\frac{-r_{(C-H)} \cdot \sin(\angle CCH)}{r_{(C-C)} - r_{(C-H)} \cdot \cos(\angle CCH)}\right)\right)$ $X_{42} = \left(\begin{array}{l}\sqrt{(r_{(C-C)} - r_{(C-H)} \cdot \cos(\angle CCH))^2 + (r_{(C-H)} \cdot \sin(\angle CCH))^2} \times \\ \sin\left(\arccos\left(\sqrt{\cos^2(\angle CCC/2) - (\sin^2(\angle CCC/2) - \cos^2(\angle CCC/2))^2}\right) + \arctan\left(\frac{-r_{(C-H)} \cdot \sin(\angle CCH)}{r_{(C-C)} - r_{(C-H)} \cdot \cos(\angle CCH)}\right)\right)\end{array}\right) \times$ $\left(-\frac{\sin(\angle CCC/2)}{\sin\left(\arccos\left(\sqrt{\cos^2(\angle CCC/2) - (\sin^2(\angle CCC/2) - \cos^2(\angle CCC/2))^2}\right)\right)}\right)$

	Y	$\left(\sqrt{\left(r_{(C-C)}-r_{(C-H)}\cdot\cos(\angle CCH)\right)^2+\left(r_{(C-H)}\cdot\sin(\angle CCH)\right)^2}\times \sin\left(\arccos\left(\sqrt{\cos^2(\angle CCC/2)-\left(\sin^2(\angle CCC/2)-\cos^2(\angle CCC/2)\right)^2}\right)+\arctan\left(\frac{-r_{(C-H)}\cdot\sin(\angle CCH)}{r_{(C-C)}-r_{(C-H)}\cdot\cos(\angle CCH)}\right)\right)\right)\times \cos\left(\arcsin\left(\frac{\sin(\angle CCC/2)}{\sin\left(\arccos\left(\sqrt{\cos^2(\angle CCC/2)-\left(\sin^2(\angle CCC/2)-\cos^2(\angle CCC/2)\right)^2}\right)\right)}\right)\right)$
	Z	$\sqrt{(Z_{41})^2+(Z_{42})^2}\times\sin\left(\psi+\arctan\left(\frac{Z_{42}}{Z_{41}}\right)\right)$ where $Z_{41}=\sqrt{\left(r_{(C-C)}-r_{(C-H)}\cdot\cos(\angle CCH)\right)^2+\left(r_{(C-H)}\cdot\sin(\angle CCH)\right)^2}\times \sin\left(\arccos\left(\sqrt{\cos^2(\angle CCC/2)-\left(\sin^2(\angle CCC/2)-\cos^2(\angle CCC/2)\right)^2}\right)+\arctan\left(\frac{-r_{(C-H)}\cdot\sin(\angle CCH)}{r_{(C-C)}-r_{(C-H)}\cdot\cos(\angle CCH)}\right)\right)$ $Z_{42}=\left(\sqrt{\left(r_{(C-C)}-r_{(C-H)}\cdot\cos(\angle CCH)\right)^2+\left(r_{(C-H)}\cdot\sin(\angle CCH)\right)^2}\times \sin\left(\arccos\left(\sqrt{\cos^2(\angle CCC/2)-\left(\sin^2(\angle CCC/2)-\cos^2(\angle CCC/2)\right)^2}\right)+\arctan\left(\frac{-r_{(C-H)}\cdot\sin(\angle CCH)}{r_{(C-C)}-r_{(C-H)}\cdot\cos(\angle CCH)}\right)\right)\right)\times \left(-\frac{\sin(\angle CCC/2)}{\sin\left(\arccos\left(\sqrt{\cos^2(\angle CCC/2)-\left(\sin^2(\angle CCC/2)-\cos^2(\angle CCC/2)\right)^2}\right)\right)}\right)$
H_5	X	$\sqrt{(X_{51})^2+(X_{52})^2}\cdot\cos\left(\psi+\arctan\left(\frac{X_{52}}{X_{51}}\right)\right)$ where $X_{51}=K\cdot\cos(\alpha+\beta)$ $X_{52}=\sqrt{\left(K\cdot\sin(\alpha+\beta)\right)^2+\left(r_{(C-H)}\cdot\sin(\angle HCH/2)\right)^2}\cdot\sin\left(-\arcsin\left(\frac{\sin(\angle CCC/2)}{\sin\alpha}\right)+\arctan\left(\frac{r_{(C-H)}\cdot\sin(\angle HCH/2)}{K\cdot\sin(\alpha+\beta)}\right)\right)$
	Y	$\sqrt{\left(K\cdot\sin(\alpha+\beta)\right)^2+\left(r_{(C-H)}\cdot\sin(\angle HCH/2)\right)^2}\cdot\cos\left(\arcsin\left(\frac{\sin(\angle CCC/2)}{\sin\alpha}\right)+\arctan\left(\frac{r_{(C-H)}\cdot\sin(\angle HCH/2)}{K\cdot\sin(\alpha+\beta)}\right)\right)$
	Z	$\sqrt{(Z_{51})^2+(Z_{52})^2}\cdot\sin\left(\psi+\arctan\left(\frac{Z_{52}}{Z_{51}}\right)\right)$ $Z_{51}=K\cdot\cos(\alpha+\beta)$ $Z_{52}=\sqrt{\left(K\cdot\sin(\alpha+\beta)\right)^2+\left(r_{(C-H)}\cdot\sin(\angle HCH/2)\right)^2}\cdot\sin\left(-\arcsin\left(\frac{\sin(\angle CCC/2)}{\sin\alpha}\right)+\arctan\left(\frac{r_{(C-H)}\cdot\sin(\angle HCH/2)}{K\cdot\sin(\alpha+\beta)}\right)\right)$
H_6	X	$\sqrt{(X_{61})^2+(X_{62})^2}\cdot\cos\left(\psi+\arctan\left(\frac{X_{62}}{X_{61}}\right)\right)$ where $X_{61}=K\cdot\cos(\alpha+\beta)$ $X_{62}=\sqrt{\left(K\cdot\sin(\alpha+\beta)\right)^2+\left(-r_{(C-H)}\cdot\sin(\angle HCH/2)\right)^2}\cdot\sin\left(-\arcsin\left(\frac{\sin(\angle CCC/2)}{\sin\alpha}\right)+\arctan\left(\frac{-r_{(C-H)}\cdot\sin(\angle HCH/2)}{K\cdot\sin(\alpha+\beta)}\right)\right)$
	Y	$\sqrt{\left(K\cdot\sin(\alpha+\beta)\right)^2+\left(-r_{(C-H)}\cdot\sin(\angle HCH/2)\right)^2}\cdot\cos\left(\arcsin\left(\frac{\sin(\angle CCC/2)}{\sin\alpha}\right)+\arctan\left(\frac{-r_{(C-H)}\cdot\sin(\angle HCH/2)}{K\cdot\sin(\alpha+\beta)}\right)\right)$
	Z	$\sqrt{(Z_{61})^2+(Z_{62})^2}\cdot\sin\left(\psi+\arctan\left(\frac{Z_{62}}{Z_{61}}\right)\right)$ where $Z_{61}=K\cdot\cos(\alpha+\beta)$ $Z_{62}=\sqrt{\left(K\cdot\sin(\alpha+\beta)\right)^2+\left(-r_{(C-H)}\cdot\sin(\angle HCH/2)\right)^2}\cdot\sin\left(-\arcsin\left(\frac{\sin(\angle CCC/2)}{\sin\alpha}\right)+\arctan\left(\frac{-r_{(C-H)}\cdot\sin(\angle HCH/2)}{K\cdot\sin(\alpha+\beta)}\right)\right)$
H_7	X	$-r_{(C-H)}\cdot\sin(\angle CCH)\cdot\cos\psi$
	Y	$-r_{(C-H)}\cdot\cos(\angle CCH)$
	Z	$-r_{(C-H)}\cdot\sin(\angle CCH)\cdot\sin\psi$
H_8	X	$-r_{(C-H)}\cdot\sqrt{\sin^2(\angle CCH)-\sin^2(\angle HCH/2)}$
	Y	$-r_{(C-C)}+r_{(C-H)}\cdot\cos(\angle CCH)$

	Z	$r_{(C-H)} \cdot \sin(\angle HCH/2)$
H_9	X	$-r_{(C-H)} \cdot \sqrt{\sin^2(\angle CCH) - \sin^2(\angle HCH/2)}$
	Y	$-r_{(C-C)} + r_{(C-H)} \cdot \cos(\angle CCH)$
	Z	$-r_{(C-H)} \cdot \sin(\angle HCH/2)$
H_{10}	X	$r_{(C-O)} \cdot \sin(\angle CCO) - r_{(O-H)} \cdot [\cos(\angle COH) \cdot \sin(\angle CCO) - \sin(\angle COH) \cdot \cos(\angle CCO) \cdot \cos\varphi]$
	Y	$-r_{(C-C)} + r_{(C-O)} \cdot \cos(\angle CCO) - r_{(O-H)} \cdot [\cos(\angle COH) \cdot \cos(\angle CCO) + \sin(\angle COH) \cdot \sin(\angle CCO) \cdot \cos\varphi]$
	Z	$r_{(O-H)} \cdot \sin(\angle COH) \cdot \sin\varphi$

Table 3.

Rotational constants of isobutyl alcohol $(CH_3)_2CHCH_2OH$ molecule isomeric forms

№	Conformer	A	B	C	Δ	χ
1	T-t	6242.624620	3983.956018	3171.755311	48.48698812	-0.4710288
2	T-g	6127.823330	4107.103513	3254.305320	50.24241774	-0.40644312
3	T-g’	6225.011060	3998.807669	3178.201711	48.56812657	-0.46133423
4	G-t	7647.817790	3488.776538	2638.033515	19.37166809	-0.6603674
5	G-g	7560.573110	3540.231101	2685.685045	21.42847912	-0.64940895
6	G-g’	7600.749230	3577.008260	2681.487695	19.31224439	-0.6359126
7	G-g’’	7631.470217	3494.458987	2637.442032	19.23465968	-0.65678329
8	G-g’’’	7642.824724	3494.363588	2648.317504	19.92731945	-0.66120939

The values of structural parameters, i.e. noted here length of valence bonds and values of the valence angles for methyl groups have been taken from article [4] as for isopropyl alcohol molecule, for the last part of molecular skeleton – from articles [5, 6] as for n-propanol molecule. The values of rotational constants obtained by this way are presented in table 3.

This makes possible to calculate values of the frequencies of rotational transitions composing all supposed conformations MW absorption spectra. It has been noted, that the use of the simplified model with rigid skeleton without taking into account the influence of such intramolecular motion specific form as internal rotation of methyl groups, hydroxyl inversion relatively to the isobutanol molecular frame symmetry plane, of course, limiting availability of precise information regarding of the values of fine structure spectral characteristics frequencies related to specified conformation spectral lines A-E doubling or inversional splitting of T-g’ isomer spectra. Nevertheless with that presented in table 3 values of isobutanol molecule isomeric forms rotational constants are certainly interesting, first of all, from the point of their use as the start point in process of preliminary identification of microwave absorption spectra of isobutanol.

[1] *A.A. Abduraxma, E.I. Veliyulin.*«O povorotnom izomerizme molekuli n-butanola», Izvestiya AN Azerbaydjanskiy SSR, seriya Fiz-tex I mat.nauk №3, 1970, str.101-105.(in Russian).

[2] *A.A. Abduraxmanov, Q.I. Ismailzade.* Jurnal Strukturnoy Ximii 1987, t.2, №2, str.91-97.(in Russian).

[3] *Taigo Uzuyama, Yoshiyuki Kawashima, and Eizi Hirota* “Fourier transform microwave spectra of n-butanol and isobutanol” Kanagawa Institute of Technology the Graduate University for Advanced Studies, June 2009.

[4] *Ch.O., Qajar, S.A. Musayev, E.Yu. Salayev,* “Double RF-MW resonances in rotational spectra of molecules $(CD_3)_2CDOHX$ and (CH3)2CHOH. Journal of Applied Spectroscopy , July 1983, vol 39, p793.

[5] *A. Maeda, F.C.DeLucia, E.E.Herbst,* The millimeter and submillimeter spectrum of Gt conformer of n-propanol, The Astrophysical Journal Supplement Series, Feb.2006 No162.

Received: 02.02.2012

THE POLYMORPHOUS TRANSFORMATIONS IN $Cu_{1.50}Zn_{0.30}Te$ AND $Cu_{1.75}Cd_{0.05}Te$ CRYSTALS

U.I. ALIYEV, U.G. ASADOV, A.G. BABAYEV, K.M. JAFAROV, F.G. MAGERRAMOVA, R.D. ALIYEVA

H.M.Abdullayev Institute of Physics of Azerbaijan National Academy of Sciences
AZ-1143, G.Javid av., 33, Baku
e-mail: yusifasadov@rambler.ru

The existing polymorphous transformations in $Cu_{1.50}Zn_{0.30}Te$ and $Cu_{1.75}Cd_{0.05}Te$ crystals are registered by high-temperature X-ray method in temperature interval 290-1100K. The thermal expansion coefficients of each existing modification are calculated from temperature dependence of lattice parameters. The influence of partial substitution of Cu by Zn and Cd on phase formation, temperature and number of polymorphous transformations in $Cu_{1.50}Zn_{0.30}Te$ and $Cu_{1.75}Cd_{0.05}Te$ crystals is shown.

Keywords:crystal structure, phase transition, high temperature
PACS: 64.60-i

INTRODUCTION

The crystal structure of $Cu_{1.80}Te$ non-stoichiometric composition is defined in [1-5] and it is shown that $Cu_{1.80}Te$ has the hexagonal structure with lattice parameters $a=2a_0=8.37$Å, $c=3c_0=21.60$Å, Z=24, sp. gr. P3m1, density is $\rho_x=7.45$gr/cm^3 (here $a_0=4.246$Å, $c_0=7.289$ Å, Z=2, sp. gr. P6/mmm, density is $\rho_x=7.33$gr/sm^3, so called Novotnov phase Cu_2Te [6]) at room temperature.

At high temperature $Cu_{1.80}Te$, ZnTe and CdTe crystallize in HC structure with lattice parameters: $a=6.083$Å ($Cu_{1.80}Te$); $a=6.103$Å (ZnTe) and $a=6.477$Å (CdTe) [2, 8, 11].

The analogy of structures, elementary cells and cation ion radiuses (Cu^{1+}-0.98, Cu^{2+}-0.80, Zn^{2+}-0.83, Cd^{2+}-0.99) in $Cu_{1.80}Te$, ZnTe and CdTe gives the foundation that Cu atoms in $Cu_{1.80}Te$ can be isomorphically substituted by Zn and Cd and one can obtain the continuous series of mixed crystals.

The part of cuprum atoms are isomorphically substituted by Zn atoms and Cd in non-stoichiometric composition $Cu_{1.80}Te$, i.e. $Cu_{1.50}Zn_{0.30}Te$ and $Cu_{1.75}Cd_{0.05}Te$ with the aim of consider of their influence on $Cu_{1.80}Te$ structure, phase-formation, polymorphous transformation temperature. These problems are discussed on the given paper.

EXPERIMENTAL PART

$Cu_{1.50}Zn_{0.30}Te$ and $Cu_{1.75}Cd_{0.05}Te$ are synthesized separately and grown up by Bridgman method for solution of given tasks.

The samples are obtained from initial components (“electrolytic» cuprum, zinc and cadmium) in vacuum-processed up to 10^{-3}Pa quartz ampoule with inner diameter 1cm and length 10cm.

The ampoule is put in the furnace so that its part is in the furnace band at air melting point (725K) during 3h. Further, the furnace temperature is increased with velocity 50K/h up to 1450K, i.e. higher Cu_2Te melting point (1398K). The ampoule is cooled slowly up to 400K after two-hour enduring at this temperature with cyclic vibration and it is annealed at this temperature during 300 hours with the aim of homogenization. After this the furnace with ampoules is cooled up to room temperature.

The X-ray analysis is carried out for establishment of one-phase obtained samples. From synthesized samples of $Cu_{1.50}Zn_{0.30}Te$ and $Cu_{1.75}Cd_{0.05}Te$ the powdergrams, the interplanar spacing calculations:

a) The powdergram calculations obtained from $Cu_{1.50}Zn_{0.30}Te$ shows that the composition at room temperature is two-phase one and consists of orthorhombic modification with lattice parameters $a=7.319$Å$=c_0$, $b=22.236$Å$=3c_0$, $c=36.458$Å$=5c_0$ and hexagonal of modifications with lattice parameters $a=8.374$Å$=2a_0$, $c=21.598$Å$=3c_0$ (table1). As it is shown in [2], the orthorhombic phase with such parameters is the superstructure in the relation to hexagonal phase $a_0=4.248$Å, $c_0=7.234$Å.

b) The powdergram calculations obtained from $Cu_{1.50}Zn_{0.30}Te$ also proves its two-phase composition (table 2) which consists of orthorhombic and hexagonal modification.

The experimentally found combination of Bridgman method and slowly cooling is used for obtaining of $Cu_{1.50}Zn_{0.30}Te$ and $Cu_{1.75}Cd_{0.05}Te$ single crystals. The synthesized polycrystalline substances are put into ampoules (specially prepared for Bridgman method). The ampoules vacuum–processed up to pressure 10^{-3} Pa with corresponding compositions are put into furnace the temperature of which is regulated with the help of thermoregulator. Further, the temperature is slowly increased up to composition melting. After three-hour enduring the ampoule temperature decrease with velocity 2mm/h. In the third band of furnace having the constant temperature 350K, the samples in the ampoule are annealed during four weeks.

It is important to note that single crystals in laboratory conditions are usually grown up from the melt or gas phase. The crystal grown task is difficult if these compounds in solid states can exist in more than one crystal structure in the dependence on temperature. As a rule, the crystals of high-temperature modifications are grown up from melts and polymorphous substance steams. The crystals of the all rest modifications are obtained from only cooling as a result of polymorphous transformation and the crystals of low-temperature modifications stay at room temperature. The single crystal modifications of this

modification depend mainly on density difference of matrix and daughter crystal: a) if matrix crystal density weakly differs from new modification density, i.e. $\rho_I \geq \rho_{II}$ then transformation of single crystal – single crystal type takes place; b) if $\rho_I >> \rho_{II}$ or $\rho_I << \rho_{II}$ then transformation of single crystal – polycrystal type takes place. From such crystal it is impossible to obtain the single crystal by the method of polymorphous transformation.

Table 1. The powdergram calculation of $Cu_{1.50}Zn_{0.30}Te$ composition Radiation CuK_α (λ_α=1.5418Å), Ni is filter. Mode: 35 kV, 10 mA, exp.16 h.

$D_{exp.}$(Å)	I/I_0	Orthorhombic		Hexagonal		Elementary cell parameters
		D_{calc}(Å)	hkl	$D_{calc.}$(Å)	hkl	
7.252	60	-	-	7.253	100	Orthorhombic
5.827	41	5.796	122	-	-	
4.901	22	5.008	132	-	-	a=7.319 Å
4.331	30	-	-	4.331	104	b=22.236 Å
3.624	100	3.628	153,0.0.10	3.626	200	c=36.458 Å
3.371	100	3.370	155	-	-	Z=104
2.536	10	2.539	248	2.530	108	sp.gr. Pnma
2.407	20	2.404	312	2.402	301	ρ_x=7.095 gr/cm^3
2.148	10	2.151	308	-	-	
2.132	63	2.135	351	-	-	
2.067	31	2.065	338	-	-	
1.981	100	1.977	357	-	-	Hexagonal
1.824	92	1.824	382, 411	1.823	315	
1.543	14	1.544	468	1.542	319, 413	a=8.374 Å
1.519	21	1.517	477	1.518	414	c=21.598 Å
1.439	34	1.436	530	1.437	502, 0.0.15	Z=24
1.393	40	1.394	508	1.392	331	sp.gr. P3m1
1.377	30	1.377	509	1.375	505	ρ_x=7.347 gr/cm^3
1.334	21	1.334	4.10.9	-	-	
1.241	10	1.241	595	1.241	509	
1.170	11	1.171	653	1.172	3.3.10	
1.139	32	1.139	670	1.135	524	
1.074	13	1.077	696	1.079	609	
1.031	51	1.031	725	1.031	532	
0.964	11	0.965	779	0.967	538	
0.930	11	0.931	7.10.7	0.928	540	
0.878	24	0.878	872	0.878	548	
0.856	32	0.856	893	0.854	639	
0.815	39	0.813	900	0.815	731	
0.794	41	0.794	962	0.795	468	

The investigations at high temperatures are carried out on diffractometer ДРОН-3М (CuK_α is radiation, Ni is filter) with high-temperature installation УРВТ-2000 in vacuum (10^{-2} Pa).

The angular resolution is ~0,1°. The regime of continuous scanning is used. In experiments the angle definition error doesn't exist $\Delta\theta=\pm0{,}02°$.

$Cu_{1.50}Zn_{0.30}Te$. At room temperature (293K) the fixed 9 diffraction reflections in angle interval $10° \leq 2\theta \leq 100°$ are indicated on the base of orthorhombic lattice parameters a=7.319Å≃c_0, b=22.236Å≃3c_0, c=36.458Å≃5c_0 and hexagonal modification with lattice parameters a=8.374 Å≃2a_0, c=21.598 Å≃3c_0, i.e. $Cu_{1.50}Zn_{0.30}Te \rightarrow (CuZn)_{1.80}Te$ two-phase crystals (see table3). As it is mentioned in [2,6] the orthorhombic modification is the hexagonal modification superstructure.

After diffractogram record at room temperature the furnace is switch on and the control records are made through each 100K. The sample temperature before each record is supported during 40 minutes.

At these conditions up to 473K the reflection number and their intensity fixed at room temperature stay constant. At temperature increase higher 473K the diffraction picture changes (table 3), i.e. the new diffraction reflections appear. Besides reflections (025) and (199), the rest ones can consider as components of split earlier existed diffraction reflections. The reflections from (113), (117) and (411) planes of hexagonal lattice correspondingly are also overlapped on (210), (257) and (458) reflections of orthorhombic one.

The diffraction reflections appearing at 473K because of splitting disappear at 573K and in previous angle interval 7 reflections are fixed. At 673K the repeated splitting of some reflections belonging to both orthorhombic and hexagonal modifications. At 773K besides reflections from orthorhombic and hexagonal modifications the four reflections from (111), (200), (220) and (311) belonging to lattice of high-temperature HCC modification with parameter a=6,120Å. The annealing at this temperature or heating continuation leads to total transformation of orthorhombic and hexagonal modification into HCC modification.

The calculation results of lattice parameters on diffractogram are graphically shown on fig.1 where a(T), b(T), c(T), V(T) and ρ(T) орторомбической, a(T), c(T), V(T) and ρ(T) hexagonal and a(T), V(T) and ρ(T) ГЦК modifications.

Table 2. The powdergram calculation of $Cu_{1.75}Cd_{0.05}Te$ composition, Radiation CuK_α (λ_α=1.5418Å), Ni is filter. Mode: 35 kV, 10 mA, exp.16 h.

$D_{exp.}$(Å)	I/I_0	Orthorhombic		Hexagonal		Elementary cell parameters
		$D_{calc.}$(Å)	hkl	$D_{calc.}$(Å)	hkl	
7.049	35	7.049	024	-	-	Orthorhombic
3.957	60	3.954	136	-	-	
3.708	30	3.708	060	3.711	405	a=7.380 Å
3.581	100	3.578	146	3.574	201	b=22.250 Å
3.222	40	3.222	156	3.221	106	c=36.274 Å
2.627	30	2.627	176	-	-	Z=104
2.537	30	2.539	248	2.534	108	sp.gr. Pnma
2.453	20	2.452	087	-	-	ρ_x=7.130 gr/cm^3
2.394	60	2.394	271	2.397	009, 301	
2.281	50	2.279	275	2.282	109	
2.265	10	2.265	306	2.267	118	
2.081	60	2.081	319	2.082	119	Hexagonal
1.999	25	1.998	0.10.8	2.001	209	
1.945	20	1.942	289	1.946	224	a=8.370 Å
1.833	10	1.856	380, 400	1.856	2.0.10	c=21.573 Å
1.802	60	1.803	421	1.805	219	Z=24
1.798	26	1.798	414	1.798	308, 0.0.12	sp.gr. P3m1
1.587	70	1.587	3.10.6	1.589	324	ρ_x=7. 437 gr/cm^3
1.442	80	1.442	514	1.441	501	
1.438	100	-	-	1.438	502, 0.0.15	
1.339	20	1.338	565	1.341	506	

As it is seen from fig.1 a parameter of orthorhombic, a and c parameters of hexagonal and a parameter of HCC modification in the dependence on temperature increase linearly, but b parrameter of orthorhombic modification linearly increases up to 470K, further decreases and beginning from 570K linearly increases up to transformation temperature. The c parameter linearly decreases up to 470K and at 570K increases beginning from 570K up to transformation temperature linearly decreases. This is explained by redistribution of cautions and vacancies.

The thermal expansion coefficients (TEC) both orthorhombic, hexagonal and HCC modifications which are given in table 4, are calculated from temperature dependence of lattice parameters. As it is seen from the table, at all temperatures TEC along [001] $\alpha_{[001]}$ direction of orthorhombic modification is negative one , i.e. $\alpha_{[001]}<0$.

Table 3

Rentgenographic data for $Cu_{1.50}Zn_{0.30}Te$, Radiation CuK_α (λ_α=1.5418Å), Ni is filter, mode 35 kV, 8 mA, exp. 24 h.

T_{exp} K	θ	I/I_0	$D_{exp.}$(Å)	Hexagonal		Orthorhombic		Elementary cell parameters
				D_{calc}(Å)	hkl	D_{calc}(Å)	hkl	
293	6°06′	60	7.252	7.2528	100	-	-	Hexagonal, a=8.374Å, c=21.598Å
	10°15′	45	4.331	4.331	104	-	-	sp.gr.P3m1, Z=24, ρ_x=7.347 gr/cm^3
	12°17′	100	3.624	3.6262	200	3.6275	153,0010	
	13°13′	100	3.371	-	-	3.3703	155	Orthorhombic, a=7.290Å,
	18°41′	60	2.407	2.4024	301	2.4039	312	b=22.325Å
	21°02′	10	2.148	-	-	1.1508	308	c=36.244Å, sp.gr. Pnma
	25°02′	40	1.820	1.8234	315	1.8196	401	Z=104, ρ_x=7.095 gr/cm^3
	29°58′	50	1.543	1.5415	319,4 13	1.5437	468	
	34°02′	30	1.377	1.3750	505	1.3767	509	
473	6°04′	70	7.293	7.2899	100	-	-	Hexagonal, a=8.421Å
	7°15′	10	6.109	-	-	6.0982	025	c=21.642Å
	10°13′	45	4.346	4.3454	104	-	-	sp.gr. P3m1
	10°19′	30	4.304	-	-	4.3045	142	Z=24
	12°13′	100	3.647	3.6449	200	3.6466	153,0010	ρ_x=7.251 gr/cm^3
	12°18′	100	3.619	-	-	3.6178	210	
	13°10′	70	3.384	-	-	3.3822	057	Orthorhombic, a=7.333Å
	13°14′	30	3.366	-	-	3.3718	155	b=22.233Å
	18°06′	40	2.481	2.4824	117	2.4861	257	c=36.244Å
	18°38′	30	2.412	2.4148	301	-	-	sp.gr. Pnma
	21°00′	40	2.151	-	-	2.1522	308	Z=104
	22°21′	20	2.027	-	-	2.0271	199	ρ_x=7.039 gr/cm^3
	24°56′	15	1.829	1.8324	315	1.8248	401	
	29°10′	15	1.582	1.5865	411	1.5887	458	
	24°51′	20	1.549	1.5477	319, 413	1.5458	468	
	33°39′	50	1.379	1.3817	505	1.3791	509	

573	6°04′ 10°13′ 12°18′ 13°10′ 18°06′ 22°21′ 24°56′	40 50 100 100 60 30 5	7.335 4.346 3.668 3.389 2.488 2.039 1.832	7.3245 4.3454 3.6622 - 2.4920 - 1.8370	100 104 200 - 117 - 315	- - 3.6675 3.3886 - 2.0295 1.8324	- - 0.0.10 057 - 119 401	Hexagonal, a=8.471Å, c=21.567Å sp.gr.P3m1, Z=24, ρ_x=7.190 gr/cm^3 Orthorhombic, a=7.362Å, b=22.704Å c=35.333Å, sp.gr. Pnma Z=104, ρ_x=7.087 gr/cm^3
673	6°02′ 10°12′ 12°05′ 12°09′ 13°07′ 17°44′ 18°01′ 18°41′ 19°16′ 24°49′	40 20 100 40 100 20 20 20 30 40	7.335 4.353 3.683 3.662 3.396 2.531 2.492 2.471 2.336 1.836	7.3343 4.3528 3.6674 3.6517 - - 2.4963 - - 1.8410	100 104 200 113 - - 117 - - 315	- - 3.6674 - 3.3966 2.5321 - 2.4708 2.3383 -	- - 153, 0010 - 057 086 - 090 191 -	Hexagonal, a=8.506Å, c=21.585Å sp.gr. P3m1, Z=24 ρ_x=7.125 gr/cm^3 Orthorhombic, a=7.699Å, b=22.473Å c=35.007Å, Z=104 sp.gr. Pnma ρ_x=6.910 gr/cm^3
773	10°10′ 12°35′ 13°05′ 14°35′ 17°43′ 17°59′ 19°15′ 20°52′ 24°41′	30 30 100 40 30 30 50 50 40	4.368 3.534 3.405 3.062 2.533 2.497 2.338 2.164 1.841	4.3677 3.5337 - 3.0602 2.5334 2.5046 - 2.1639 1.8453	104 (111)* - (200)* 108 117 - (220)* 315 (311)*	- - 3.4050 - 2.5337 - 2.3382 - 1.8429	- - 057 - 086 - 191 - 401	Hexagonal, a=8.616Å, c=21.547Å sp.gr. P3m1, Z=24 ρ_x=6.956 gr/cm^3 Orthorhombic, a=7.423Å, b=22.222Å c=37.088Å, Z=104 Pnma, ρ_x=6.910gr/cm^3 HCC: a=6.120Å
973	12°34′ 14°33′ 20°49′ 24°37′	100 40 60 80	3.544 3.070 2.170 2.851	3.5442 3.0693 2.0703 1.8509	111 200 220 311			Z=4, пр.гр.Fm3m ρ_x=7.005 gr/cm^3 HCC: a=6.139Å, Z=4 Fm3m, ρ_x=6.943gr/cm^3
*- (111), (200), (220) and (311) belong to HCC modification								

Table 4. Thermal expansion of $Cu_{1.50}Zn_{0.30}Te$ (*10^{-6}grad^{-1}) modification.

Modification	T_{exp}, K	$\alpha_{[100]}$	$\alpha_{[010]}$	$\alpha_{[001]}$	$\bar{\alpha} = \frac{\alpha_{[100]} + \alpha_{[010]} + \alpha_{[001]}}{3}$	$\bar{\beta} = \alpha_{[100]} + \alpha_{[010]} + \alpha_{[001]}$
Orthorhombic	293-373 373-473 473-573 573-673 673-773	70.302 2.728 39.547 52.975 29.726	121.485 120.761 -26.858 40.175 5.567	-353.734 -206.976 136.806 -40.573 -26.876	-53.982 -27.829 49.832 17.526 2.806	-65,33 -72,32 4,88 18,01 25,78
Hexagonal	293-373 373-473 473-573 573-673 673-773	32.855 26.215 30.901 3.555 21.319		2.316 1.389 16.667 1.387 0.924	22.675 17.940 26.156 2.832 14.521	67,27 59,22 66,30 51,04 49,98
HCC	773-873 873-973 973-1073	16.340 14.682 14.660			16.340 14.682 14.660	49.020 44.046 43.980

$Cu_{1.75}Cd_{0.05}Te$. At room temperature in angle interval $10^\circ \le 2\theta \le 80^\circ$ ten diffraction reflections from $Cu_{1.75}Cd_{0.05}Te$ crystal which as powdergrams (table 2) are indicated on the base of elementary cell parameters of orthorhombic and hexagonal modifications identically to $Cu_{1.75}Cd_{0.05}Te$ crystal (table 5), are fixed. Note that some reflections especially most intensive ones indicate on the base of elementary sell parameters of $Cu_{1.80}Te$ hexagonal modification, i.e. the reflections from (009), (0.0.12) and (0.0.15) planes of hexagonal lattice overlap on reflections from (094), (414) and (530) planes of orthorhombic one. The diffraction picture fixed at room temperature stays constant up to 573K. At 573K the splitting of three most intensive reflections (009), (0012) and (0015) and at 673K the splitting totally ends. Moreover, the insensitivities of (414) orthorhombic and (0012) hexagonal modifications become less ones than reflection intensivities from (413) plane of orthorhombic and new (004) modifications which appear at splitting. The diffraction reflections from (003), (004) and (005) planes appearing as a result of reflection splitting from (009), (0012) and (0015) planes belong to new hexagonal modification with lattice parameters *a*=4.20Å, *c*=7.26Å close to parameter values of Novotnov hexagonal phase for stoichiometric composition Cu_2Te. At 761±1 K both splitted reflections and ones belonging to first hexagonal modification disappear. In previous angle

interval only five reflections belonging to orthorhombic modification are fixed and reflections from (311) and (222) planes belonging to high-temperature HCC modification overlap on (289) and (3010) reflections. At 833±2 K all reflections from orthorhombic modification totally disappear and in previous angle interval only reflections from (311) и (222) planes of cubic modification with lattice parameter a=6.727Å stay.

Table 5.

The diffractogram calculation of $Cu_{1.75}Cd_{0.05}Te$ crystal at different temperatures Radiation CuK_α (λ_α=1.5418Å), Ni is filter, mode 35 kV, 10 mA.

T_{exp}, K	D_{exp}(Å)	I/I_0	Orthorhombic		Hexagonal		Elementary cell parameters
			D_{calc}(Å)	hkl	D_{calc}(Å)	hkl	
290	2.627	30	2.627	176	-	-	Orthorhombic, a=7.330Å, b=22.250Å
	2.453	20	2.452	087	-	-	c=36.274Å, sp.gr. Pnma
	2.397	50	2.395	094	2.397	009	Z=104, ρ_x=7.130 gr/cm^3
	2.265	10	2.265	306	2.267	118	
	2.081	20	2.081	319	2.080	119	Hexagonal-I,
	1.994	30	1.994	3.2.10	2.000	209	a=8.370Å
	1.833	10	1.856	380,400	1.855	2.0.10	c=21.573Å
	1.798	30	1.797	414	1.798	0.0.12,402	sp.gr.P3m1, Z=24,
	1.587	70	1.587	3.10.6	1.589	324	ρ_x=7.437 gr/cm^3
	1.438	100	1.438	530	1.438	0.0.15,502	
673	2.642	10	2.641	176	-	-	Orthombic, a=7.369Å
	2.464	10	2.463	087	-	-	b=22.417Å
	2.425	30	2.425	258	2.425	$(003)_1$	c=36.179Å
	2.408	80	2.402	094	2.408	009	sp.gr. Pnma
	2.087	20	2.087	319	2.083	119	Z=104, ρ_x=7.058 gr/cm^3
	2.000	20	2.000	3.2.10	2.002	209	Hexagonal-I,
	1.944	10	1.943	366	-	-	a=8.412Å
	1.868	10	1.869	368	1.856	2.0.10	c=21.701Å
	1.848	10	1.847	380,400	-	-	sp.gr. P3m1, Z=24,
	1.819	100	1.815	413	1.819	$(004)_1$	ρ_x=7.319 gr/cm^3
	1.806	50	1.800	414	1.806	0.0.12,402	Hexagonal-II,
	1.597	20	1.597	3.10.6	1.596	324	a=4.237Å
	1.455	30	1.455	504	1.455	$(005)_1$	c=7.275Å
	1.445	90	1.446	530	1.445	0.0.15,502	
773	2.330	20	2.330	267	-	-	Orthorhombic
	2.110	10	2.112	328	-	-	a=7.423Å, b=22.857Å
	2.028	20	2.028	3.0.10	2.028	$(311)^*$	c=35.253Å, sp.gr. Pnma
	1.942	100	1.942	289	1.942	$(222)^*$	Z=104, ρ_x=6.997 gr/cm^3
	1.429	10	1.429	496	-	-	HCC: a=6.727Å, Z=4
							sp.gr. Fm3m, ρ_x=5.329gr/cm^3
873	2.030	10	2.029	311			HCC: a=6.734Å, Z=4
	1.944	100	1.944	222			sp.gr. Fm3m, ρ_x=5.313gr/cm^3
* - reflections from HCC modification							

Table 6.

Thermal expansion of $Cu_{1.75}Cd_{0.05}Te$ (*10^{-6}grad^{-1}) modification.

Modification	T_{exp}, K	$\alpha_{[100]}$	$\alpha_{[010]}$	$\alpha_{[001]}$	$\overline{\alpha} = \frac{\alpha_{[100]}+\alpha_{[010]}+\alpha_{[001]}}{3}$	$\bar{\beta} = \alpha_{[100]} + \alpha_{[010]} + \alpha_{[001]}$
Orthorhombic	290-373	23.603	15.593	-6.975	10.740	32.221
	373-473	5.448	15.266	-3.586	5.709	17.128
	473-573	24.503	25.106	-14.349	11.753	35.260
	573-673	6.790	25.044	-2.487	9.782	29.347
	673-773	-67.851	-74.050	96.188	-15.238	-45.713
	773-833	-84.256	-35.504	71.637	-16.041	-48.123
Hexagonal	290-373	17.273		16.180	16.909	50.726
	373-473	13.123		14.351	13.532	40.597
	473-573	9.532		18.491	12.518	37.555
	573-673	13.094		13.381	13.190	39.569
	673-773	22.587		18.893	21.356	64.067
HCC	833-873	94.838			94.838	284.514
	873-973	9.859			9.859	29.577

The graphically temperature dependences of crystal lattice parameters, atomic volume and densities of $Cu_{1.75}Cd_{0.05}Te$ modifications are given on fig.2. As it is seen from fig.2 *a* and *c* parameters of hexagonal modification in the dependence on temperature linearly increase and *a* и *b* parameters of orthorhombic modification in temperature interval 293-673K also linearly increase and higher this temperature strongly decrease, *c* parameter up to 673K linearly decrease and higher this temperature strongly increases up to transformation into cubic modification.

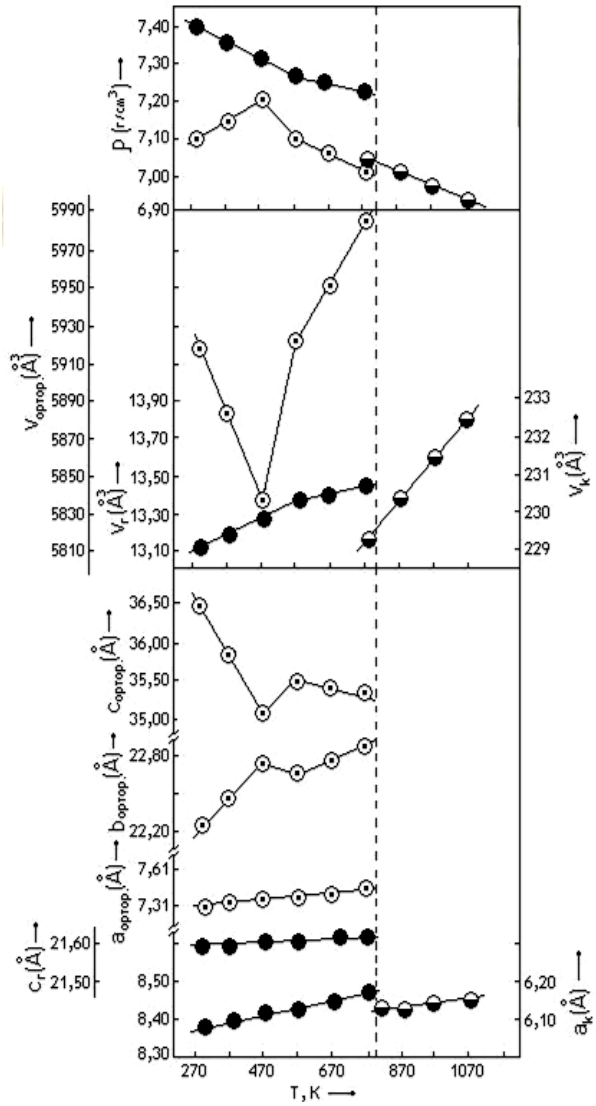

*Fig.1.*Temperature dependence of elementary cell parameters of hexagonal, orthorhombic and HCC of $Cu_{1.50}Zn_{0.30}Te$ modification: ● are a and c, volume *V* and density *ρ* of hexagonal modification; ⊙ are *a*, *b* and *c*, volume *V* and density *ρ* of orthorhombic modification; ◒ are *a* parameter, *V* is volume and *ρ* density of HCC modification

From temperature dependence of lattice parameters of existing modifications TEC are calculated by main crystallographic directions which are given in table 6. The strongly anisotropy on main crystallographic directions of orthorhombic modification is connected with weakening of covalent (short) bonds at increased temperature and their irregular position in crystal lattice.

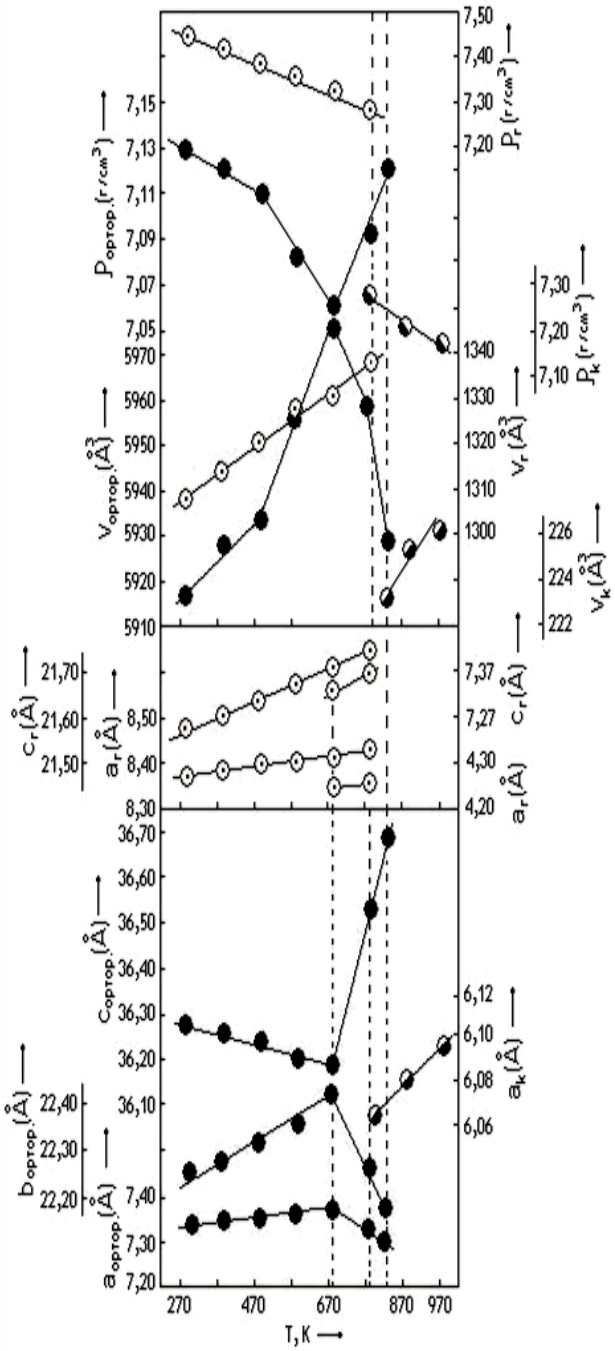

*Fig.2.*Temperature dependence of elementary cell parameters of hexagonal, orthorhombic and HCC $Cu_{1.75}Cd_{0.05}Te$ modifications: ⊙ are *a* and *c* parameters, V volume and density *ρ* of hexagonal modification; ● are *a*, *b* и *c* parameters, *V* volume and density *ρ* of orthorombic one; ◒ are *a* parameter, *V* is volume and *ρ* density of HCC modification

The Novotnov hexagonal modification forming at 673K also essentially influences on parameter values of $Cu_{1.75}Cd_{0.05}Te$ orthorhombic modification. The anomaly in temperature dependence of crystal lattice of orthorhombic modification is observed with formation of this modification.

[1] *F. Guastavino, H. Luquet, J. Bougnot.* Etude du diagramme de phase du systeme Cu-Te dam Le domaine de La Solition solide $Cu_{2-x}Te$, member // Res. Bull., 1973, 8, №8, pp. 935-942.

[2] *R.B. Baranova, A.S. Avilov, Z.Q. Pinsker.* // Kristalloqrafiya, 1973, t.18, v.6, №2, s. 1169-1176. (in Russian).

[3] *R.B. Baranova, Z.Q. Pinsker.* // Kristalloqrafiya, 1964, t.9, №1, s. 104-106. (in Russian).

[4] *R.B. Baranova.* // Kristalloqrafiya, 1967, t.12, №2, s. 266-273. (in Russian).

[5] *R.B. Baranova,* // Kristalloqrafiya, 1968, t.13, №5, s. 803-808. (in Russian).

[6] *Novotny H.* Die Kristallstructurs von Cu_2Te // Z. Metallkunde, 1946, 37, pp. 40-42.

[7] *A.S. Pashinkin, Q.N. Tishenko, I.V. Korneva I dr.* // Kristalloqrafiya, 1960, t.5, №2, s.261-267. (in Russian).

[8] *Thomassen, L., Mason, D.R., Rose, G.D., et al.* The Phase Diagram for the Pseudo-Binary System CdTe–In_2Te_3 // J. Electrochem. Soc., 1963, vol. 110, № 11, pp. 1127–1131.

[9] *W.H.Zachariasen.* Z.Phys. Chem., Die kristallstruktur von berylliumoxyd und berylliumsulfid//Z.Phys.Chem. *1926, v.*119, pp. 201-213.

[10] *M.R.Lorens,* Phys. Chem. Solids, 1962, 23, pp.939-947.

[11] *K.B. Shalimov, A.F. Andrushko, I. Spinulesku-Karnaru I dr.* Kristalloqrafiya, 1964. t. 9. №5. s. 741-743.

Received: 26.01.2012

THE THERMAL CONDUCTIVITY OF $(PbS)_{1-x}(Sm_2S_3)_x$ (x=0÷0.04) SOLID SOLUTIONS

G.A. GASANOV, E.G. JAFAROV, U.S. NAMAZOV
of Azerbaijan Republic Academy o Ministry of NationalSecurity named by Heydar Aliyeva
AZ-1029,A.Gayibov str.,6, Baku, Azerbaijan Republic,
hummat.hasanov@gmail.com

The temperature dependences (in 170÷670K interval) of λ thermal conductivity of $(PbS)_{1-x}(Sm_2S_3)_x$ (0-4 mol.% Sm_2S_3) solid solutions are obtained. The isotherms of λ_l lattice thermal conductivity λ_l are constructed on the base of these data and the effective cross section of phonon scattering on *Sm* impurity atoms is estimated. The region of λ_l anomalous growth is revealed in the region of 1.25-2.0 mol.% Sm_2S_3 concentrations not corresponding with usually observed decrease of λ_l at increase impurity concentration. It is supposed that anomalous growth of λ_l begins to take place when in the crystal the continuous chain of overlapping deformative fields formed by separate atoms forms; the partial compensation of strengths in crystal lattice takes place and phonon dispersion decreases. The universal character of revealed effect is supposed.

Keywords: thermal conductivity, isotherm, solid solution
PACS: 61.72

INTRODUCTION

The compounds of $A^{IV}B^{VI}$ type and solid solutions on their base belong to the number of well known semiconductor materials which are wide used in IR-techniques, thermoelectricity, tensometry and etc [1,2]. In these solid solutions the concentration anomalies of properties [3,4] the presence of which is connected with critic phenomena having the percolation nature and belonging to any solid solution [5], are observed in the series of the given solid solutions in the impurity small concentration region by us.

The solid solutions on *PbS* base in $(PbS)_{1-x}(Sm_2S_3)_x$ ($x = 0 \div 0.04$) base crystallizing in the structure by *NaCl* type are the object of the present investigation [6]. The anomalies on the concentration dependences of Hall coefficients, electric conduction and thermal expansion coefficient near ~1 mol.% Sm_2S_3 are observed in these solid solutions [6].

The investigation of temperature dependences of λ thermal conductivity and construction of isotherms on their base are the aims of the present work.

THE EXPERIMENT TECHNIQUE

The $(PbS)_{1-x}(Sm_2S_3)_x$ (0-4 mol.% Sm_2S_3) alloys are prepared by ampoule method from elements of high purity and are endured by homogenization annealing at 900K during 200h. The two series of alloys with the similar composition set are prepared at the synthesis for exclusion of accidental errors. λ measurement is carried out by the method of dynamic calorimeter in the mode of monotone heat [3] in 170÷670K temperature interval on cylinder samples by 1,5 cm diameter and 0,5 cm height. The samples are prepared by hot pressure method at temperature 770K and pressure 4000 kg/cm^2, annealed during 200h at 900K and cooled in the air. After the given treatment the region of solid solutions on *PbS* base is ~ 3 mol.% about which the results of microstructure investigation, parameter precision measurement and microhardness one prove. The temperature dependences λ for all samples are obtained. λ measurement is carried out on each sample not less than 3 times and the results are averaged. The curve shift λ(T)from measurement to another one on the same sample usually doesn't exceed ~5% and is explained by some nonidentity at sample positioning in the device which takes place. The absence of λ(T) curve systematic shift fact at repeat processes of heat-cooling during the measurements evidences about unimportance of the thermocycling influence on λ value and on enough sample degree of homogeneity achieved at thermal treatment. The resultant dependence λ(T) for each from the compositions is constructed by the way of data averaging obtained for first and second alloy series. The electric conduction σ is measured by four-probe method with the delicacy not less than ~5%. The assignment of electronic thermal conductivity component λ_e is carried out by Videman Frantz law; $\lambda_e = L\sigma T$. The Lorentz number *L* is defined by the formula which is right for degenerated semiconductors, $L=(r+2)(k_0/e)^2$ (r is degree coefficient in the dependence on free length on energy λ=ε`) [7] in supposition of carrier dominated scattering on acoustic lattice oscillations (r=0.1).

THE RESULTS AND DISCUSSION

The dependences λ(T) for samples of the different compositions are given on fig.1. The clearly expressed minimum at ~ 400÷450K on all curves takes place.

It is known that heat transfer in semiconductors in general case can be carried out by crystal lattice oscillations, electronic gas, electromagnetic radiation and also by bipolar diffusion of charge carriers [4.5]. That's why the expression for calculation of total thermal conductivity λ can be written in the form:

$$\lambda = \lambda_l + \lambda_e + \lambda_{ph} + \lambda_b, \qquad (1)$$

where $\lambda_l, \lambda_e, \lambda_{ph}, \lambda_b$ are lattice, photon and bipolar components of λ correspondingly. The growth λ after $400 \div 450$K can be caused by increase of electron transfer, however, the estimation of electron component shows that λ_e makes the unimportant contribution into total thermal conductivity (not more than 7%) and can't provide the extremal character of λ(T) dependences. That's why one can suppose that the bipolar diffusion of charge carriers caused by appearance of intrinsic conductivity takes place as *PbS* [8]. The fact that intrinsic conductivity is observed at enough low temperatures is connected with complex structure of valency band of $p-PbS$ the parameters of which essentially depend on temperature.

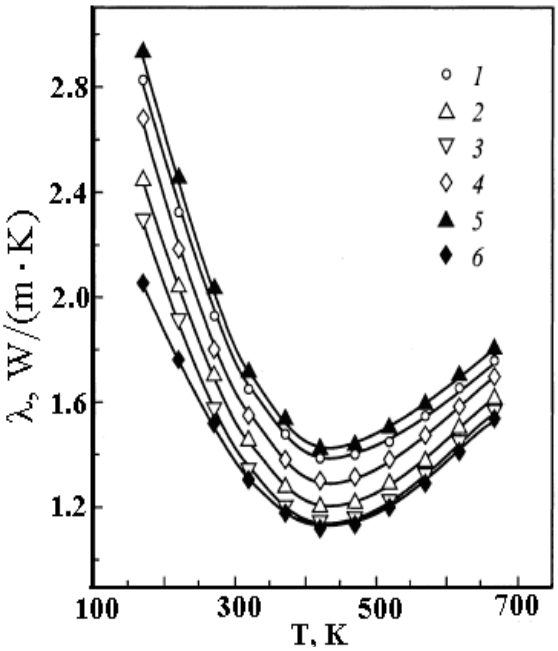

Fig.1. The temperature dependences of thermal conductivity in solid solutions $(PbS)_{1-x}(Sm_2S_3)_x$. Sm_2S_3 (in mol.%) concentration: *1*- 0, *2*- 0.75, *3*-1.25, *4*- 1.75, *5*-2.0, *6*-4.0.

According to many works [4,5] the valency band of lead chalcogenides consists of two overlapping subbands with different state density divided by energy gap ΔE, decreases with temperature growth and becomes equal to zero at $450 \div 500$K. The further temperature growth leads to the fact that subbands of "easy" and "heavy" holes change places. The impurity Sm_2S_3 introduction leads to increase of forbidden band width, but the valency band structure PbS and $(PbS)_{1-x}(Sm_2S_3)_x$ solid solutions stay identical ones [7].

The heat transfer by electromagnetic radiation is significant in that case when the absorptivity in the region of heat radiation is mall one [8,10]. As the absorption coefficient of *PbS* is big enough ($\alpha \approx 200\text{cm}^{-1}$) and in $(PbS)_{1-x}(Sm_2S_3)_x$ alloys α value exceed by a factor of ten [8], the heat transfer by electromagnetic radiation can be ignored. The estimation of photon thermal conductivity shows that in whole temperature interval contribution of λ_{ph} in total conductivity doesn't exceed 0,5%.

Taking under consideration the insignificant contribution λ_e and λ_{ph} in total alloy thermal conductivity $(PbS)_{1-x}(Sm_2S_3)_x$ can be expressed by the sum of lattice and bipolar components $\lambda = \lambda_l + \lambda_b$. The temperature dependences of thermal resistance calculated by taking under consideration lattice and bipolar components: $W_{exp}=1/(\lambda_l+\lambda_b)$. In temperature interval $170 \div 400$K the linear growth W_{exp} is observed and at temperatures higher ~400K the thermal resistance decreases.

It is known [4] that at $T \geq \Theta$ (Θ is Debye temperature) the phonon mean free path is limited by interphonon interaction of phonons with lattice defects. At taking under consideration only three-phonon processes and scattering on defects in the correspondence with Debye-Payerls theory the lattice thermal resistance can be expressed in the following form:

$$W_л = 1/\lambda_l = AT + B, \qquad (2)$$

where A is coefficient taking under consideration the oscillation anharmonicity degree of crystal lattice and *B* defines the additional thermal resistance caused by the lattice defects. Extrapolating the linear part of $W_{exp}(T)$ to high temperatures (dotted line on Fig.2), one can define the contribution of bipolar component of thermal conductivity by distance between dotted line and experimental curve:

$$\lambda_b = 1/W_{exp} - 1/W_л.$$

The estimations made with correspondence with them show that the contribution of bipolar component is big one and at temperature ~670K achieves ~60% of total thermal conductivity.

The concentration dependences λ_l (before beginning of carrier bipolar diffusion) and $(\lambda_l+\lambda_b)$ (after beginning of carrier bipolar diffusion) are constructed on the base of α and σ temperature dependences (Fig.3). From this picture it is seen that dependences have the clearly expressed nonmonotonic character: on all curves in concentration interval 1.25-2.0 mol.% Sm_2S_3 the region of anomalous growth of lattice conductivity takes place.

Usually λ_l decreases because of phonon scattering on impurity atoms with growth of impurity concentration in solid solution region. In limits Klemens theory λ_l decrease in region of slid solutions is defined by the mass difference and lattice main and impurity atoms, difference

of bond forces in neighborhood impurity atom and also by elastic stress caused by difference of atom sizes [6]. In the investigated system λ_l decrease is observed in the regions of 0-1.25 and 2.0-4mol.% Sm_2S_3 compositions.

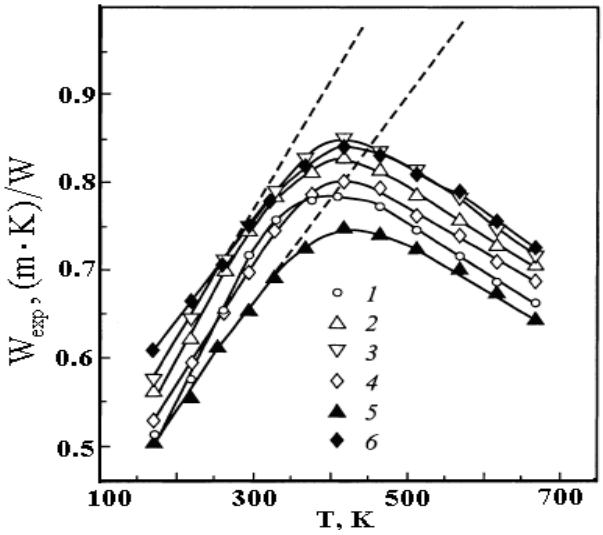

Fig.2. The temperature dependences of thermal resistance in $(PbS)_{1-x}(Sm_2S_3)_x$ solid solutions. The concentration Sm_2S_3 (in mol.%): *1*- 0, *2*- 0.75, *3*-1.25, *4*- 1.75, *5*- 2.0, *6*-4.0.

The anomalous growth λ_l in intermediate concentration interval we connect with critical phenomena of percolation type taking place in crystal impurity subsystem [3].

The impurity atoms are centers of local lattice distortions, sources of internal stress and deformations decreasing inversely to distance in third degree [7]. As the atom marked shifts form on length equal to one-two atom distances, the elastic deformation field can be considered as short-range one and can use the conception of character radius of deformation interaction R_0. At small impurity concentration when the distance between them is much bigger than R_0 the deformation fields formed by separate atoms aren't practically overlapping and make the additive contribution in lattice thermal resistance increasing it.

As impurity concentration increases, the overlapping of elastic fields of neighbor atoms leading to partial compensation of elastic stress of opposite sign takes place. In short-range approximation supposing the distribution statistic character of impurity atoms by means of the percolation theory [8] using R_0 values one can estimate the concentration x_c (percolation threshold) at which the collective interaction corresponding to formation of unit chain of overlapping deformation fields going through whole crystal (so-called "infinitive cluster"), begins. We can solve the inverse task: by the value of critic concentration x_c we can define R_0 radius. Considering that x_c corresponds to ~ 1.25mol.% Sm_2S_3 we obtain $R_0 \approx (1/2)\cdot\alpha_0$ (α_0 is elementary cell parameter) that corresponds with short-range character of deformation interaction. The transition from dissolved solid solutions to concentration ones when the continuous cluster forms should be accompanied by critic phenomena, analogical phase transitions of second order [2]. As the partial compensation of opposite sign stress leading to decrease of general level of elastic lattice stress corresponds to percolation channel formation, one can suppose that this leads to increase of lattice thermal conductivity.

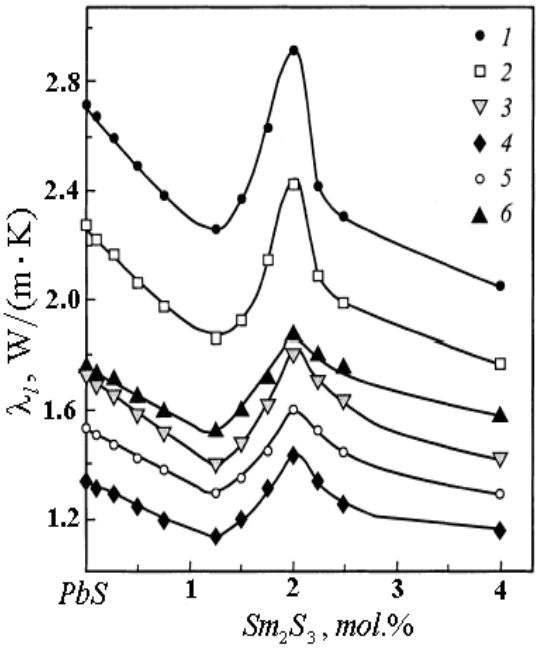

Fig.3. The isotherms of lattice thermal conductivity in $(PbS)_{1-x}(Sm_2S_3)_x$. T,K: 1- 170, 2- 220, 3- 295, 4- 420, 5- 570, 6- 670 solid solutions.

The growth λ_l in anomalous region is connected with increase of infinitive cluster density. After that as compensation process of elastic stress catches the whole crystal and whole volume is filled by "impurity liquid", the further impurity atom introduction leads to new lattice distortions and therefore to decrease of lattice thermal conductivity. The situation can be analogical to Mott transition when percolation channel formation on electron membranes of separate atoms leads to appearance of electric conductivity (metal-dielectric transition). In considered case the percolation channels form by deformation fields of separate impurity atoms. At critic concentrations the probability of impurity atom ordering processes strongly increases. The simple calculation shows that composition ~1.0mol.% Sm_2S_3 is the optimal one for ordered distribution of impurity atoms over nodes of primitive cubic lattice with period $\alpha = 3\alpha_0$, but at ~1.6mol.% Sm_2S_3 the formation of superstructure with HCC –lattice of impurity atoms is possible and with period $\alpha = 4\alpha_0$ (α_0 is alloy elementary cell parameter). The significant growth λ_l in λ_l interval can directly show on the presence of order processes.

The nonsignificant contribution of electronic component of thermal conductivity in the investigated alloys doesn't allow us to connect the observable concentration anomalies λ_l with change of Lorentz number which can takes place at strong doping as a result of electron-electron interaction [9].

By concentration dependence λ in 0-1.25mol.% Sm_2S_3 region the estimation of effective phonon cross sections on Sm impurity atoms with the use of Yoffe formula [4] is made:

$$\frac{\lambda}{\lambda_0} = 1 + \Phi \frac{N}{N_0} \cdot \frac{l_0}{d}, \qquad (3)$$

where λ_0 and λ are crystal thermal conductivity coefficients without impurities, N and N_0 are number of impurity and all atoms in volume unit correspondingly. d is distance between atoms, l_0 is average phonon free path introducing into expression for thermal conductivity coefficient of non-doped crystal; $\lambda_0 = l_0 C_V \nu_g / 3$ (where C_V is volumetric heat capacity and ν_g is average group velocity, Φ is coefficient introducing into expression for effective cross section of $S = \Phi \cdot d^2$ phonon scattering. Substituting the values $\lambda_0, \lambda, N, N_0$ and also C_V and ν_g in (3) we obtain that $\Phi = 1.9$ and $S = 1.9d^2 = 0.48a_0^2$ at 300K. The obtained S shows that the impurity atoms aren't the centers of phonon effective scattering in solid solutions under consideration.

[1] *A.B. Lyubchenko, E.A. Salkov, F.F. Sizov.* Fizicheskoe princhipi poluprovodnikov infrakrasniy fotoelektroniki . Nauk. Dumka, Kiev (1984). 254 s. (in Russian).

[2] *N.X. Abrikosov, L.E. Shelimova.* Poluprovodnikov materiali na osnove soedineniy $A^{IV}B^{VI}$. Nauka, M.(1975). 195 s. (in Russian).

[3] *M.I. Murquzov, Q.A. Qasanov.* Temperaturnie i konchentrachionnie zavisimosti podvijnosti nositeley zaryada v tverdix rastvorax $(PbS)_{1-x}(Sm_2S_3)_x (x = 0 \div 0.04)$ // Texnoloqiya i konstruirovanie v elektronniy apparature. Odessa, 2008, № 6. s.50-54. (in Russian).

[4] *Yu.I. Ravich, B.A .Efimova, I.A. Smirnov.* Metodi issledovaniya poluprovodnikov v primenenii k xalqonidam svinicha $PbS, PbSe, PbTe$, Nauka, M.(1968).384 s. (in Russian).

[5] *Q.A. Qasanov.* Elektricheskie i fotoelektricheskie svoystva plenok silno kompensirovannix tverdix rastvorov na primere $(PbS)_{1-x}(Sm_2S_3)_x\langle Na\rangle$ // Moskva-Taqanroq, Voprosi spechialnoy radioelektroniki. 2008, №2, c.113-121. (in Russian).

[6] *Q.A. Qasanov.* Vliyanie rasseyaniya fononov na neytralnix i zaryajennix primesnix chentax na teploprovodnost reshetki v $Pb_{0.98}Sm_{0.02}Te\langle Na\rangle$.// Baku, Vestnik Bakinskoqo Universtiteta, 2009, №1, s. 166-172. (in Russian).

[7] *M.I.Murquzov, H.A.Hasanov.* Hall mobility of charge carriers in films of $(PbX)_{1-x}(Sm_2X_3)_x$ semiconductors formed on porous silicon // Semiconductor Physics, Quantum Elecrtonics &Optoelectronics, 2008, V.11,4, p.356-359.

[8] *Q.A. Qasanov.* Vliyanie primesi natriya na xarakter lokalizachii dirok v tverdix rastvorax sistemi Ln-Pb-Se (Ln –Nd,Sm) // Materiali Mejdunorodnoy nauchnoy konferenchii «Praktika i persperspektivi razvitiya partnerstva v sfere visshey shkoli» Donechk, 2009, may , s.59-65. (in Russian).

[9] *H.A.Hasanov.* Electrophysical Properties of $Sm_xPb_{1-x}Te$ Solid Solutions// Semiconductor Physics, Quantum Electronics&Optoelectronics, 2009, V.12,1, p.135-137.

Received: 20.12.2011

LUMINESCENT PROPERTIES OF $YbGa_2S_4:Er^{3+}$ SINGLE CRYSTALS

B.G. TAGIYEV[1,2], O.B. TAGIYEV[1,3], F.A. KAZIMOVA[1], U.F. KASUMOV[1]

[1]Institute of Physics of ANAS
AZ 1143, H.Javid ave., 33,
[2]National Space Academy, Bina, Baku, Az1045, 25 kilometer
[3]Branch of Moscow State University named by M.V.Lomonosov in Baku
E-mail:oktay@physics.ab.az

The photoluminescent properties of $YbGa_2S_4:Er^{3+}$ crystal at excitation by emission with λ=337,1nm and λ=976nm in the dependence on temperature. The samples are obtained with the help of solid-state reaction. The mechanisms of Stokes and anti-Stokes luminescence of $YbGa_2S_4:Er^{3+}$ crystals are defined.

Keywords: photoluminescence, rare-earth element, kinetics, anti-Stokes luminescence.
PACS: 76.30, 78.55

INTRODUCTION

The process-dependent parameters of the growth of triple earth chalcogenide semiconductors by $Sr(Eu,Yb,Sm,Ca,Ba)Ga(Al)_2S(Se,O)_4$ type and also of doping by rare-earth elements define their emissive properties. One can change the transformation efficiency of different energy types into light one and luminescence color of these compounds by the selection of corresponding sensitizers and activators. The oriented optimization, i.e. the improvement of obtaining technology of new luminescent materials perspective for the formation of luminophors with the special properties allowing their usage for emission visualization beyond visible range of spectrum and lighting, is possible on the vase of establishment of feedback between growth and doping parameters of these materials with their structural, optical, luminescent and laser properties [1,2,3,4].

The mode is developed and 10 representatives of triple chalcogenides of $A^{II}B^{III}{}_2C_4^{VI}$ type including $YbGa_2S_4$ are obtained in [5]. The oriented crystallization and annealing with slow temperature decrease (5degree/h) are applied for single crystal obtaining. The crystal structure parameters have the values *a*=20,112; *b*=20,082 and *c*=12,132Å. The obtained compounds are treated by micro-structural, X-ray-phase, thermographic analyses and microhardness measurement. The detail thermographic investigation and chemical analysis of the compounds show that they are individual phases having the character melting points regularly decreasing from gallium-containing compounds up to indium-containing ones, and also from europium-containing up to ytterbium-containing ones. The investigation results of photoluminescence spectrum of $YbGa_2S_4$:Er crystal at different temperatures and luminescence kinetics are given in present paper.

THE SAMPLE OBTAINING AND THE EXPERIMENT

$YbGa_2S_4$ samples are obtained from double YbS and Ga_2S_3 compounds by the way of solid-state reaction in graphite crucible covered by activated carbon. Er doping is carried out by ErF_3 use in synthesis process. The powder after drying is treated by H_2S stream at 900°C during 4 hours. X-ray analysis of the powder shows that all samples well crystallize, in particular, after treatment. It is proved that treatment improves the crystallization and solubility of Er^{3+} ions.

The impulse diode laser is used for excitation at 976nm. The light radiated by the sample, is collected by optical fiber situated perpendicular to sample surface on distance 10mm and is analyzed by HR460 Yobin-Ybon spectrometer and multi-channel detectors Spectramax and TRIAX 320 Hamamutsu PDA into visible and IR regions correspondingly.

THE RESULTS AND DISCUSSION

The photoluminescence spectrum of $YbGa_2S_4$:Er crystal at $\lambda_{ex}=337,1nm$ in temperature interval 78-300K is shown on fig.1. The spectrum consists of three parts of emissive transitions. The first region is wave length interval 550-650nm (is connected with *f-d* transition of Yb^{2+}ion [6,7]), second region is in interval 800-870nm and the third one is in interval 870-950nm. These narrow-band emissions are connected with transitions $^4I_{9/2} \rightarrow {}^4I_{15/2}$ and $^4I_{11/2} \rightarrow {}^4I_{15/2}$ of Er^{3+} ions [8]. We observe also emission of Er^{3+} ion with $I_{13/2} \rightarrow {}^4I_{15/2}$ transition in IR spectrum region (1480-1600nm) (fig.2) [8].

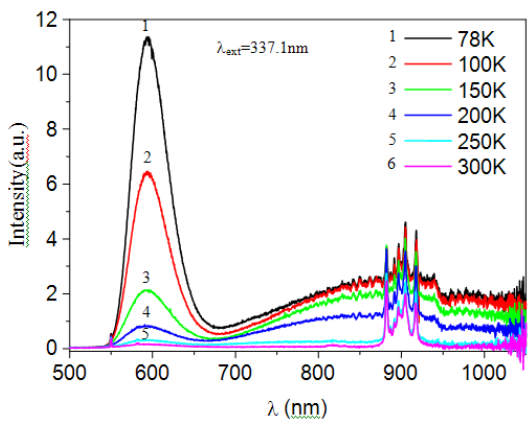

Fig.1. The luminescence spectrum of $YbGa_2S_4:Er^{3+}$ crystal at temperature different values.

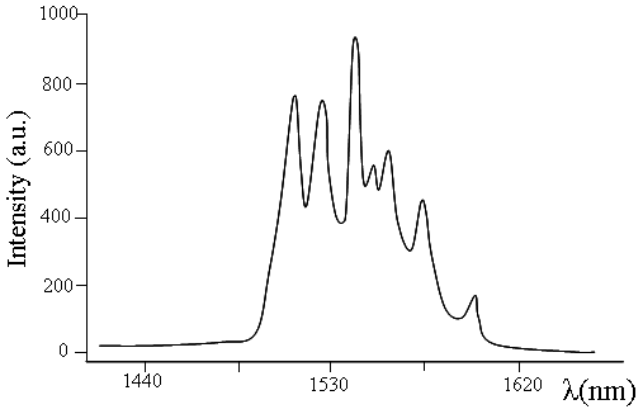

Fig.2. The luminescence spectrum of $YbGa_2S_4:Er^{3+}$ crystal in IR region at λ_{exc}=337.1nm and T=300K.

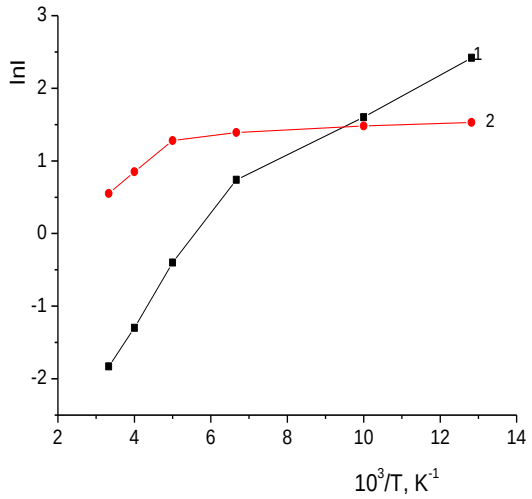

Fig. 3. The temperature dependences of PhL intensity for maxima 595nm-1 and 900nm-2.

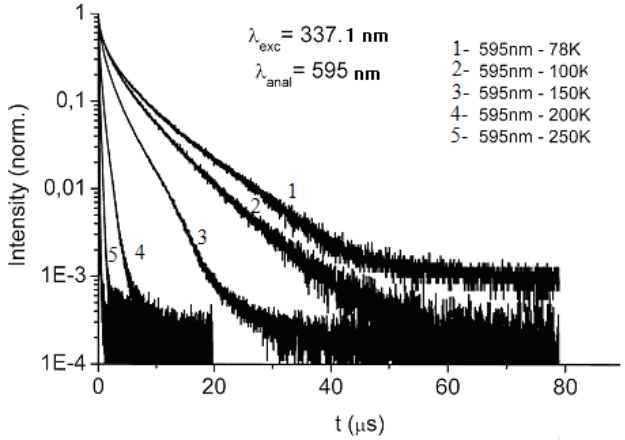

Fig. 4. Time dependences of Er^{3+} ion emission lines at 595nm of $YbGa_2S_4:Er^{3+}$ crystal at different temperatures.

The activation energies of luminescence centers 009 and 0,07eV responsible for emission 595 and 900nm correspondingly are defined from temperature dependence of intensity (fig.3). The kinetics of emission maximum at 595nm at different temperatures is presented on fig.4. At 78K the emission kinetics in interval 0-20μs has hyperbolic character with the following transition on exponential regularity. This can be connected with two different states for Yb^{2+} ion [9,10]. The life time decreases with temperature growth (fig.5).

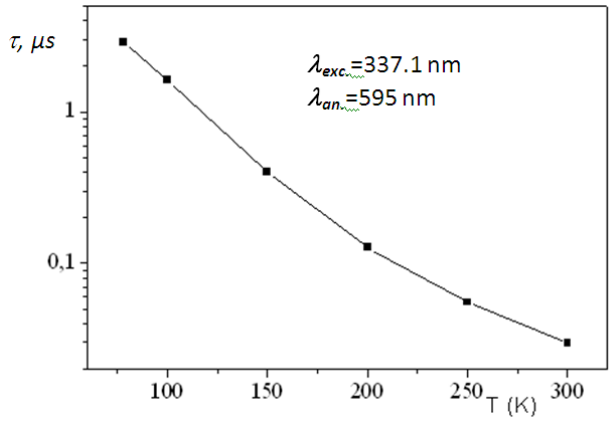

Fig. 5. The dependence of life time on temperature.

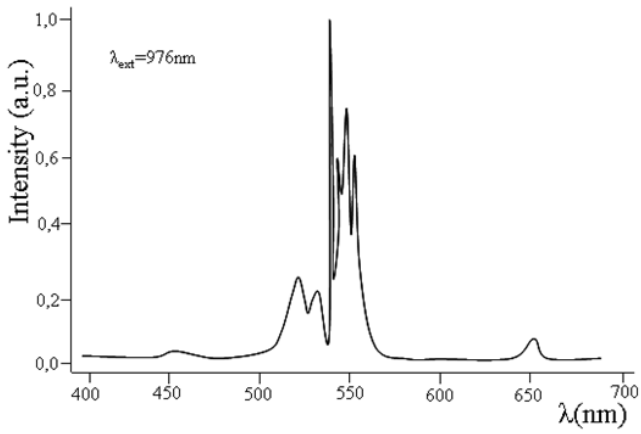

Fig.6. The spectrum of anti-Stokes emission of $YbGa_2S_4:Er^{3+}$ (λ_{ex}=976nm and T=300K).

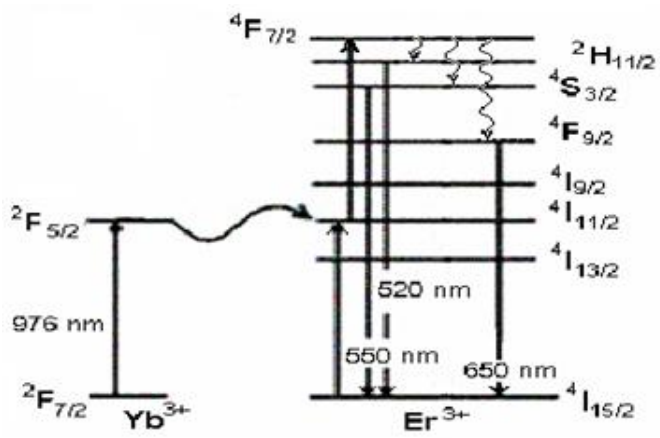

Fig.7. The energy scheme of anti-Stokes luminescence in $YbGa_2S_4:Er^{3+}$ (λ_{ex}=976nm and T=300K).

The study of Er^{3+} ion at $\lambda_{max}=1560nm$ gives the possibility of $YbGa_2S_4$ crystal usage in the capacity of active mediums for lasers emitting in the region 1530nm. The principle of operation of optical divisors using REE in the capacity of active material bases on the following fact. During preparation the base material is doped by rare-earth elements. Their ions form the active medium of wave length of special bands corresponding to absorption bands of doping material. The impurity ions can be excited by emission of laser pumping of corresponding wave length and further, they can relatively easily drop the excited electrons on low level in relaxation process. This process can't correspond to two-level model of interaction taken under consideration as the main one, such process goes with phonon emission and without it. In first case the phonons are formed (transition energy causes the environment oscillations). In second case the phonon excitation takes place.

Moreover, the transition from excited level to relaxation one carries out through intermediate metastable level caused by upper laser level. Thus, interaction model becomes the three-level one. In any case, for the normal interaction the photon energy in signal flow should be equal to difference of excited level energy and relaxation one.

Last time the materials where there are towards ytterbium (Yb) and erbium (Er) ions are applied for emission amplification at 1550nm. Er ions have absorption peaks in region of wave length 532, 660, 808, 980, 1480nm. From this it is followed that known laser types with wave lengths 800, 980 and 1480nm can serve as pumping source. The three-level interaction models of interaction correspond to 800 and 980nm and two-level model correspond to 1480nm.

These lasers are used widely enough, taking under consideration (because of three-level interaction) very low noise level (3-5dB order). However, lasers on 1480nm though they are effective ones (70% from laser on 980nm), are considered the more preferable ones and can realize the low enough noise level (5dB order). One can use the laser pumping diodes working on wave length 1053nm at Yb ion use in the capacity of component. Their use allows us the obtaining the more pumping source.

The anti-Stokes emission (fig.6) is revealed at excitation of $YbGa_2S_4$:Er[11] compound by emission of wave length 976nm. We suppose the following mechanism of anti-Stokes emission (fig.7). The photon absorption with wave length 976nm leads to $^2F_{7/2}\rightarrow{}^2F_{5/2}$ electron transition in Yb^{3+} ion. The migration of excitation energy on crystal one can lead to the excitation energy transfer from $^2F_{5/2}$ level of Yb^{3+} ion on near energy level $4I11_{/2}$ of excited state of Er^{3+} ion. The absorption of second photon leads to $^4I_{11/2}\rightarrow{}^2F_{7/2}$ transition in Er^{3+} ion and moreover, the energy transition from Yb^{3+} also takes place. The corresponding emitting transitions into main state ($^2H_{11/2}\rightarrow{}^4I_{15/2}$, $^4S_{3/2}\rightarrow{}^4I_{15/2}$, $^4F_{9/2}\rightarrow{}^4I_{15/2}$) take place after thermal relaxtion from $^2F_{7/2}$ level to $^2H_{11/2}$, $^4S_{3/2}$ and $^4F_{9/2}$, levels and the emission at 520, 540 and 650nm is observed. The nature of this process is caused by realization of two acts of elementary excitations of the same Er^{3+} ion.

CONCLUSION

The luminescent materials doped by Er^{3+} and having the emission at 1550nm present the big interest for thin-film integral technology, standard telecommunication zona C (1530-1560nm). It is established that the consecutive excitation energy transfer from sensibilizator to emitting activator, i.e. the consecutive sensibilization is the mechanism of observable anti-Stokes emission.

The given paper is carried out at financial support of Science Development Fund under President of Azerbaijan Republic, Grant № EİF-2011-1(3)-82/01/1.

[1] *A.A. Koplyanskiy, A.K. Projevuskiy*. Opt. i spektr. 1965, 19, s.597-610.

[2] *V.E. Oranovskiy, Z.A. Trapeznikova*. Opt. i spektr, 1958, 5, s.302-306.(in Russian)

[3] *Z.A. Trapeznikova, V.V. Shaenko*. Nekotorie opticheskie svoistva novih sinkosulfidnih fosforidov, aknivirovannih RZE. DAN SSSR. 1956, 106, s.230-232.(in Russian)

[4] *P.P. Feofilov*. Spektroskopiya kristallov. M. «Nauka», 1966, 87s. (in Russian)

[5] *O.M. Aliyev, M.A. Alijanov, T.Kh. Kurbanov, P.G. Rustamov, S.M. Salmonov.* Neoganicheskie materiali. 1976, t.12, №2, s. 1944-1947.(in Russian)

[6] *G.K. Aslanov, Ch.M. BriskV.F. Zolin, V.M. Markushev, G.M. Niftiyev, O.B. Tagiyev*. Neoganicheskie materiali. 1986, t.22, 10, s.1630-1634.(in Russian)

[7] *A.N. Georgobiani, A.N. Gruzintsev, P. Benallol et.al.* Infrared Luminescence of Er^{3+} in Calcium thiogallate. J. of the Electrochemical Society. 2001, 148(11), H167-H170.

[8] *C. Barthou, P. Benalloul, B.G. Tagiev, O.B. Tagiev, et.al.* Energy transfers between Eu^{2+} and Er^{3+} in $EuGa_2S_4$: Er. // J. of Physics: Condensed matter. 2004, 16, p.8075-8084.

[9] *S. Lizzo, E.P. Klin, N. Nagelvoort et al.* On the quenching of the Yb^{2+} Luminescence in different host lattices. // J. of physics and chemistry of solids 1997, 58, 6, p.963-968.

[10] *S. Lizzo, A. Meijerink, G. Blasse.* Luminescence of divalent ytterbium in alkaline earth sulphates. // J. of Luminescence. 1994, 59, 3, p.185-194.

[11] *A.N. Georgobiani, B.G. Tagiyev, O.B. Tagiyev, R.B. Jabbarov, S.A. Abushov, F.A. Kazimova, K. Bartou, P. Benaloul, V.M. Salmanov.* JPS, 2007, t.74, 3, s. 332-335. (in Russian)

Received: 26.12.2012

ISSN 1028-8546

2012, Vol. XVIII, 1
Section: En

CONTENTS

www.physics.gov.az